A Raman Quantum Free-Electron Laser Model

Schouwenaars, S.

Award date:
2022

Department of Applied Physics
Coherence and Quantum Technology (CQT)

A Raman Quantum Free-Electron Laser Model

Master Thesis (60 EC)

S. Schouwenaars
1000983

Public thesis created following the TU/e Code of Scientific Integrity

Committee:
Prof. dr. ir. O.J. Luiten (Chair)
Dr. ir. S.J.J.M.F. Kokkelmans
Prof. dr. A.A. Darhuber
MSc. B.H. Schaap (Advisor)

Supervisors:
MSc. B.H. Schaap
Prof. dr. ir. O.J. Luiten

Eindhoven, July 2022

Abstract

Operation of a Quantum Free-Electron Laser (QFEL) could provide fully coherent X- and γ-rays from a compact setup. Imperative to experimental realization is allowing for decoherence of both spontaneous emission and space-charge to take place, having opposing constraints. Current models assume a Compton regime where the QFEL process is negligibly influenced by the space-charge forces resulting from the mean electric field of the charged particle distribution. Here, for the first time, we present a QFEL Wigner model that includes microscopic space-charge by quantizing the periodic potential derived from Fourier components of the longitudinal electron beam density. The model is then used to investigate QFEL dynamics in a Raman regime where space-charge effects become important. Next, we include spontaneous emission and 3D radiation diffraction to the model, which is used to investigate the design parameters for a future QFEL setup. We find that the ultracold electron source (UCES) together with commercially available laser systems can potentially drive a realizable QFEL in a moderate space-charge regime.

Contents

1 Introduction

It is hard to overstate that lasers have become essential to modern life because of their vast applications in industry, science and technology. Ever since the development of the first laser in the 1960s [1], decades of scientific progress have resulted in various types of coherent light sources that cover a broad range of the electromagnetic spectrum. By pushing towards shorter wavelengths and pulse lengths, radiation can be used to probe matter at higher spatial resolutions and has enabled advanced imaging applications in material and life sciences [2]. Coherent radiation in the soft and hard X-ray regime is therefore highly desired, but significantly more challenging to produce using conventional laser technology [3]. For this reason, high-quality X-rays are currently provided, for the most part, by accelerator-based light sources such as the Free-Electron Laser (FEL). X-ray FELs in operation today are primarily based on the Self-Amplified Spontaneous Emission (SASE) mode. SASE lasing originates from shot noise, resulting in a low temporal coherence and poor pulse-to-pulse stability of the generated X-ray pulses compared to more conventional laser sources. Several schemes have been proposed and demonstrated to improve the longitudinal coherence of FEL radiation, such as coherent seeding and prebunching techniques using high-gain high harmonic generation (HGHG) or echo-enabled harmonic generation (EEHG) [4]. Unfortunately, these methods start to present difficulties when going to very short wavelengths [5]. In 2005, Bonifacio *et. al.* showed that by entering the quantum regime of FEL operation, one could produce short-wavelength radiation with a strongly narrowed spectrum and increased coherence compared to classical FELs, due to a process known as "quantum purification" [6]. This extremely promising feature has put the Quantum Free-Electron Laser (QFEL) at the center of continued theoretical interest, as it could provide a fully coherent compact X-ray device with exceptional radiation properties. To find a realizable parameter space, however, there is a need for a more comprehensive quantum theory of QFELs that includes the Raman regime in which space-charge effects become important [7]. This thesis will provide a theoretical continuation of QFEL theory, particularly by describing this Raman regime. In this introductory chapter, we will first introduce a basic laser model and both the classical and quantum versions of the FEL.

1.1 A basic laser model

The laser, short for Light Amplification by Stimulated Emission of Radiation, is a device that produces coherent radiation through optical amplification. In general, these devices consist of a gain medium, a mechanism to energize (or pump) that medium, and something to provide optical feedback with [8], which is seen in Fig. 1.1. To facilitate the stimulated emission events to be amplified, gain media contain an internal structure of (excitable) quantum states that can interact with and produce photons. In practice, the gain medium is not limited to a single state of matter: from gases in gas lasers and liquids in dye lasers all the way up to photonic crystals and semiconductors used by solid-state lasers. The wavelength at which a laser is able to produce radiation is directly dependent on the material properties that determine the energy separation between specific quantum states. This energy separation ΔE is related to the radiated photon energy and frequency by

$$\Delta E = E_e - E_g = \hbar\omega_R = \frac{hc}{\lambda_R}. \tag{1.1}$$

A lasing process is ordinarily characterized by three steps. First, the gain medium is pumped by preparing many atoms in the same excited state, or energy level. Then, spontaneous emission events take place where atoms spontaneously drop to the ground state and produce photons. Thirdly, when such a system is contained within a resonator or optical cavity, the spontaneously emitted photons oscillate through the gain medium and initiate stimulated emission events that produce more photons, which acts as an amplification process.

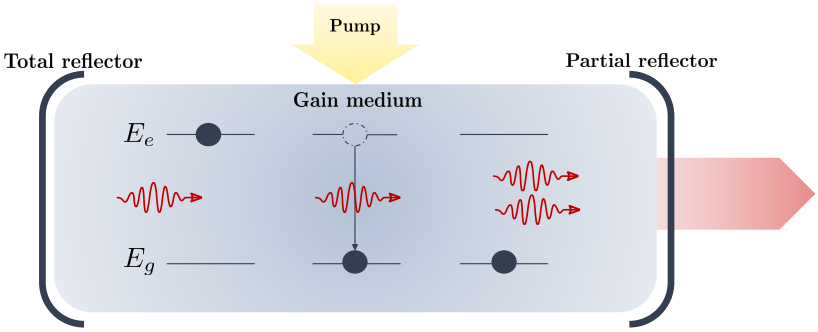

Figure 1.1: Schematic of a laser with two-level quantum system and stimulated emission: a single photon causes the decay of electron from the excited state E_e to the ground state E_g, emitting a second photon in the process.

1.2 The Free-Electron Laser

The free-electron laser (FEL) is another powerful source of coherent electromagnetic (EM) radiation. Its operating principle is based on the interaction of a relativistic electron beam that passes and wiggles through a periodic magnetic field provided by the so-called *undulator*, see Fig. 1.2. In each bend, the electrons emit tiny flashes of light that add up to a strong laser-like pulse. The wavelength of the pulse λ_R is strongly blue-shifted due to the relativistic Doppler effect, depending on the electron beam energy, the undulator strength $K \propto B_0\lambda_u$ where B_0 is the peak magnetic field and the wavelength of the undulator field λ_u. This can be expressed as follows

$$\lambda_R = \frac{\lambda_u}{2\gamma^2}\left(1 + \frac{K^2}{2}\right), \tag{1.2}$$

where γ is the Lorentz factor which is a measure for the electron beam energy. The FEL is an attractive device because the radiated wavelength λ_R can be chosen simply by changing the electron beam energy γ. As opposed to conventional lasers, the tunability of FEL radiation is not dependent on the intrinsic material properties of the gain medium. Instead, the gain medium consists of free electrons, unbounded by atoms or molecules but an external magnetic field instead, and whose properties can be readily modified, resulting in outstanding tuning capabilities. In particular for producing coherent X-rays, an area where conventional lasers using material gain media become more challenging [3], the FEL is truly a unique and indispensable tool.

1.2.1 Radiation and microbunching

Radiation produced by FELs can be understood in the same terms as conventional lasers, despite the different underlying physical basis. Two types of radiation involved can be distinguished:

1. **Spontaneous emission** refers to the *incoherent* undulator radiation that an accelerating charge produces in an undulator field;

2. **Stimulated emission** involves electrons interacting with their own, additional *coherent* radiation field. If electrons lose energy to the radiation field and decelerate this could be

considered a form of stimulated emission. Oppositely, if electrons gain energy from the radiation field this is analogous to absorption.

FELs have sufficiently long undulators so that the incoherent undulator radiation (spontaneous emission) can trigger a periodic density modulation which causes electrons to radiate collectively and exponentially increases the coherent radiation intensity (stimulated emission) in a process called Self-Amplified Spontaneous Emission, or SASE. The key mechanism in SASE-FELs is that electrons start "communicating" with each other through their commonly produced (and growing) radiation field by exchange of energy. The combination of the undulator field and the counter-propagating radiation field results in a standing wave pattern which exerts a *ponderomotive force* on the electrons. Over sufficient interaction time, these ponderomotive forces modulate the (longitudinal) density so that electrons bunch up in small slices around the radiation wavelength. This process of micro-bunching and the resulting collective electron behaviour lead to coherent amplification, and lie at the heart of classical high-gain FELs, as is illustrated in Fig. 1.2.

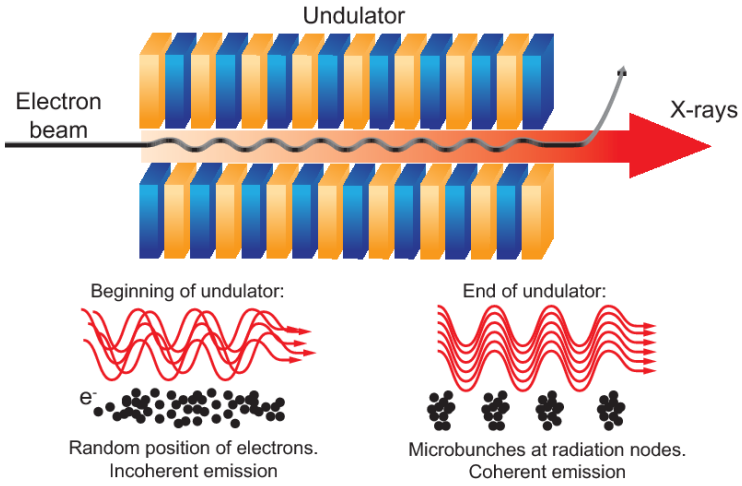

Figure 1.2: Overview of a basic FEL structure (top) [9]. Incoherent undulator radiation generated by randomly distributed electrons is amplified throughout the undulator and enables exponential growth of coherent emission from micro-bunched electrons (bottom).

Typically, FELs can be operated in the high-gain *Compton* or *Raman* regime [10]. In the Compton regime, the undulator field is strong such that the ponderomotive force fully dominates over the space-charge forces between electrons. In the Raman regime, space-charge effects play a substantial role in determining the radiation growth and efficiency, and thus cannot be neglected w.r.t. the ponderomotive force. This regime usually involves lower electron energies, high charge densities and a weaker undulator field. In either case, the physical basis of the FEL mechanism can be captured in a fully classical model, as opposed to the transitions between states within the quantum mechanical structure of a gain medium. The radically different involved dynamics make for a noisier spectrum, and is one of the reasons why FELs are often not considered true lasers.

1.2.2 Optical free-electron laser

At present, operational FELs are based on magnetostatic undulators where the periodic magnetic field is generated by arrays of alternating magnets of opposing polarity, as illustrated in Fig. 1.2 by the blue and yellow blocks. The generated undulator wavelength λ_u is therefore inherently limited to the size at which sufficiently strong magnets can be manufactured, which is typically on the cm scale. For the production of X-rays, we consequently need to bridge the wavelength gap from cm to nm by an extremely strong Doppler shift that is only associated with highly energetic electrons,

see Eq. (1.2). This high energy requires large accelerating structures which, combined with long undulators, has resulted in costly, specialized and large-scale FEL facilities such as LCLS(-II), FERMI, European XFEL, SwissFEL and TESLA [11].

Due to limited beam time at these facilities and increased demand for high-quality X-rays, the development of *compact* light sources has become more important over the past years. To this end, it has been proposed to use a laser pulse as an optical undulator. A schematic of this optical FEL (OFEL), where the electron bunch is depicted before, during and just after interacting with the laser pulse, is seen in Fig. 1.3. This type of undulator used in OFELs has a significantly smaller wavelength than the magnetostatic alternative, thereby requiring a significantly lower electron beam energy resulting in a much more compact FEL set-up. As the undulator is provided by a laser pulse that counter-propagates with respect to the electron beam instead of a static field, we modify the wavelength-relation from Eq. (1.2) by $\lambda_u \to \lambda_0/2$, now using the dimensionless electric field amplitude $a_0 = eE_0/mc\omega$ as the laser undulator parameter

$$\lambda_R = \frac{\lambda_0}{4\gamma^2}(1 + a_0^2) \tag{1.3}$$

To illustrate their advantage, optical FELs could operate at $\lambda_R = 1$ nm, $\lambda_0 = 1$ μm by using ~ 8 MeV electrons, opposed to approx. 4 GeV electrons in the case of a magnetostatic undulator at $\lambda_u = 5$ cm. In addition to their potential to shrink FELs down to table-top size, optical FELs are also suited, in theory, to produce radiation at even smaller wavelengths (hard X-rays and γ-rays) due to their lower energy requirement. Although the theoretical concept has already been proposed quite some time ago [12, 13], FEL microbunching still requires exceptional laser pulse and electron bunch properties in an experiment, making experimental realization a topic of ongoing research [14, 15, 16, 17], and on which will be elaborated later in Chapter 6.

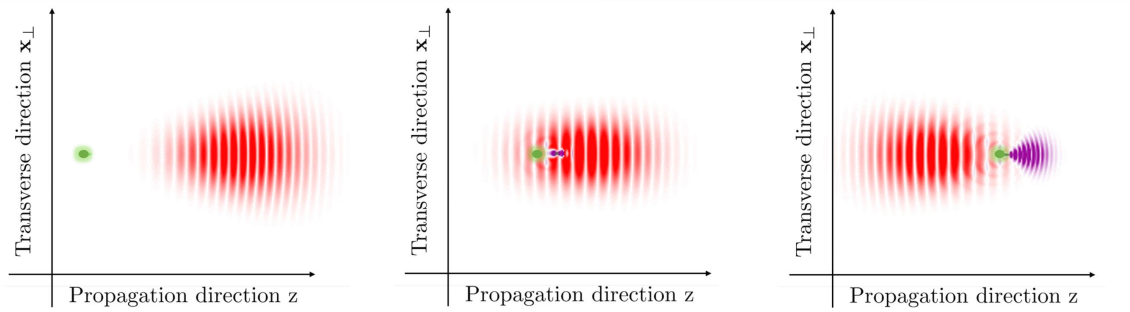

Figure 1.3: Optical FEL scheme: electron bunch (green) approaches laser pulse undulator (left); electron bunch oscillates in laser field and starts producing (incoherent) undulator radiation (center); ponderomotive force modulates density (as in Figure 1.2) producing a coherent radiation pulse (right).

1.3 The Quantum Free-Electron Laser

Conventional FELs operate in a regime that can be described fully classically, despite the fact that the original proposal by Madey was based on a quantum mechanical description [18]. A FEL based on an optical undulator, however, can access a regime in which the classical theory breaks down. The Quantum Free-Electron Laser (QFEL) operates in a regime where the quantum mechanical discreteness of the electron-light interaction is relevant, such that the underlying physical mechanism and radiation properties become very different from its classical counterpart. This section centers around a definition of this quantum regime and sets out the characteristics of QFELs.

1.3.1 Defining the quantum regime

In search of the quantum regime, we first consider the electron momentum spread. During FEL interaction, electrons exchange momentum with the radiation field according to the stimulated emission and absorption described in 1.2.1. This process modulates the electron momentum distribution and results in a FEL-induced momentum spread Δp in the electron phase-space. Fundamentally, the electron-light interaction is mediated by photons such that the momentum exchange is a discrete process described by a quantum theory, rather than a continuous process that only belongs to the quantum theory's classical limit. By explicitly comparing the amplitude of the FEL momentum modulation to a single-photon recoil (due to emission and absorption of radiation), we can use their ratio as a useful quantity that dictates the transition between the classical and quantum regime in FELs:

$$\bar{\rho} = \frac{\Delta p}{\hbar k_R}. \tag{1.4}$$

Later, we will derive an analytical expression for Δp. For classical FELs ($\bar{\rho} \gg 1$), the induced momentum spread is much larger than a single-photon recoil such that the fundamental discreteness of the interaction washes out completely and a classical theory suffices. In the quantum regime ($\bar{\rho} < 1$) however, this is not the case and momentum discreteness becomes important. From Eq. (1.4), we can conclude that this quantum regime can be accessed by a sufficiently small momentum spread Δp in combination with high single-photon momentum. Optical FELs are much better suited to meet these conditions compared to the current FELs based on magnetostatic undulators. First off, high photon momentum is achieved by reducing the radiation wavelength as far as possible (e.g. $\lambda_R = 0.1$ nm) for which optical FELs are generally better suited. Secondly, as the momentum spread is proportional to γ, it is also best to keep the electron energy as small as possible. The laser undulator in optical FELs allows the generation of short-wavelength radiation with much lower-energy electrons, and hence becomes instrumental in achieving the quantum FEL regime.

1.3.2 The current state of QFEL theory

The emergence of a quantum FEL regime immediately requires an updated quantum model of FELs that can account for the discrete nature of the momentum exchange [19]. In 2005, a first QFEL model was published by Bonifacio *et. al.* [6] which immediately showed features that were completely different from SASE in the classical regime. Most interestingly in this regime is the phenomenon of "quantum purification": the random spiking and large spectral width of classical SASE-FEL radiation [20] almost fully disappear and a strong narrowing of the spectrum occurs [21, 22], as if the FEL was driven by a coherent seed.

The first QFEL models [21, 22] are based on Maxwell-Schrödinger equations which couple a matter-wave function Ψ for the electrons to the classical radiation field, heavily inspired by existing Collective Atomic Recoil Lasing (CARL) models [23]. CARL is a form of light amplification based on Rayleigh scattering and the collective behaviour within a cold atomic gas [24], and has already been experimentally observed [25, 26]. This type of model also yields the simplest representation of the QFEL mechanism, and shows that, for sufficiently low values of $\bar{\rho}$, the wave function Ψ periodically switches between discrete electron momentum states very similar to a two-level quantum system in atomic lasers (see Fig. 1.1). Soon after, focus shifted to more comprehensive models based on the Wigner distribution function [27], which also could be more easily extended to a 3D geometry [28, 29]. Though a first 3D model has already been around for a while, simulation results are scarce and progress can still be made using 1D models to gain a deeper, more complete understanding of the dynamics at play. For example, it is crucially important to allow for decoherence of either spontaneous emission or space-charge to take place, having opposing experimental constraints [7]. Whilst spontaneous emission has been studied [30], the effects of space-charge in QFELs are largely unknown. This implies that all current models adopt the Compton regime where the QFEL process is negligibly influenced by the internal Coulomb inter-

actions, instead of a Raman regime. A complete theory would eventually have to account for the complete 3D kinetics, decoherence effects, and non-ideal electron and laser beam properties in a rigorous quantum mechanical model [7]. Such a model can subsequently be used for the design of a future experiment. Experimental considerations and challenges have already been discussed on multiple occasions [7, 31, 32] and generally conclude that required laser and electron sources for a QFEL set-up could come within reach of state-of-the-art technology. This makes thorough theoretical substantiation all the more important for the experimental realization of QFELs.

1.3.3 Future applications

The realization of QFELs is primarily motivated by applications and experiments using the highly coherent short X-ray pulses from a compact light source. The quantum purification process yields considerable improvements on the coherence lengths compared to existing hard X-ray sources. A drawback of QFELs is, however, that the stringent experimental conditions have direct consequences on the number of photons per pulse. At best, this equals the number of electrons ($\sim 10^5 - 10^{10}$), which is relatively low compared to large facilities ($\sim 10^{12}$) [33]. Nevertheless, QFELs can produce a combination of very small bandwidth and simultaneously well-defined ultrashort pulses with long coherence lengths, whereas classical SASE-FELs produce a shot-by-shot randomly distributed train of pulses [7]. Therefore, its unique type of light enables novel applications such as time-resolved, dynamical studies in structural matter using interferometric, or other phase-referenced methods. This could be used, for instance, to detect exotic states of matter undergoing instabilities on ultrashort timescales or rapid phase transitions in high phase-space density plasmas [7, 34]. Moreover, QFEL radiation could serve as a high-quality seeding source for subsequent amplification in a different set-up, which does not require high intensities.

1.4 Thesis outline

This thesis will serve as a partial review, but mainly a continuation of the currently existing QFEL theory based on analytical work and numerical simulations. To this end, we first give a review of classical FEL theory in Chapter 2 to introduce relevant concepts on which the QFEL physics is based. Chapter 3 is dedicated to presenting the quantum mechanical FEL theory in its current state and mathematically substantiating the QFEL dynamics. In Chapter 4, a novel addition to the theory is made as we study the effects of space-charge on QFELs. Although a comprehensive 3D theory lies outside the scope of this work, the most important elements of such a model are expanded on in Chapter 5. Finally, Chapter 6 will consider aspects of the experimental realization of future QFELs and its link to the ultra-cold electron source (UCES)/Coldlight project [35] at the CQT group in Eindhoven. Based on additions to and extensive simulations of the model described in this thesis, we gain novel insights into the workings and future realization of QFELs.

2 Classical FEL theory

In this chapter, the fundamentals of a classical high-gain FEL theory are reviewed. Next to familiarising the reader with the important concepts of a FEL, this chapter will lay the important groundwork on which the quantum-mechanical analysis is based. It will set off by deriving the equations of motion for an electron bunch in a ponderomotive wave.

2.1 Electron dynamics

The Hamiltonian framework is well-suited to study a wide variety of classical, dynamical systems formalized as point-particles with a canonical position $\mathbf{q}$ and momentum $\mathbf{p}$. At the heart of it lies the stationary-action principle expressed in Hamiltonian form as

$$\delta S = \delta \int_{t_1}^{t_2} \Big(\mathbf{p} \cdot \dot{\mathbf{q}} - \mathcal{H}(\mathbf{q}, \mathbf{p}) \Big) \mathrm{d}t = 0. \tag{2.1}$$

By setting up a Cartesian coordinate system $\mathbf{r} = (x, y, z)$ and $\mathbf{p} = (p_x, p_y, p_z)$, the direction in which the FEL interaction will predominantly take place is chosen as the z- direction. The action-principle can now conveniently be rewritten such that z serves as the independent variable and (x, y, t) and $(p_x, p_y, -E)$ are the new sets of canonical position and momentum variables

$$\delta \int_{z_1}^{z_2} \Big(p_x \frac{\mathrm{d}x}{\mathrm{d}z} + p_y \frac{\mathrm{d}y}{\mathrm{d}z} - E \frac{\mathrm{d}t}{\mathrm{d}z} + p_z \Big) dz = 0. \tag{2.2}$$

In its current form, the old Hamiltonian $\mathcal{H} = E$ coincides with the total electron energy, and Hamilton's equations apply to this new set of (in)dependent variables for a *new* Hamiltonian given by the longitudinal momentum $-p_z$. An expression for $-p_z$ is found using the (dimensionless) relativistic Hamiltonian for an electron with canonical momentum $\mathbf{p}$ interacting with an electromagnetic field described by an arbitrary vector potential $\mathbf{a}$

$$\mathcal{H} = \gamma = \sqrt{1 + (\mathbf{p} + \mathbf{a})^2} = \sqrt{1 + (\mathbf{p}_\perp + p_z \hat{\mathbf{z}} + \mathbf{a})^2}. \tag{2.3}$$

In this form, transverse momentum in x- and y-direction is combined in the variable $\mathbf{p}_\perp$. Now, it is useful to bring in specifics of the FEL interaction. First off, the total electromagnetic field in which electrons move around and interact with is composed of two fields: the laser (undulator) field and the radiation field. These fields are respectively characterized by transverse amplitudes $a_{L,R}(\mathbf{x}_\perp, z, t)$ and counter-propagate w.r.t. z with circular polarization according to $\hat{\boldsymbol{\epsilon}} = (\hat{\mathbf{x}} + i\hat{\mathbf{y}})/\sqrt{2}$. The sum of these two fields, also referred to as the *ponderomotive* wave, is expressed in dimensionless form as

$$\mathbf{a}(\mathbf{x}_\perp, z, t) = \frac{e\mathbf{A}}{mc} = \mathbf{a}_L + \mathbf{a}_R = \frac{\hat{\boldsymbol{\epsilon}}}{\sqrt{2}} \Big(a_L(\mathbf{x}_\perp, z) e^{-ik_L(z-ct)} - i a_R(\mathbf{x}_\perp, z) e^{ik_L(z+ct)} \Big) + c.c., \tag{2.4}$$

although we will make several approximations approriate for FELs. Now, Eq. (2.3) can be solved to derive an expression for p_z, that simultaneously serves as the new Hamiltonian $\mathcal{H}'$ of the

following form

$$\mathcal{H}'(\mathbf{x}_\perp, \mathbf{p}_\perp, ct, \gamma, z) = -p_z = -\gamma + \frac{1}{2\gamma}\Big(1 + |\mathbf{p}_\perp|^2 + |\mathbf{a}|^2\Big). \tag{2.5}$$

Because of the transverse polarization of $\mathbf{a}$, we are left with only one other, fast-oscillating cross-term $2(\mathbf{p}_\perp \cdot \mathbf{a})$ which can be neglected. In addition, the ultra-relativistic limit applies such that $\gamma \gg \sqrt{1 + |\mathbf{p}_\perp|^2 + |\mathbf{a}|^2}$. Having constructed this Hamiltonian, we can write down Hamilton's equations which lie at the basis of the electron dynamics in the ponderomotive field.

$$\frac{\mathrm{d}q_i'}{\mathrm{d}z} = \frac{\partial \mathcal{H}'}{\partial p_i'} \quad \Longrightarrow \quad \Big(\frac{\mathrm{d}\mathbf{x}_\perp}{\mathrm{d}z} = \frac{\partial \mathcal{H}'}{\partial \mathbf{p}_\perp}\Big), \quad \Big(\frac{\mathrm{d}t}{\mathrm{d}z} = -\frac{\partial \mathcal{H}'}{\partial E}\Big) \tag{2.6a}$$

$$\frac{\mathrm{d}p_i'}{\mathrm{d}z} = -\frac{\partial \mathcal{H}'}{\partial q_i'} \quad \Longrightarrow \quad \Big(\frac{\mathrm{d}\mathbf{p}_\perp}{\mathrm{d}z} = -\frac{\partial \mathcal{H}'}{\partial \mathbf{x}_\perp}\Big), \quad \Big(\frac{\mathrm{d}E}{\mathrm{d}z} = \frac{\partial \mathcal{H}'}{\partial t}\Big) \tag{2.6b}$$

These equations will now be worked out in order. One of the most important aspects of the electron dynamics in the ponderomotive wave is the longitudinal spatial modulation that constitutes the micro-bunching process. To illustrate this effect we first consider the Hamiltonian equation for transverse position $\mathbf{x}_\perp$ from Eq. (2.6a)

$$\frac{\mathrm{d}\mathbf{x}_\perp}{\mathrm{d}z} = \frac{\partial}{\partial \mathbf{p}_\perp}\left(-\gamma + \frac{1}{2\gamma}\Big[1 + \mathbf{p}_\perp^2 + |\mathbf{a}|^2\Big]\right) = \frac{\mathbf{p}_\perp}{\gamma}. \tag{2.7}$$

It is important to recall that $\mathbf{p}_\perp$ stands for the canonical momentum. Using the solution of Eq. (2.7), the transverse electron velocity can be written (in the paraxial approximation $\frac{\mathrm{d}\mathbf{x}_\perp}{\mathrm{d}z} \ll 1$) as

$$\boldsymbol{\beta}_\perp = \frac{\mathbf{a}}{\gamma} + \frac{\mathrm{d}\mathbf{x}_\perp}{\mathrm{d}z} \approx \frac{\mathbf{a}}{\gamma}. \tag{2.8}$$

Using this fact, we can explain the micro-bunching effect: as electrons lose energy to the radiation field, their energy γ reduces and transverse velocity $\beta_\perp$ grows, which means the electron undulates at a sinusoidal trajectory of greater amplitude. The opposite happens when the electrons gain energy from the field. This makes very explicit that the energy modulation induced by the ponderomotive field (which we will work out later in this chapter) alters the electron trajectories. This speeding up or slowing down eventually will result in a micro-bunch structure. Before we proceed, it is useful to work out the ponderomotive potential term using Eq. (2.4)

$$|\mathbf{a}|^2 = |\mathbf{a}_L + \mathbf{a}_R|^2 \approx |\mathbf{a}_L|^2 - i\Big(\mathbf{a}_L^* \mathbf{a}_R e^{i\vartheta} - c.c.\Big) \tag{2.9}$$

where we assumed that $|\mathbf{a}_R|^2 \ll |\mathbf{a}_L|^2$, and adopt the notation of the ponderomotive phase

$$\vartheta = (k_R + k_L)z - (k_R - k_L)ct. \tag{2.10}$$

This variable ϑ denotes the electron phase of the ponderomotive wave, which will be used as a measure for the each electron's position. Next, we will consider the Hamilton equation for the time variable t from Eq. (2.6a)

$$c\frac{\mathrm{d}t}{\mathrm{d}z} = 1 + \frac{1}{2\gamma^2}\Big[1 + \mathbf{p}_\perp^2 + |a_L|^2 - i\Big(a_L^* a_R e^{i\vartheta} - c.c.\Big)\Big], \tag{2.11}$$

which could also be used to write an expression for the longitudinal electron velocity:

$$\beta_z = \frac{1}{c}\frac{\mathrm{d}z}{\mathrm{d}t} \approx 1 - \frac{1}{2\gamma^2}\Big[1 + \mathbf{p}_\perp^2 + |a_L|^2 - i\Big(a_L^* a_R e^{i\vartheta} - c.c.\Big)\Big] \tag{2.12}$$

Finally, the third equation that we consider is the one for electron energy γ from Eq. (2.6b)

$$\frac{\mathrm{d}\gamma}{\mathrm{d}z} = \frac{1}{2\gamma}\frac{\partial}{\partial(ct)}\Big[|\mathbf{a}_L|^2 - i\Big(a_L^* a_R e^{i\vartheta} - c.c.\Big)\Big] = -\frac{k_R}{2\gamma}\Big(a_L^* a_R e^{i\vartheta} + c.c.\Big) \tag{2.13}$$

2.2 Radiation field dynamics

Next, we would like to describe the spatio-temporal evolution of the radiation potential $\mathbf{a}_R$. There is an additional, electrostatic self-field generated by the internal Coulomb interaction between electrons, i.e. space-charge forces, that is neglected for now. By doing so, the FEL theory will be presented in the Compton limit, which is a valid limit for high electron energies and moderate electron densities. Later, in Chapter 4, the effect of space-charge is brought back in and studied in a quantum FEL model. We first derive the evolution of the transverse radiation potential $\mathbf{a}_R$ with the Maxwell wave equation in the Coulomb gauge ($\nabla \cdot \mathbf{a}_R = 0$)

$$\Box \mathbf{a}_R = \Big(D^+ D^- + \boldsymbol{\nabla}_\perp^2\Big)\mathbf{a}_R = -\frac{\mu_0 e}{mc}\mathbf{J}_\perp, \tag{2.14}$$

where $D^\pm = \partial_z \pm c^{-1}\partial_t$ and we can express the current density $\mathbf{J}_\perp$ for a beam of $j = 1, .., N$ electrons as

$$\mathbf{J}_\perp = -ec\sum_{j=1}^{N} \boldsymbol{\beta}_\perp \delta^{(2)}\Big(\mathbf{x}_\perp - \mathbf{x}_{j,\perp}(t)\Big)\delta\Big(z - z_j(t)\Big) \tag{2.15}$$

Combining these results in the Slowly Varying Envelope Approximation (SVEA), i.e. the radiation amplitude a_R varies slowly over z and t compared to the radiation wavelength ω_R^{-1}, the second-order derivatives can be neglected in the longitudinal and temporal coordinates. This makes the LHS of Eq. (2.14)

$$\Big(D^+ D^- + \boldsymbol{\nabla}_\perp^2\Big)\mathbf{a}_R \simeq \sqrt{2}\hat{\boldsymbol{\epsilon}} k_R e^{ik_r(z-ct)}\left(D^+ + \frac{\boldsymbol{\nabla}_\perp^2}{2ik_R}\right)a_R + c.c. \tag{2.16}$$

The RHS, by substitution of the (non-approximated) transverse velocity $\boldsymbol{\beta}_\perp$ from Eq. (2.8) in Eq. (2.15), reads

$$-\frac{\mu_0 e}{mc}\mathbf{J}_\perp = \frac{e^2}{\epsilon_0 mc^2}\sum_{j=1}^{N}\left(\frac{a_L e^{-ik_l(z+ct)} - ia_R e^{ik_R(z-ct)}}{\sqrt{2}\gamma_j} + \frac{\mathrm{d}\mathbf{x}_\perp}{\mathrm{d}z}\right)\delta^{(2)}\Big(\mathbf{x}_\perp - \mathbf{x}_{j,\perp}(t)\Big)\delta\Big(z - z_j(t)\Big).$$

Combining the LHS and RHS and projecting the expression on the $\hat{\boldsymbol{\epsilon}}$-direction yields:

$$\left(D^+ + \frac{\boldsymbol{\nabla}_\perp^2}{2ik_R}\right)a_R = \frac{e^2}{2\epsilon_0 mc^2 k_R}\sum_{j=1}^{N}\left(\frac{a_L e^{-i\vartheta} - ia_R}{\gamma_j} + \frac{\mathrm{d}\mathbf{x}_\perp}{\mathrm{d}z}e^{-ik_R(z-ct)}\right)\delta^{(2)}\Big(\mathbf{x}_\perp - \mathbf{x}_{j,\perp}(t)\Big)\delta\Big(z - z_j(t)\Big). \tag{2.17}$$

For the last step, we define the transverse average over N electrons of an arbitrary function $S(\vartheta, \mathbf{x}_\perp)$ as

$$\langle S(\vartheta, \mathbf{x}_\perp)\rangle = \frac{A}{N}\sum_{j=1}^{N} S(\vartheta, \mathbf{x}_\perp)\delta^{(2)}\Big(\mathbf{x}_\perp - \mathbf{x}_{j,\perp}(t)\Big), \tag{2.18}$$

where A is the transverse section of the electron beam. Also, we average over a longitudinal dimension of several wavelengths long $L_b = r\lambda_R$, where L_b is the bunch length and r an integer. This way, the number of electrons is scaled with a beam volume $N/(AL_b) = n_e$ and the plasma frequency $\omega_p = \sqrt{e^2 n_e/\epsilon_0 m_e}$ can be introduced. This leads to the following form of the field evolution equation:

$$\left(D^+ + \frac{\boldsymbol{\nabla}_\perp^2}{2ik_R}\right)a_R = \frac{k_R}{2}\Big(\frac{\omega_p}{\omega_R}\Big)^2\left[\left\langle\frac{a_L e^{-i\vartheta}}{\gamma}\right\rangle - i\left\langle\frac{a_R}{\gamma}\right\rangle - \left\langle\frac{\mathrm{d}\mathbf{x}_\perp}{\mathrm{d}z}e^{-ik_R(z-ct)}\right\rangle\right]. \tag{2.19}$$

2.3 1D FEL Model

In the previous section, a closed set of equations, Eqs. (2.7), (2.11), (2.13) and (2.19), was derived that captured the full 3D evolution of the system. The one-dimensional approximation is, however, exhaustive for most of the FEL physics, and at the same time offers a very intuitive picture of the basic mechanisms at work. In this section, any dependence on transverse coordinates is dropped such that the variables only evolve along the propagation direction z and time t. In addition, the laser amplitude is considered constant $a_L(\mathbf{x}_\perp, z) = a_0$ and the radiation amplitude is approximated by $a_R(\mathbf{x}_\perp, z, t) \approx a_R(z, t)$. The evolution of the j-th electron's ponderomotive phase given in Eq. (2.10) can be written as

$$\frac{\mathrm{d}\vartheta_j}{\mathrm{d}z} = (k_R + k_L) - (k_R - k_L)c\frac{\mathrm{d}t_j}{\mathrm{d}z} = k_L\Big(\frac{\gamma_j^2 - \gamma_r^2}{\gamma_j^2}\Big) \approx 2k_L\eta_j \tag{2.20}$$

under the assumption that $\eta_j \ll 1$. In addition, the Hamiltonian equation from Eq. (2.11) is used and the relative energy deviation from resonance is introduced as $\eta_j = (\gamma_j - \gamma_r)/\gamma_r$. The resonant energy is given by $\gamma_r = \sqrt{k_R(1 + a_0)^2/4k_L}$ according to Eq. (1.3). Using Eq. (2.13), we can subsequently write the evolution of η_j as follows:

$$\frac{\mathrm{d}\eta_j}{\mathrm{d}\bar{z}} = -\frac{a_0 k_R}{2\gamma_r^2}\Big(a_R e^{i\vartheta_j} + a_R^* e^{-i\vartheta_j}\Big) \tag{2.21}$$

Finally, the radiation field from Eq. (2.19) is approximated in 1D by

$$\left(\frac{\partial}{\partial z} + \frac{\partial}{\partial(ct)}\right)a_R = \frac{a_0 k_R}{2\gamma_r}\Big(\frac{\omega_p}{\omega_R}\Big)^2\langle e^{-i\vartheta}\rangle. \tag{2.22}$$

Note that the center term of Eq. (2.19), $-i\langle a_R/\gamma\rangle$, is also neglected by assuming that a_R is small compared to a_L. In addition, the Compton limit ensures that $\gamma \approx \gamma_r$ such that $\langle e^{-i\vartheta}/\gamma\rangle \approx \langle e^{-i\vartheta}\rangle/\gamma_r$. Immediately, an interesting result arises: the radiation field evolution scales directly with the average of all electron phases, which we will here define as the bunching factor:

$$b = \frac{1}{N}\sum_{j=1}^{N} e^{-i\vartheta_j} = \langle e^{-i\vartheta}\rangle. \tag{2.23}$$

The bunching factor is a measure for the phase correlation between individual electrons and quantifies the quality of micro-bunching. For randomly distributed electrons, their phases are uncorrelated such that $b = 1/N$. Perfect micro-bunching on the radiation wavelength would increase the bunching factor value to maximally 1.

Universal scaling

The set of equations, Eqs. (2.20)-(2.22), which neatly couples the electron dynamics to the radiation field, lends itself well to so-called universal scaling [36]. This form of dimensionless scaling makes that no experimental parameters explicitly appear in the working equations, which allows for an easy and intuitive interpretation of the physical processes at work. It starts by defining the fundamental FEL parameter, also called the Pierce parameter:

$$\rho = \frac{1}{\gamma_r}\Big(\frac{a_0\omega_p}{4ck_L}\Big)^{2/3} \tag{2.24}$$

We use this specifically to rewrite the variables to the following dimensionless form: $p_j = \eta_j/\rho$, $A = (\omega_R/\omega_p\sqrt{\rho\gamma_r})a_R$, $\bar{z} = 2k_L\rho z = z/L_g$ where the gain length L_g denotes the characteristic FEL length scale, which gives

$$\frac{\mathrm{d}\vartheta_j}{\mathrm{d}\bar{z}} = p_j \tag{2.25a}$$

$$\frac{\mathrm{d}p_j}{\mathrm{d}\bar{z}} = -\left(Ae^{\vartheta_j} + A^* e^{-i\vartheta_j}\right) \tag{2.25b}$$

$$\frac{\partial A}{\partial \bar{z}} + \frac{\partial A}{\partial (c\bar{t})} = b \tag{2.25c}$$

The full electron phase space is coupled self-consistently to the radiation field amplitude in a completely parameter-less set of equations. In the remainder of this chapter, analytical and numerical solutions to these three equations will be treated. In addition, we present the physical interpretation of the FEL parameter ρ.

2.3.1 Linear stability, detuning of exponential gain

Eqs. (2.25a)-(2.25c) allow for a linear stability analysis of the stationary solutions, which can provide valuable insight into the FEL dynamics. This type of analysis allows characterization of the conditions under which instabilities around stationary solutions can occur. To this end, we introduce the detuning δ as an independent parameter that essentially forms the initial conditions for the p_j variables:

$$p_j(0) = p(0) = \delta = \frac{\gamma_0 - \gamma_r}{\rho \gamma_r}. \tag{2.26}$$

Physically, the detuning signifies the relative electron energy with respect to the resonant energy. For simplicity, we assume all electrons have the same energy γ_0 of which we will refer to as the cold-beam approximation. Later this assumption will be dropped. It is convenient to let the detuning explicitly appear in the equations as it is highly relevant for achieving exponential gain. This can simply be done by substitution of $p_j' = p_j - \delta$, $\vartheta_j' = \vartheta_j - \delta\bar{z}$ and $A' = Ae^{i\delta\bar{z}}$ in Eqs. (2.25a)-(2.25c), in which we transform to a comoving reference frame where electrons do not experience phase change because of the detuning. Immediately dropping the primes, this effectively only alters the field equation to

$$\frac{\partial A}{\partial \bar{z}} = b + i\delta A \tag{2.27}$$

where we also dropped the time-dependence for now. To proceed with the linear stability analysis, an additional momentum bunching variable $P = \langle pe^{-i\vartheta} \rangle$ is introduced as we follow the collective variable description from Refs. [37, 38]. We subsequently analyze the stability around a stationary point in the small-signal limit. This implies an initially small radiation amplitude $A \approx \Delta A$, and a minimal change in the electron variables $\vartheta_j \approx \vartheta_j(0) + \Delta\vartheta_j$, $p_j \approx \Delta p_j$ where $\Delta(..) \ll 1$. Substitution in the collective variable expressions for b and P, and a first-order expansion of $e^{i\Delta\vartheta_j}$ whilst assuming that $\langle e^{-i\vartheta(0)} \rangle = 0$, allows us to simplify the electron evolution equations to

$$\frac{\mathrm{d}b}{\mathrm{d}\bar{z}} = -iP \tag{2.28}$$

$$\frac{\mathrm{d}P}{\mathrm{d}\bar{z}} = -A. \tag{2.29}$$

In combination with Eq. (2.27), the three equations can be reduced to a single third-order differential equation of the form

$$\frac{\mathrm{d}^3 A}{\mathrm{d}\bar{z}^3} - i\delta \frac{\mathrm{d}^2 A}{\mathrm{d}\bar{z}^2} - iA = 0, \tag{2.30}$$

which can easily be solved using an Ansatz of the form $A \propto e^{i\Lambda\bar{z}}$. Substitution of the Ansatz yields a dispersion relation of the form

$$(\Lambda - \delta)\Lambda^2 + 1 = 0 \tag{2.31}$$

The three solutions for $\delta = 0$ are given by $\Lambda_1 = -1$, $\Lambda_2 = (\sqrt{3}i - 1)/2$ and $\Lambda_3 = -(\sqrt{3}i + 1)/2$, which respectively yield oscillatory, exponentially decaying and exponentially growing solutions for A. Filling out the Ansatz, it is evident that the imaginary part of Λ_3 constitutes exponential growth of the radiation field $A \propto e^{i\,\mathrm{Im}\{\Lambda_3\}\bar{z}} \propto e^{X>0}$. The conditions under which this collective instability can occur are fully determined by the detuning δ, being the only free parameter left in

the description. In Fig. 2.1, the growth rate is plotted as function of the detuning, and we observe that the optimal growth rate is achieved with all on-resonance electrons, for $\delta = 0$.

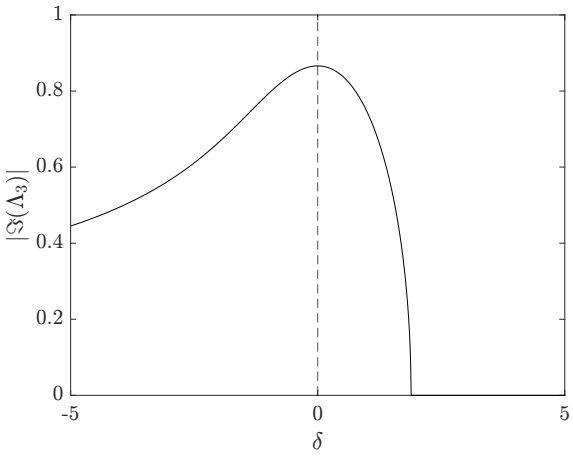

Figure 2.1: Growth rate against detuning. Dotted line indicates optimal value which is exactly on resonance ($\delta = 0$).

The linear stability analysis hereby shows that, for $\delta = 0$, collective instabilities occur in FEL interaction that leads to an exponential growth of the radiation amplitude. This will be further explained in the next section.

2.3.2 Steady-state instability

Having established exponential growth of the radiation field as one of the key characteristics of FEL action, we now turn to full numerical simulations only dropping time-dependence. In this steady-state regime, the evolution of the three variables is only considered with respect to $\bar{z}$. This approximation is valid for $\langle \beta_z \rangle \simeq 1$ or when the interaction time is short enough to neglect the velocity difference between light and electrons. Numerically solving Eqs. (2.25a)-(2.25c) using a Runge-kutta scheme (see Appendix A) yields the results seen in Fig. 2.2. Here we see the electron phase space $\{\vartheta_j, p_j\}$ as well as the radiation intensity $|A|^2$ and bunching $|b|$ against $\bar{z}$.

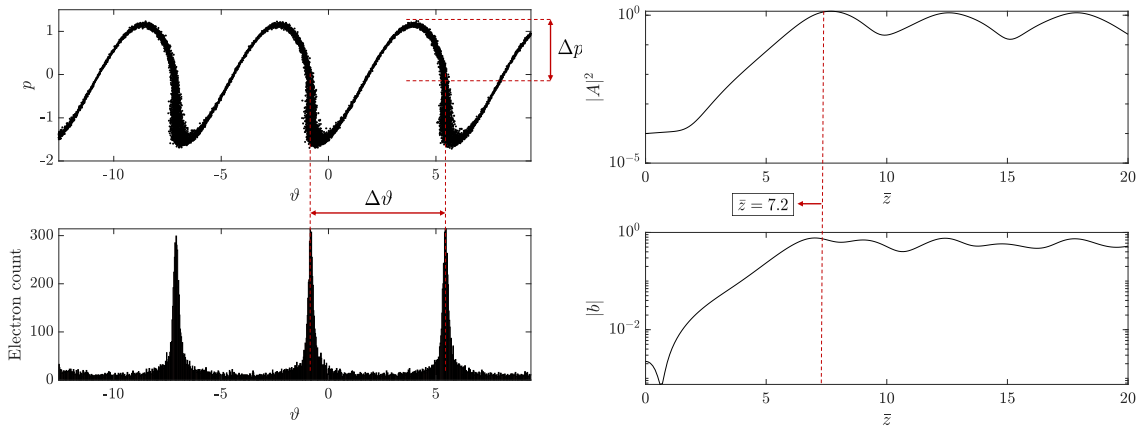

(a) (b)

Figure 2.2: (a) Electron phase space where each black dot is an electron at $\bar{z} = 7.2$ and (b) radiation intensity $|A|^2$ and bunching factor $|b|$ for $N = 3 \cdot 10^4$.

The simulation was initialized for a small non-zero field $A(\bar{z}=0) = 10^{-4}$ and $N = 3 \cdot 10^4$ electrons uniformly distributed in ϑ between $[-2\pi, 2\pi]$ and normally distributed around $p = 0$ with an rms width $\sigma_p = 0.1$. Let us start at Fig. 2.2(b); the exponential growth of the radiation intensity $|A|^2$, which was demonstrated in the previous section, is again clearly seen in the region between $\bar{z} = 0$ and $\bar{z} \approx 7$. The longitudinal evolution occurs along the normalized coordinate $\bar{z} = z/L_g$ such that the instability is paired with a characteristic length scale of gain lengths. This exponential growth turns into saturation in which oscillatory behaviour becomes dominant. The identical regimes, startup - exponential growth - saturation, are recognized in the evolution of the bunching factor, see Eq. (2.27). After saturation, both strong bunching and high intensities alternate in a chaotic fashion. As we consider the electron phase space $\{\vartheta_j, p_j\}$ specifically at the point of saturation $\bar{z} = 7.2$, high bunching is immediately recognized as the periodic vertical alignment in phase space, which the histogram of the electron density also clearly depicts. This emergent structure is known as micro-bunching, and the spacing between separate micro-bunches is on the order of an optical (radiation) wavelength:

$$\Delta\vartheta = 2\pi \quad \longrightarrow \quad \delta z = \frac{2\pi}{k_R + k_L} \approx \lambda_R. \tag{2.32}$$

The periodic density modulation around the radiation wavelength and consequent collective behaviour of radiating electrons is responsible for the exponential growth of the phase-correlated (coherent) radiation they produce. This is made even more clear in the histogram in Fig. 2.2(a) where electron count (which is a measure for density) is set out against ϑ. The electron phase space also exhibits energy modulation by the energy exchange of individual electrons with the radiation field, which is on the order of

$$\Delta p \sim 1 \quad \longrightarrow \quad \frac{\gamma - \gamma_r}{\gamma_r} = \frac{\Delta\gamma}{\gamma} \sim \rho \tag{2.33}$$

The FEL parameter ρ is thus a direct measure of the amplitude of the energy modulation induced by the FEL action.

2.3.3 Slippage

In reality, the electron bunches are not infinitely long so that time-dependence should be taken into account. It is instructive to see what time-dependence physically entails in a FEL system. Time-dependence essentially keeps track of the velocity difference between the electrons and the radiation they produce throughout the interaction over $\bar{z}$. By not taking this into account in the steady-state approximation, we effectively assume an infinitely long bunch. This so-called *slippage* has a substantial effect on the FEL interaction because the propagating radiation field interacts with different sections of the electron beam and thus requires evaluation of a spatial evolution on a *different* scale than gain lengths, but rather with respect to an internal bunch coordinate. This effect is strongest near the trailing edge of the e-beam; electrons produce radiation without being affected by radiation produced by any electrons behind [39]. To quantify this slippage, we introduce a second characteristic length scale, the cooperation length L_c, which is the distance the radiation slips in front of the electron bunch in one gain length:

$$L_c = \frac{\lambda_R}{8\pi\rho} = L_g \frac{1 - \beta_z}{\beta_z} \tag{2.34}$$

The time-derivative can be rewritten using a coordinate transformation to the co-moving electron frame $z_1 = (z - \beta_z ct)/L_c$

$$\frac{\partial}{\partial(ct)} \to \frac{\partial}{\partial z_1}. \tag{2.35}$$

Numerically this effect can be simulated by defining an electron bunch with a finite length of a number of cooperation lengths $L_b = nL_c$. When slippage is included in the equations, FELs can operate in the superradiant regime where the peak power scales as n_e^2.

2.4 Self-amplified spontaneous emission

Self-Amplified Spontaneous Emission, or SASE-FEL operation allows for (i) the steady-state instability and (ii) the superradiant scattering to occur from (iii) incoherent spontaneous emission, or noise. Rather than a coherent seed, the electron beam propagates through a sufficiently long undulator to initiate the coherent amplification by itself. The high-gain regime of SASE-FELs was first observed experimentally in the Livermore experiment for FELs in the microwave regime [40], and later in the X-ray regime at the LCLS [41]. The features of SASE-FEL radiation are determined by the characteristic length scales of the gain length L_g (i) and cooperation length L_c (ii) along with the electron bunch length L_b. As the cooperation length signifies the length scale over which electrons within a bunch can interact, a finite electron bunch is composed of L_b/L_c independent regions which radiate randomly and which give rise to a superradiant peak within each cooperation length [42]. Because of this, the resulting temporal radiation pulse has a (quasi-)chaotic structure, as is seen on the left in Fig. 2.3. We can subsequently investigate the spectral features by Fourier transformation of the temporal pulse:

$$\mathcal{F}\{|A(\bar{z}, z_1)|^2\} = P(\bar{z}, \bar{\omega}), \tag{2.36}$$

where $\bar{\omega} = (\omega - \omega_R)/\rho\omega_R$ with the resonant radiation frequency given by $\omega_R \approx 4\gamma_r^2\omega_L$. The resulting radiation spectrum is given on the right in Fig. 2.3. The shape of the resulting spectrum is spiky with the number of spikes an indication of the number of L_c in the bunch. Furthermore, the spectral width is broad compared to that of a transform-limited pulse. The chaotic spectrum of a classical SASE-FEL is one other reason that distinguishes FELs from conventional lasers, whose spectrum is ideally transform-limited. For shorter wavelengths, L_c further decreases (see Eq. (2.34) such that an electron bunch contains many independently radiating cooperation lengths with a broader spectral width as result. This is undesirable for coherent X-ray light source applications.

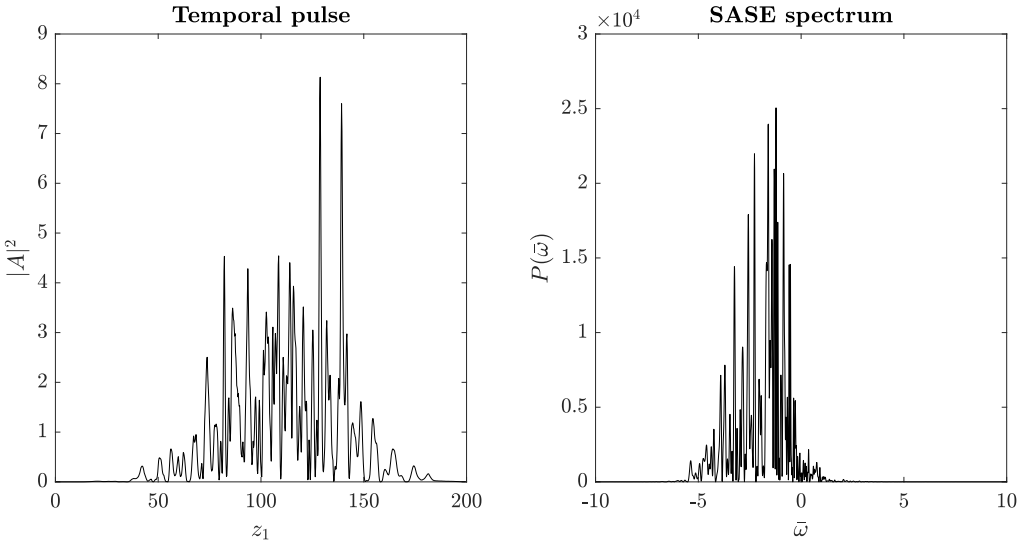

Figure 2.3: Temporal (left) and spectral (right) features of SASE radiation for $\bar{z} = 20$ and $L_b/L_c = 50$.

The spectral quality of SASE-FEL radiation could drastically be improved upon by quantum purification. Operation in the quantum regime avoids the spiking and chaotic behaviour and is therefore of utmost importance for future applications [6].

3 Quantum FEL theory

In this chapter, the FEL theory is modified to include the quantum mechanical nature of the electron-light interaction. After presenting a model for electron quantization in terms of momentum states, a more intuitive Wigner model is derived. Contrary to the first model, this Wigner model is more similar to the classical description and therefore better suited to study dynamics across the full breadth of the quantum-classical spectrum. Lastly, non-ideal and decoherence effects are introduced and implemented in the Wigner model.

3.1 From classical to quantum

In Chapter 1, an argument was made that the quantum mechanical nature of the interaction will start to emerge as the momentum spread Δp due to interaction will become on the order of a single-photon momentum. In Chapter 2, we found that this momentum spread can be written as $\Delta p = \gamma mc\rho$. By substitution of Δp in Eq. (1.4), a new parameter is automatically introduced, the QFEL parameter:

$$\bar{\rho} = \frac{\gamma mc}{\hbar k}\rho. \tag{3.1}$$

The QFEL parameter governs the transition between the classical and quantum regimes of FEL dynamics. In the classical regime ($\bar{\rho} \gg 1$), the momentum exchange and resultant momentum spread is much larger than a single photon recoil $\hbar k$ such that the momentum exchange can be interpreted, effectively, as a continuous process. The electrons follow continuous trajectories in phase space (see Fig. 3.1 (left)) to get to specific phase-space distributions such as the one in Fig. 2.2(a). In the quantum regime ($\bar{\rho} \ll 1$), the momentum spread induced by FEL action is on the scale of, or even smaller than $\hbar k$ such that the momentum exchange does not allow for a continuous description, which is illustrated in Fig. 3.1 (right) with a step-wise momentum ladder. The discrete nature of the momentum exchange between electrons and field should be properly accounted for in a quantum mechanical model. As both the electrons and electromagnetic field are fundamentally quantum objects, their classical description is replaced by a quantum mechanical one.

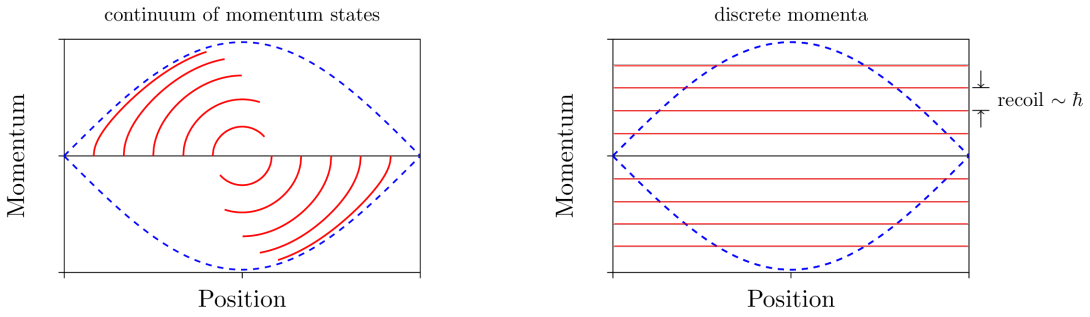

Figure 3.1: Schematic depiction of phase space evolution as continuous trajectories in the classical limit (left) and QFEL dynamics of discretized momentum separated by the photon recoil (right) [19].

3.1.1 Quantum electron dynamics

In acknowledging the limited applicability of treating the electrons as a classical point-charge distribution, a conceptual leap should be taken. In a quantum field theory (QFT) approach by G. Preparata [43], it was shown that for a large number of electrons FEL dynamics can be solved by a single-electron wave function $|\Psi\rangle$ obeying Schrödinger's equation in a self-consistent field[1]. To move towards such a description, we first explicitly introduce $\bar{\rho}$ to re-normalize p_j such that $\bar{p}_j = \bar{\rho} p_j$, and recognize the equivalence between the evolution equations for ϑ_j and $\bar{p}_j$ and Hamilton's equations:

$$\frac{\mathrm{d}\vartheta_j}{\mathrm{d}\bar{z}} = \frac{\bar{p}_j}{\bar{\rho}} = \frac{\partial \mathcal{H}_j}{\partial \bar{p}_j} \tag{3.2}$$

$$\frac{\mathrm{d}\bar{p}_j}{\mathrm{d}\bar{z}} = -\bar{\rho}\Big(Ae^{i\vartheta_j} + A^* e^{-i\vartheta_j}\Big) = -\frac{\partial \mathcal{H}_j}{\partial \vartheta_j} \tag{3.3}$$

Straight-forwardly, this implies that the (single-)electron dynamics can be associated with a Hamiltonian of the form

$$\mathcal{H}_j(\vartheta_j, \bar{p}_j) = \frac{\bar{p}_j^2}{2\bar{\rho}} - i\bar{\rho}\Big(Ae^{i\vartheta_j} - A^* e^{-i\vartheta_j}\Big) \tag{3.4}$$

At this point, the canonical nature of the theory allows immediate generalization of the Hamiltonian principle to quantum mechanics by relating the Poisson brackets for canonical variables to commutators for quantum operators:

$$[\hat{\vartheta}_j, \hat{p}_{j'}] = i\{\vartheta_j, \bar{p}_{j'}\} = i\delta_{jj'}. \tag{3.5}$$

Using this relation, the canonical variables can be replaced with a quantum position operator $\vartheta_j \to \hat{\vartheta}_j$ and momentum operator $\bar{p}_j \to -i\partial/\partial\vartheta_j$. The commutation relation can be easily checked knowing that a quantum operator in its most basic form is defined by action on its eigenstates. All in all, this allows us to write an expression for the total Hamiltonian operator $\mathcal{H}$ as

$$\mathcal{H} = \sum_{j=1}^{N} \mathcal{H}_j = \mathcal{H}_0 + \mathcal{H}_{int} = \frac{1}{2\bar{\rho}}\frac{\partial^2}{\partial\vartheta^2} - i\bar{\rho}\Big(Ae^{i\vartheta} - A^* e^{-i\vartheta}\Big), \tag{3.6}$$

We here observe that N electrons behave independently in an interaction potential captured by $\mathcal{H}_{int}$ which depends on the radiation field amplitude A. Rather than solving N equations for both operators $\hat{\vartheta}_j$ and $\hat{p}_j$, we can introduce a matter-wave function $|\Psi\rangle$ describing the electron bunch, on which our newly defined operators can act:

$$\langle\vartheta|\Psi\rangle = \Psi(\vartheta, \bar{z}) \tag{3.7}$$

$$\langle\vartheta|\,\hat{p}\,|\Psi\rangle = -i\frac{\partial\Psi(\vartheta,\bar{z})}{\partial\vartheta}, \tag{3.8}$$

and which evolves according to a (dimensionless) Schrödinger-like equation.

$$i\frac{\partial\,|\Psi\rangle}{\partial\bar{z}} = \mathcal{H}\,|\Psi\rangle\,. \tag{3.9}$$

Filling out Eq. (3.9) whilst projecting the wave function and momentum operator on the position $\langle\vartheta|$ basis makes that the single-electron wave function evolves according to

$$i\frac{\partial\Psi(\vartheta,\bar{z})}{\partial\bar{z}} = -\frac{1}{2\bar{\rho}}\frac{\partial^2\Psi(\vartheta,\bar{z})}{\partial\vartheta^2} - i\bar{\rho}\Big(Ae^{i\vartheta} - A^* e^{-i\vartheta}\Big)\Psi(\vartheta,\bar{z}). \tag{3.10}$$

[1]Note that the EM field will not be quantized, making the analysis semi-classical in nature.

3.2 Momentum state model

From Fig. 3.1, it is evident that the electron wave function cannot take on every value of momentum, but instead is limited by a discreteness inherent to the photon-mediated momentum exchange. This implies that the wave function Ψ can only occupy discrete momentum states which are spaced $\hbar k$ apart. The momentum state model is centered around a wave function decomposition in momentum eigenstates $\langle\vartheta|m\rangle = (2\pi)^{-1/2}e^{im\vartheta}$, which satisfy the eigenvalue equation:

$$\hat{p}\,|m\rangle = m\,|m\rangle\,. \tag{3.11}$$

The wave function can subsequently be (Fourier) expanded in terms of the momentum eigenstates

$$\Psi(\vartheta,\bar{z}) = \frac{1}{\sqrt{2\pi}}\sum_{m=\infty}^{\infty} c_m(\bar{z})e^{im\vartheta}, \tag{3.12}$$

More specifically, $|c_m|^2$ represents the probability of an electron having momentum $(\gamma_0-\gamma)m_ec = m\hbar k$. Substitution of this wave function expansion in Eq. (3.10) yields an evolution equation for the momentum state coefficients of the form

$$\frac{\mathrm{d}c_m}{\mathrm{d}\bar{z}} = -i\frac{m^2}{2\bar{\rho}}c_m - \bar{\rho}\Big(Ac_{m-1} + A^*c_{m+1}\Big). \tag{3.13}$$

The electron evolution due to the FEL interaction is now fully described in terms of population exchange between different electron momentum states mediated by photon exchange of $\hbar k$. The bunching factor b in the quantum description is not given by an ensemble average, but instead by the expectation value of $e^{-i\vartheta}$ of the continuous probability distribution $P = |\Psi|^2 = \Psi\Psi^*$. Using this, the bunching factor in the momentum state model is given by

$$b = \int_0^{2\pi}\Psi\Psi^*e^{-i\vartheta}\mathrm{d}\vartheta = \frac{1}{2\pi}\int_0^{2\pi}\Big(\sum_{m=-\infty}^{\infty}c_me^{im\vartheta}\sum_{m'=-\infty}^{\infty}c^*_{m'-1}e^{-im'\vartheta}\Big)\mathrm{d}\vartheta = \sum_m c_mc^*_{m-1} \tag{3.14}$$

Up to here, we have seen that the evolution of the radiation field amplitude is classically driven by the spatial micro-bunching of electrons, see Eq. (2.27). Here, by switching to a momentum state model, an equivalence is demonstrated between the spatial bunching of electrons and the coherence between neighbouring momentum states occupied by the electron wave function. The radiation field amplitude now evolves as

$$\frac{\partial A}{\partial\bar{z}} + \frac{\partial A}{\partial z_1} = \sum_m c_mc^*_{m-1} + i\delta A. \tag{3.15}$$

Together with Eq. (3.13), these equations form the basis of the momentum state model that can describe FEL interaction for every value of $\bar{\rho}$, and is thus capable of describing the quantum regime. In what follows, and identical to the classical approach, we perform a linear stability analysis, steady-state simulations and time-dependent simulations to obtain analytical and numerical solutions to these equations.

3.2.1 Linear stability analysis

As with the classical case, a linear analysis is extremely useful to characterize the conditions under which an instability around stationary solutions can occur. We consider a similar small-signal limit with a stationary point of the form $A \approx \Delta A$, $c_0 \approx 1 + \Delta c_0$ and $c_{m\neq 0} \approx \Delta c_m$. We can plug the small-signal approximation directly in Eqs. (3.13) and (3.15), leaving us with the following three equations

$$\frac{\mathrm{d}c_1}{\mathrm{d}\bar{z}} = -i\frac{1}{2\bar{\rho}}c_1 - \bar{\rho}A \tag{3.16a}$$

$$\frac{\mathrm{d}c_{-1}}{\mathrm{d}\bar{z}} = -i\frac{1}{2\bar{\rho}}c_{-1} + \bar{\rho}A \tag{3.16b}$$

$$\frac{\mathrm{d}A}{\mathrm{d}\bar{z}} = c_1 + c_{-1}^* + i\delta A, \tag{3.16c}$$

which are again analytically solvable. Rewritten to a single third-order equation

$$\frac{\mathrm{d}^3A}{\mathrm{d}\bar{z}^3} = -\frac{1}{4\bar{\rho}^2}\left(\frac{\mathrm{d}A}{\mathrm{d}\bar{z}} - i\delta A\right) + iA + i\delta\frac{\mathrm{d}^2A}{\mathrm{d}\bar{z}^2} \tag{3.17}$$

and solving with the same Ansatz of $A \propto e^{i\Lambda\bar{z}}$ yields a dispersion relation of the following form:

$$(\Lambda - \delta)\left(\Lambda^2 - \frac{1}{4\bar{\rho}^2}\right) + 1 = 0, \tag{3.18}$$

which is identical to Eq. (2.31) for $\bar{\rho} \to \infty$. The FEL-induced energy spread is sufficiently large such that discreteness washes out and a classical description is valid. However, as the imaginary part of the exponential growing mode $|\mathrm{Im}\{\Lambda_3\}|$ is plotted against δ for different values of $\bar{\rho}$ in Fig. 3.2, we observe something interesting. Where for $\bar{\rho} = 5$ the curve overlaps almost perfectly with the classical result, for smaller $\bar{\rho}$ the region of gain decreases in height and overall size. From Eq. (3.18) can be derived that the maximum gain occurs for $\delta_{max} \approx 1/2\bar{\rho}$ such that $(\gamma_0 - \gamma_r) \approx \hbar k/2mc$ and the gain width is proportional to $4\sqrt{\bar{\rho}}$. This has two practical implications. Firstly, for QFEL interaction to show exponential gain, electrons need to be detuned to within the bandwidth of the gain region. Secondly, even with proper detuning, only a decreased growth rate can be reached compared to the classical case.

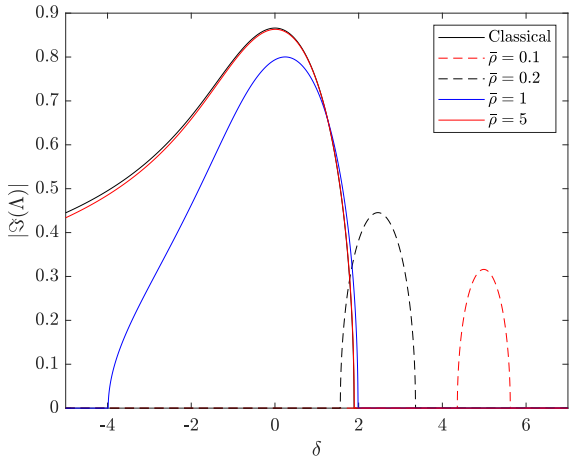

Figure 3.2: Growth rate against detuning for different values of $\bar{\rho}$.

3.2.2 Steady-state regime

Next, we turn to the steady-state solutions of Eqs. (3.13) and (3.15) where we first consider the deep quantum regime ($\bar{\rho} = 0.2$). We initialize the system such that $c_0(\bar{z} = 0) = 1 - \epsilon^2$ and $c_{-1}(\bar{z} = 0) = \epsilon^2$, where $\epsilon \ll 1$ signifies some random shot noise. Physically, this shot noise would be caused by spontaneous emission. Since spontaneous emission is not (yet) contained within the current model, we have to mimic its effect in simulation by adding a small, non-zero probability of decay to the lower momentum state. We also start with zero field ($A(\bar{z} = 0) = 0$) and a detuning $\delta = 1/(2\bar{\rho}) = 2.5$ consistent with the linear analysis. The occupation probabilities $|c_m|^2$ at three $\bar{z}$-positions, and the normalized intensity $\bar{\rho}|A|^2$ and bunching against $\bar{z}$ are plotted in Fig. 3.3.

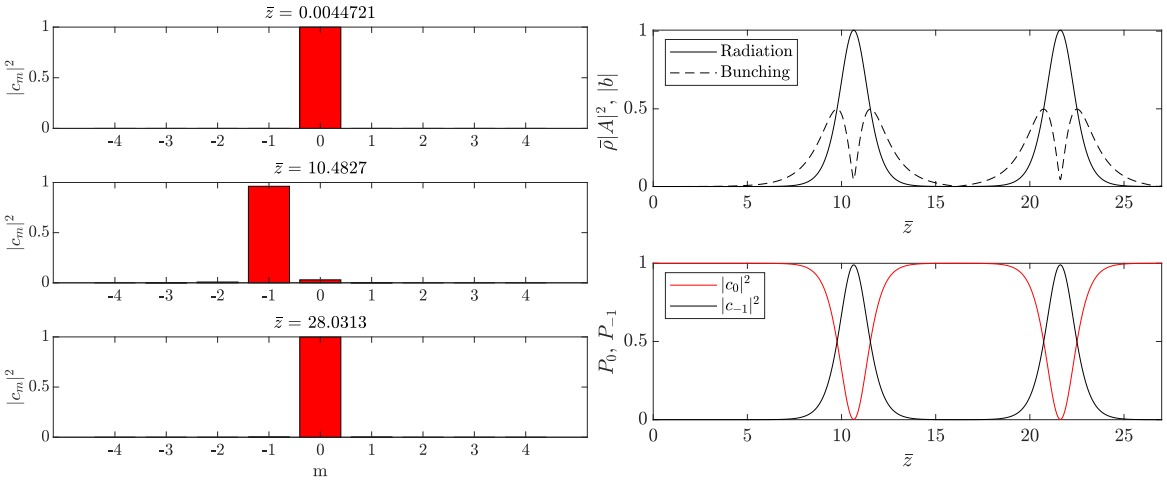

(a) (b)

Figure 3.3: Quantum regime ($\bar{\rho} = 0.2$): (a) Occupation probabilities for different values of $\bar{z}$, (b) normalized radiation intensity and bunching factor (top) and occupation probabilities (bottom) against $\bar{z}$.

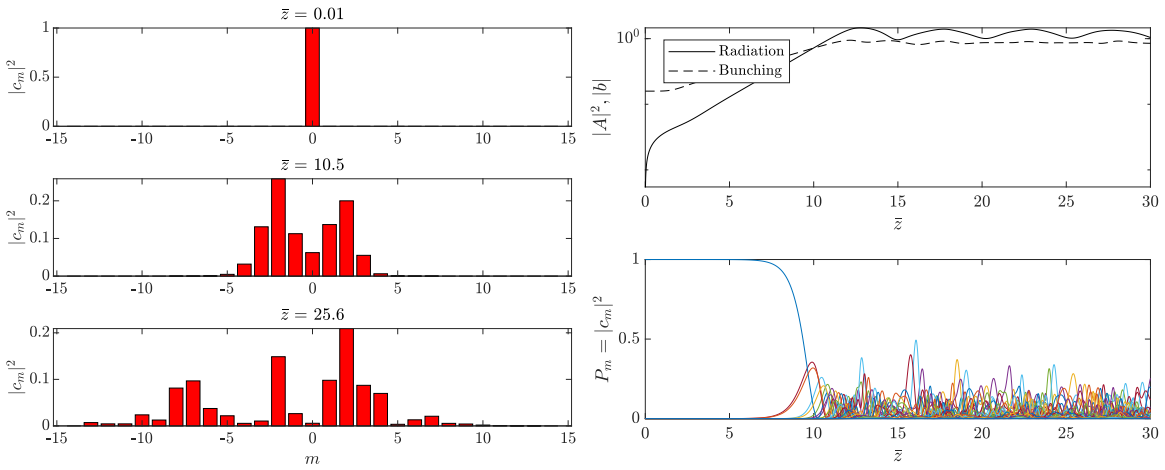

(a) (b)

Figure 3.4: Classical regime ($\bar{\rho} = 5$): (a) Occupation probabilities for different values of $\bar{z}$, (b) normalized radiation intensity and bunching factor (top) and occupation probabilities (bottom) against $\bar{z}$.

First off, we observe in Fig. 3.3(b) that the system again shows a collective instability and exponential growth of the radiation intensity in the region from $0 < \bar{z} \lesssim 10.5$, as the linear analysis suggested. The intensity evolution is, however, very different from the classical result in Fig. 2.2(b). Rather than the oscillatory behaviour after saturation as seen classically, the intensity in the quantum regime evolves as sequential pulses. We start with full occupation of the c_0 momentum state followed by a region of exponential growth during which the occupation of c_{-1} grows. This exponential growth terminates as both the occupation of the c_{-1} state and the radiation intensity reach saturation, where the intensity is normalized such that $\bar{\rho}|A|^2 = 1$ represents the emission of

a single photon per electron. Subsequently, the radiation is absorbed when the wave function fully transitions back to c_0. During the interaction, the population keeps cycling periodically between these two states emitting a radiation pulse during each transition. We observe a field driven by the coherence between adjacent momentum states. Next, we will consider a classical limit case for $\bar{\rho} = 5$ and $\delta = 0$ under the same initial conditions in Fig. 3.4. It is immediately evident that during the interaction, more momentum states get involved. The different colors in Fig. 3.4 on the bottom-right also show that transitions between a large number of momentum states occur chaotically in the saturation regime from $\bar{z} > 10$. As a result, the intensity evolves very similarly to the classical model from Fig. 2.2(b). It is perhaps surprising that the behaviour already resembles the classical model to this extent, especially since the number of involved momentum states is still relatively low. The momentum distribution is far from continuous and discreteness is still clearly visible nevertheless, the radiation profile that results from this chaotic pattern of transitions is already hard to distinguish from classical theory.

INTERMEZZO: Connection to the atomic laser

In Chapter 1, it was already brought up that FELs are often not considered true lasers since they rely on collective Compton scattering instead of coherent transitions within the quantum mechanical structure of a gain medium. What the momentum state model already makes clear is that FEL operation in the quantum regime leaves us with Rabi-like oscillations in an effective two-level system driven by the emission of photons of a fixed wavelength. The quantum FEL regime starts to behave like a system described by the optical Bloch equations well-known in laser physics [44]. This is illustrated in Fig. 3.5.

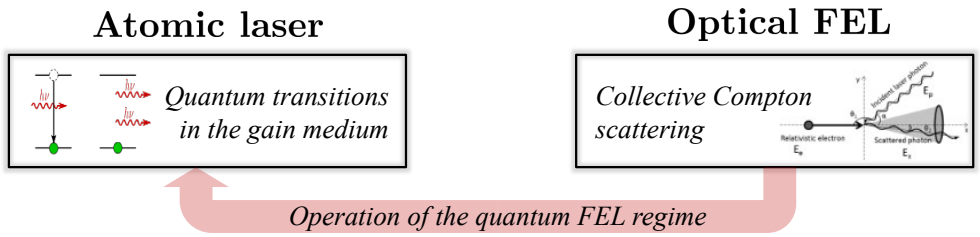

Figure 3.5: QFEL resembles the atomic laser.

3.2.3 Quantum purification

Similar to the classical approach, we now include slippage with an additional z_1-dependence of the radiation amplitude such that we can study the temporal and spectral features of SASE-QFEL in more detail. This is even more exciting because we can quantify the spectral advantage of QFELs over classical FELs due to the quantum purification. The temporal radiation pulse and the corresponding spectrum as found through numerical integration of Eqs. (3.13)-(3.15) for $\bar{\rho} = 0.2$ are plotted in Fig. 3.6. Here, we observe a significant spectral narrowing compared to the chaotic, broad classical spectrum from Fig. 2.3.

To give an explanation of the spectral narrowing in the quantum regime, we first restate the origin of the broad and spiky spectrum for classical SASE. In general, radiation is produced due to transitions between neighbouring momentum states ($|c_m|^2 = m\hbar k$) which leads to equally spaced emitted frequencies proportional to the difference between the associated kinetic energies. For large $\bar{\rho}$, a large number of momentum states gets occupied such that many different transitions occur resulting in a spectrum that contains a large number frequencies and has an envelope width proportional to the FEL-induced modulation amplitude from Eq. (2.33):

$$\left(\frac{\Delta\omega}{\omega}\right)_{\mathrm{cl}} = 2\frac{\Delta\gamma}{\gamma} \sim 2\rho \tag{3.19}$$

The FEL-induced modulation occurs for all electrons with an initial energy that falls within the gain bandwidth from the linear analysis (see Fig. 3.2). The different electron energies contained within that bandwidth, therefore, lead to the large number of sequential transitions randomly occurring, which explains the resulting broad multi-line spectrum. The number of spikes N_s can be approximated using the fact that radiation is emitted in a time of $t_b = L_b/c$, such that the corresponding width of a single frequency peak can be written as

$$\left(\frac{\Delta\omega}{\omega}\right) \approx \frac{\lambda_R}{L_b} \tag{3.20}$$

In combination with Eq. (3.19), the number of spikes $N_s = 2\rho L_b \lambda_R = L_b/(2\pi L_c)$ which is consistent with section 2.4. Now, for the quantum regime ($\bar{\rho} < 1$) the FEL-induced modulation amplitude Δp is *by definition* smaller than $\hbar k$ such that only a single transition between two adjacent states can occur, leading to a single frequency spike in the spectrum with a width of $\Delta\omega/\omega \approx \lambda_R/L_b$. Hence we can understand that QFELs inherently produce transform-limited, thus fully temporally coherent radiation. For instance, for pico-second bunches which radiate at $\lambda_R \approx 0.1$ nm, the QFEL bandwidth is on the order of 10^{-7} compared to 10^{-3} for the classical SASE spectrum given typical values for $\rho \sim 10^{-4}$. This spectral improvement of several orders of magnitude makes QFELs extremely interesting for high resolution studies in the structure of matter and warm-dense matter physics among other things [7, 45].

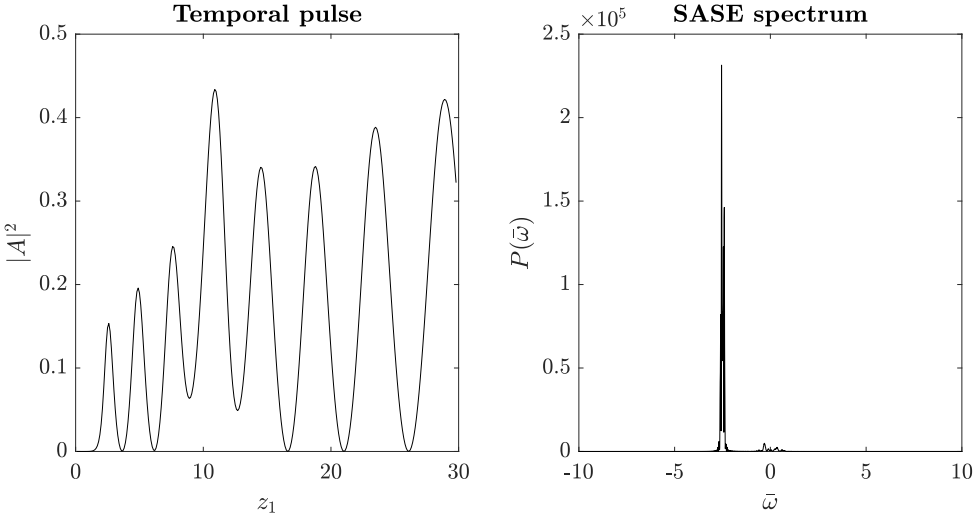

Figure 3.6: Temporal (left) and spectral (right) features of SASE-QFEL radiation at $\bar{z} = 60$ and $L_b/L_c = 30$.

3.2.4 Degree of longitudinal coherence

The time-dependent solution of the radiation field allows for a spectral analysis, which is useful to study the quantum purification in more detail. Here, we quantify the longitudinal coherence of a FEL as function of $\bar{\rho}$ by explicitly calculating the longitudinal coherence properties of QFEL radiation. To this end, the first-order spectral correlation function is defined as [46]

$$g^{(1)}(\omega, \omega', \bar{z}) = \frac{\langle \hat{A}(\omega, \bar{z}) \hat{A}^*(\omega', \bar{z}) \rangle}{\sqrt{\left\langle \left| \hat{A}(\omega, \bar{z}) \right|^2 \right\rangle \left\langle \left| \hat{A}(\omega', \bar{z}) \right|^2 \right\rangle}}. \tag{3.21}$$

Using this, the degree of longitudinal coherence (DLC) ζ can be determined using

$$\zeta = \frac{\iint \left| g^{(1)}(\omega, \omega') \right|^2 I(\omega) I(\omega') \mathrm{d}\omega \mathrm{d}\omega'}{\left[\int I(\omega) \mathrm{d}\omega \right]^2} \tag{3.22}$$

where $I(\omega) = \left\langle \left| \hat{A}(\omega, \bar{z}) \right|^2 \right\rangle$. In Fig. 3.7, we plot the DLC against $\bar{\rho}$ where we see a considerable decrease as $\bar{\rho}$ grows larger and we exit the quantum regime.

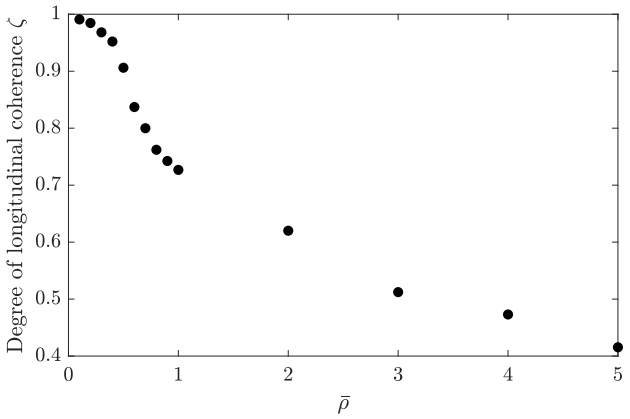

Figure 3.7: DLC against $\bar{\rho}$

3.3 Wigner distribution function model

The wave function model describes the momentum state dynamics clearly from the deep quantum to the classical regime, resulting in distinct evolution of the radiation intensity. However, in comparison with the classical model, the phase-space representation is lost. For the classical regime, the number of involved momentum states m is very large such that the discreteness between individual states is irrelevant. The (deep) quantum regime only involves the bare minimum number of momentum states ($m = 2$) that could still show meaningful dynamics. In order to observe the quantum-to-classical transition, however, just stating that "the number of involved momentum states increases" (see Fig. 3.8) would not do justice to the dynamics at play, whilst our current model is only equipped to do just that.

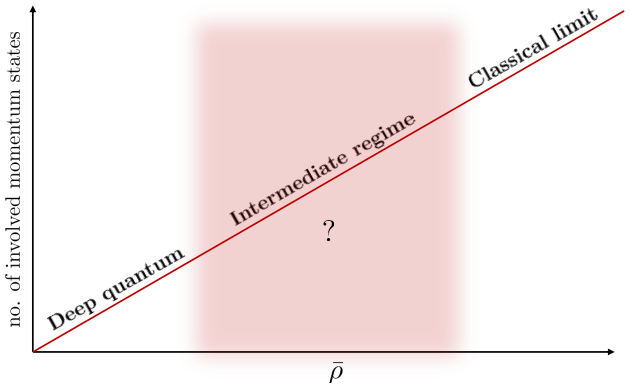

Figure 3.8: The transition from quantum to classical in terms of momentum states.

To this end, we will now move to a Wigner distribution function model that is better able to also capture the intermediate regime and whose equation explicitly shows a classical limit. Wigner models can represent the full quantum state in a description more similar to classical phase space without loss of information [47], thereby allowing for a more intuitive representation of the dynamics across all regimes. The Wigner function is also not limited to describing perfectly coherent particle samples, but also admits mixed quantum states which seems to be more representative

for the thermal electron beams in FELs. Thirdly, as will become more evident in Chapter 5, the Wigner formalism may easily be extended to a 3D geometry that includes transverse electron dynamics. Whilst the Wigner function has a myriad of applications in other fields [48], we will here restrict ourselves to a brief derivation purely in the context of QFELs.

3.3.1 Continuous Wigner model

The Wigner distribution function in the context of quantum mechanics effectively links a wave function to a probability distribution in phase space. More specifically, the density operator $\hat{\varrho}$ is considered, which can be defined for either a pure of mixed state

$$\text{Pure:} \quad \hat{\varrho} = |\Psi\rangle\langle\Psi| \qquad \text{Mixed:} \quad \hat{\varrho} = \sum_i c_i |\Psi_i\rangle\langle\Psi_i| . \tag{3.23}$$

This operator on a infinite-dimensional complex vector space, can be described with the same level of rigor as a *real* function on classical phase space. The Wigner distribution function is generally defined for a conjugate variable pair q and p as [49]

$$\mathcal{W}(q,p,t) = \frac{1}{\pi\hbar}\int_{-\infty}^{\infty} \langle q+q'|\,\hat{\varrho}\,|q-q'\rangle\, e^{-2ipq'/\hbar}\mathrm{d}q' = \frac{1}{\pi\hbar}\int_{-\infty}^{\infty} \langle p+p'|\,\hat{\varrho}\,|p-p'\rangle\, e^{-2ip'q/\hbar}\mathrm{d}p' \tag{3.24}$$

In the context of time-dependent FEL theory, our conjugate variables are the ponderomotive phase ϑ and relative energy deviation p, and include a dependency over the two, by now familiar, length scales: the undulator length $\bar{z}$ normalized in units of gain length L_g and the internal bunch coordinate $\bar{z}_1$ normalized to a cooperation length L_c. If we momentarily assume a pure quantum state, this results in the following

$$\mathcal{W}(\vartheta,p,\bar{z},\bar{z}_1) = \frac{1}{\pi}\int_{-\infty}^{\infty} \langle \vartheta+\vartheta'|\,\hat{\varrho}\,|\vartheta-\vartheta'\rangle\, e^{-2ip\vartheta'}\mathrm{d}\vartheta' = \frac{1}{\pi}\int_{-\infty}^{\infty} \Psi^*(\vartheta-\vartheta',\bar{z})\Psi(\vartheta+\vartheta',\bar{z})e^{-2ip\vartheta'}\mathrm{d}\vartheta' \tag{3.25}$$

Steady-state evolution of the electron dynamics is now captured by the evolution of the corresponding Wigner function $\mathcal{W}$

$$\frac{\partial\mathcal{W}}{\partial\bar{z}} = \frac{1}{\pi}\int_{-\infty}^{\infty}\left(\frac{\partial\Psi^*(\vartheta-\vartheta')}{\partial\bar{z}}\Psi(\vartheta+\vartheta') + \Psi^*(\vartheta-\vartheta')\frac{\partial\Psi(\vartheta+\vartheta')}{\partial\bar{z}}\right)e^{-2ip\vartheta'}\mathrm{d}\vartheta'. \tag{3.26}$$

This expression contains the evolution equation of the electron wave function, which we already derived before. It can be shown that substitution of Eq. (3.10) in Eq. (3.26) yields [27]

$$\frac{\partial\mathcal{W}}{\partial\bar{z}} = -\bar{p}\frac{\partial\mathcal{W}}{\partial\vartheta} + \bar{\rho}\Big(Ae^{i\vartheta} + A^*e^{-i\vartheta}\Big)\Big\{\mathcal{W}\Big(\vartheta,\bar{p}+\frac{1}{2\bar{\rho}},\bar{z}\Big) - \mathcal{W}\Big(\vartheta,\bar{p}-\frac{1}{2\bar{\rho}},\bar{z}\Big)\Big\}, \tag{3.27}$$

where $\bar{p} = p/\bar{\rho}$. It can be proven that, due to linearity of the statistical operator $\hat{\varrho} = \sum_i p_i |\Psi_i\rangle\langle\Psi_i|$, the same equation also holds for mixed states [27]. The coupling to the radiation field can be done analogous to the wave function model with an expectation value expression for the phase factor in terms of the Wigner function:

$$\frac{\mathrm{d}A}{\mathrm{d}\bar{z}} = \int_{-\infty}^{\infty}\mathrm{d}\vartheta\int_{-\infty}^{\infty}\mathcal{W}(\vartheta,p,\bar{z})e^{-i\vartheta}\mathrm{d}p + i\delta A \tag{3.28}$$

Here, we can also demonstrate one of the aforementioned advantages of the Wigner equation compared to the momentum state equation (see Eq. (3.13)). In the classical limit $\bar{\rho}\to\infty$, the third term in Eq. (3.27) reduces to

$$\lim_{\bar{\rho}\to\infty}\bar{\rho}\Big\{\mathcal{W}\Big(\vartheta,\bar{p}+\frac{1}{2\bar{\rho}},\bar{z}\Big) - \mathcal{W}\Big(\vartheta,\bar{p}-\frac{1}{2\bar{\rho}},\bar{z}\Big)\Big\} = \frac{\partial\mathcal{W}}{\partial p}, \tag{3.29}$$

such that the equation becomes a Vlasov equation that is explicitly consistent with the classical equations for ϑ and p from Eqs. (2.25a)-(2.25b):

$$\frac{\partial \mathcal{W}}{\partial \bar{z}} + p\frac{\partial \mathcal{W}}{\partial \vartheta} - \left(Ae^{i\vartheta} + A^* e^{-i\vartheta}\right)\frac{\partial \mathcal{W}}{\partial p} = \frac{\partial \mathcal{W}}{\partial \bar{z}} + \frac{\partial \mathcal{W}}{\partial \vartheta}\underbrace{\frac{\mathrm{d}\vartheta}{\mathrm{d}\bar{z}}}_{(2.25a)} + \frac{\partial \mathcal{W}}{\partial p}\underbrace{\frac{\mathrm{d}p}{\mathrm{d}\bar{z}}}_{(2.25b)} = 0. \tag{3.30}$$

Unfortunately, there is still one element missing. In the above derivation, it is both assumed that ϑ is unbounded while the ponderomotive phase is in fact periodic in $(0, 2\pi)$, and p is continuous, whilst electron recoil is associated with discrete momentum transitions. As opposed to a classical picture, in quantum mechanics, the periodicity and discreteness of conjugate variables are intrinsically linked and should thus be accounted for.

3.3.2 Discrete Wigner model

The *discrete* Wigner function is able to describe rotational periodicity and quantized momentum in quantum mechanics, and was first explored by J. Bizarro in 1994 [50]. The discrete Wigner function for a discrete momentum state, again labelled by m, is defined as

$$\mathcal{W}_m(\vartheta, \bar{z}) = \frac{1}{\pi}\int_{-\pi/2}^{\pi/2} \Psi^*(\vartheta - \vartheta')\Psi(\vartheta + \vartheta')e^{-2im\vartheta'}\mathrm{d}\vartheta' \tag{3.31}$$

From here on, we follow a slightly different approach compared to the continuous Wigner model by first substituting the momentum eigenstate expansion for $\Psi(\vartheta \pm \vartheta')$ of Eq. (3.12):

$$\begin{aligned}\mathcal{W}_m(\vartheta, \bar{z}) &= \frac{1}{2\pi^2}\sum_{m',m''} c^*_{m'}c_{m''}e^{-i(m'-m'')\vartheta}\int_{-\pi/2}^{\pi/2} e^{-i(2m-m'-m'')\vartheta'}\mathrm{d}\vartheta' \\ &= \frac{1}{2\pi}\sum_{m',m''} c^*_{m'}c_{m''}e^{-i(m'-m'')\vartheta}\mathrm{sinc}\Big[\Big(m - \frac{m'+m''}{2}\Big)\pi\Big].\end{aligned} \tag{3.32}$$

Since the Wigner function and both Fourier expansions are indexed by the number of momentum states, we are left with three indices (m, m', m'') that run from $(-\infty, \infty)$. The following index transformation can be made: $m' \to m + m' + \mu$ and $m'' \to m' - m$, where m'' is replaced by $\mu = 0, 1$ to maintain both integer and half-integer contributions of the sinc function. This convenient transformation allows to simplify the expression further by writing out the sum over μ. The first contribution $\mu = 0$ always evaluates the sinc function at 0 where we know that $\mathrm{sinc}(0) \to 1$, and the second contribution ($\mu = 1$) is ± 1 dependent on the exact half-integer:

$$\mathcal{W}_m(\vartheta, \bar{z}) = \frac{1}{2\pi}\sum_{m'}\left(c^*_{m+m'}c_{m-m'}e^{-2im'\vartheta} + c^*_{m+m'+1}c_{m-m'}e^{-i(2m'+1)\vartheta}\frac{(-1)^{m-m'-1}}{(m-m'-\frac{1}{2})\pi}\right) \tag{3.33}$$

This can written in slightly more compact form as

$$\mathcal{W}_m(\vartheta, \bar{z}) = w_m(\vartheta, \bar{z}) + \sum_{m'=-\infty}^{\infty}\frac{(-1)^{m-m'-1}}{(m-m'-\frac{1}{2})\pi}w_{m+\frac{1}{2}}(\vartheta, \bar{z}) \tag{3.34}$$

where for $\mu = 0, 1$ holds that

$$w_{m+\mu/2} = \frac{1}{2\pi}\sum_{m'} c^*_{m+m'+\mu}c_{m-m'}e^{-i(2m'+\mu)\vartheta}. \tag{3.35}$$

To determine the full Wigner distribution function $\mathcal{W}_m(\vartheta, \bar{z})$ *both* the integer and half-integer functions w_n and $w_{n+1/2}$ are needed. The same holds for the subsequent probability distributions for m and ϑ:

$$|c_m(\bar{z})|^2 = \int_{-\pi}^{\pi} w_m(\vartheta, \bar{z})\mathrm{d}\vartheta \tag{3.36a}$$

$$|\Psi(\vartheta,\bar{z})|^2 = \sum_m w_m(\vartheta,\bar{z}) + w_{m+1/2}(\vartheta,\bar{z}). \tag{3.36b}$$

These marginal projections are found using the Wigner function's projection property [49]. For the continuous case, we could directly find a closed evolution equation for $\mathcal{W}$. It is, however, not possible to do the same for $\mathcal{W}_m$. For this reason, we first expressed $\mathcal{W}_m$ is terms of $w_{m+\mu/2}$ where we *can* find evolution equations for, and reconstruct the full Wigner function $\mathcal{W}_m(\vartheta,\bar{z})$ after. Again for a more extensive derivation we refer to Ref. [50]. Deriving Eq. (3.35) with respect to $\bar{z}$, where we use the shorthand notation $s = m + \mu/2$, yields

$$\frac{\partial w_s(\vartheta,\bar{z})}{\partial \bar{z}} = -\frac{s}{\bar{\rho}}\frac{\partial w_s(\vartheta,\bar{z})}{\partial \vartheta} + \bar{\rho}\Big(Ae^{i\vartheta} + A^* e^{-i\vartheta}\Big)\Big\{w_{s+\frac{1}{2}}(\vartheta,\bar{z}) - w_{s-\frac{1}{2}}(\vartheta,\bar{z})\Big\}. \tag{3.37}$$

This equation is again coupled to the evolution of the radiation field as

$$\frac{\mathrm{d}A}{\mathrm{d}\bar{z}} = \sum_{m=-\infty}^{\infty}\int_{-\pi}^{\pi} w_{m+\frac{1}{2}}(\vartheta,\bar{z})e^{-i\vartheta}\mathrm{d}\vartheta + i\delta A \tag{3.38}$$

To ease numerical simulation of Eq. (3.37) and because w_s is periodic in ϑ, we can introduce an additional Fourier expansion of

$$w_s(\vartheta,\bar{z}) = \frac{1}{2\pi}\sum_{n=-\infty}^{\infty} w_s^n(\bar{z})e^{in\vartheta}. \tag{3.39}$$

Substitution in Eqs. (3.37) and (3.38) yields the final working equations of the discrete Wigner model.

$$\frac{\mathrm{d}w_s^n}{\mathrm{d}\bar{z}} + in\frac{s}{\bar{\rho}}w_s^n = \bar{\rho}\left\{A\Big(w_{s+\frac{1}{2}}^{n-1} - w_{s-\frac{1}{2}}^{n-1}\Big) + A^*\Big(w_{s+\frac{1}{2}}^{n+1} - w_{s-\frac{1}{2}}^{n+1}\Big)\right\} \tag{3.40a}$$

$$\frac{\mathrm{d}A}{\mathrm{d}\bar{z}} = \sum_{m=-\infty}^{\infty} w_{m+\frac{1}{2}}^1 + i\delta A. \tag{3.40b}$$

With this, we have arrived at a consistent set of equations that describe QFEL interaction using a discrete Wigner distribution function. First off, it is conveniently dependent on $\bar{\rho}$ whilst capturing both the discreteness and periodicity of conjugate variables intrinsic to the quantum regime ($\bar{\rho} < 1$) as well as having an explicit continuous, classical Vlasov limit ($\bar{\rho} \gg 1$). Moreover, it uniquely re-expresses their quantum dynamics to classical language which is extremely useful to investigate the intermediate/quasi-classical FEL regime, and the transition into the quantum regime.

3.3.3 Quasi-phase space dynamics

Since the consistency between Eqs. (3.40a)-(3.40b) and the momentum state model from Eqs. (3.13)-(3.15) has been demonstrated before [27, 29], we turn directly to numerical solutions of the discrete Wigner distribution function as depicted in Fig. 3.9. The Wigner function merges its separate marginal projections, which are also obtained by the wave-function model, into a single quasi-probability distribution, allowing for a more qualitative analysis of the dynamical transition into the quantum regime. Fig. 3.9(a) corresponds to the quasi-classical regime ($\bar{\rho} = 5$). The phase-space is very similar to the classical model in Fig. 2.2(a), apart from negative regions in the quasi-distribution which indicate non-classical behaviour [51]. From $|\Psi(\vartheta,\bar{z})|^2$, classical micro-bunching is recognized as the strongly peaked probability distribution around the radiation wavelength. As we move to lower $\bar{\rho}$ in Fig. 3.9(b), the classical structure is still visible although the number of involved momentum states is significantly lower compared to (a). The probability distribution around the micro-bunch positions is also less sharp and the negative regions in the distribution are more pronounced. In Fig. 3.9(c), the value for $\bar{\rho}$ is sufficiently low to reduce the number of involved momentum states to only 4, and the resulting phase space almost fully loses

the swirling, (quasi-)classical structure. Finally, for $\bar{\rho} = 0.2$ in Fig. 3.9(d), the dynamics can be fully described by c_0 and c_{-1} as an effective two-level quantum system apart from some non-zero values in the surrounding phase-space regions. These contributions do not add up to something significant in the marginal projections on m and ϑ. In this regime, the phase-space representation also makes more clear that bunching (phase correlation) is significantly lower compared to $\bar{\rho} = 5$, which might explain the lower amplitudes of the gain curve for lower values of $\bar{\rho}$ (see Fig. 3.2).

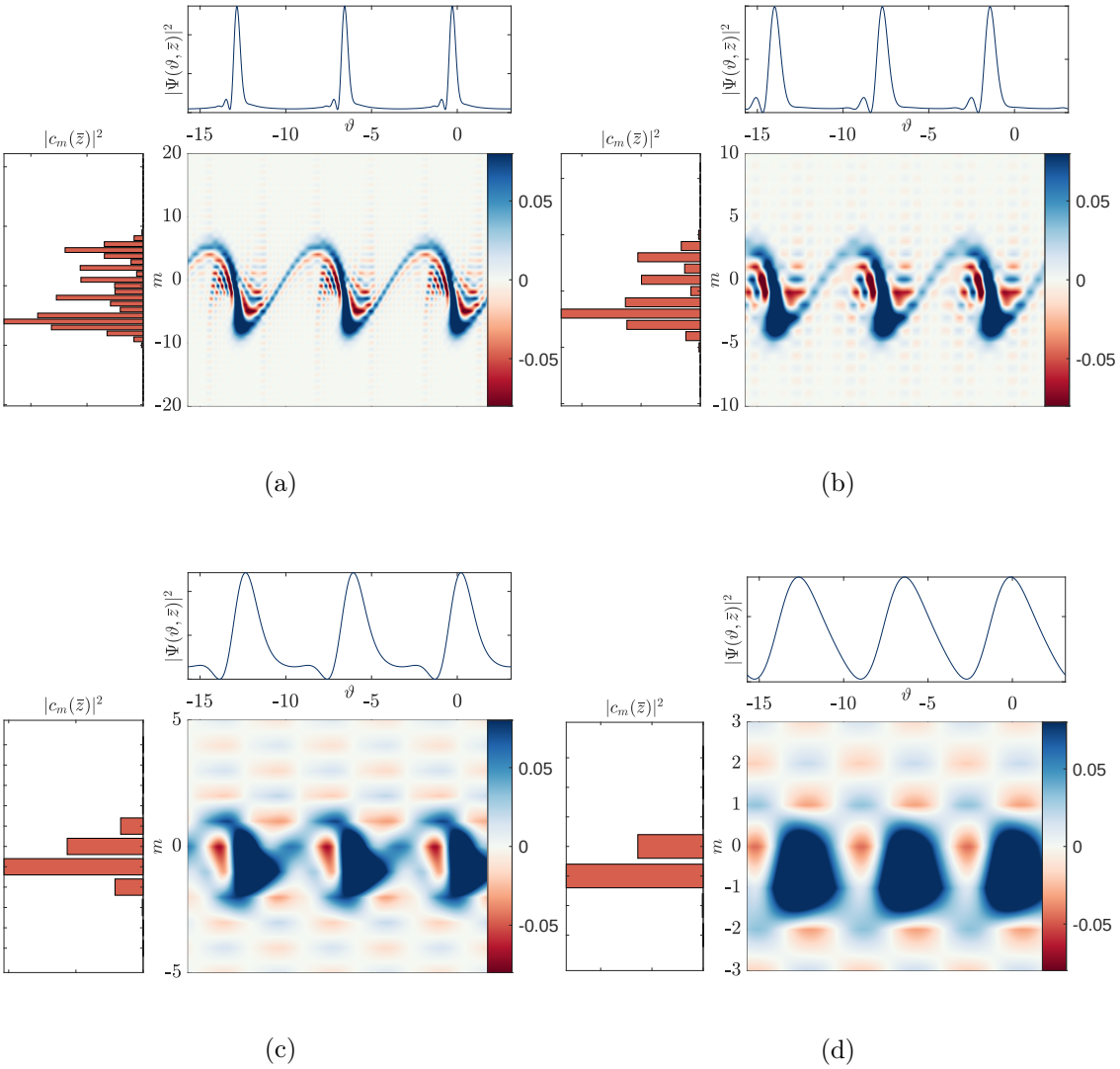

Figure 3.9: Wigner function $\mathcal{W}_m(\vartheta, \bar{z})$ with marginal projections $|c_m(\bar{z})|^2$ and $|\Psi(\vartheta, \bar{z})|^2$. Results are shown for $\bar{\rho} = 5$ (a), $\bar{\rho} = 2$ (b), $\bar{\rho} = 0.7$ (c) and $\bar{\rho} = 0.2$ (d). All positions are chosen at the point of saturation where the first radiation peak and maximum micro-bunching first occur.

3.4 Decoherence and non-ideal effects

QFEL operation heavily relies on coherent transitions between adjacent momentum states. As a result, the question arises which additional, non-ideal effects might impair this behavior and could cause decoherence. In this section, we revisit several assumptions intrinsic to the current model. Specifically, the effect of uncorrelated energy spread and spontaneous emission on the coherent

QFEL dynamics is considered. In addition, we argue that space-charge effects should be added to current models. All have a detrimental effect on the photon yield and saturation length of the steady-state and time-dependent evolution.

3.4.1 Inhomogeneous energy spread

There are two important energy scales in FELs. First, the inhomogeneous energy spread $\delta\gamma$ of the electron beam prior to interaction, as shown in Fig 3.10(a). Due to $\delta\gamma$ each electron couples slightly differently with the ponderomotive wave. Second, there is an energy modulation induced by the momentum exchange with the radiation field, as depicted in Fig. 3.10(b). In this subsection, we consider the first. So far, the electron beam has been considered mono-energetic (cold-beam approximation), at a detuning $\delta = (\gamma_0 - \gamma_r)/\rho\gamma_r$ where each electron has initial energy $\gamma(\bar{z} = 0) = \gamma_0$ at the start of the interaction. In reality, however, the incoming electron beam will always have a finite energy spread $\delta\gamma$ due to various kinds of inhomogeneous broadening mechanisms such that individual electrons will experience slightly different Doppler shifts, resulting in a broadening of the radiation bandwidth [52].

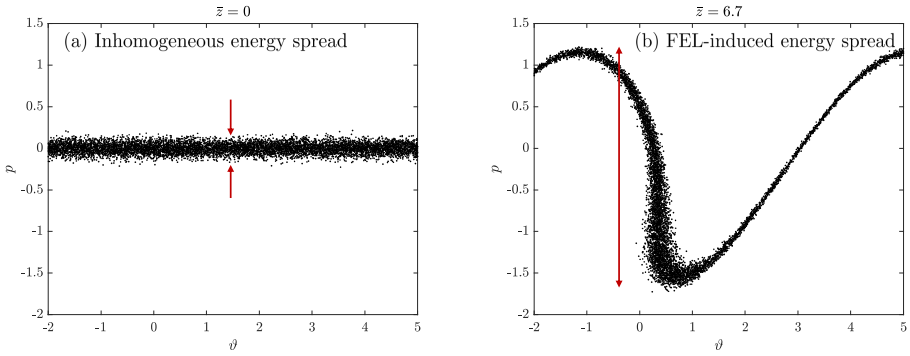

Figure 3.10: Two classical interpretations of energy spread.

Classically, energy spread can be easily implemented in the model by initializing a momentum distribution around the resonant energy for the point-charge distribution. For a QFEL, however, a broader occupation distribution over initial momentum states is not the same as energy spread, since the discreteness only emerges due to the coupling with the radiation field. (For a big part, the high-energy photons make that the quantum discreteness can even become significant ($\bar{\rho} < 1$) on the scale of FEL interaction.) As we consider the *initial* energy spread, however, coupling to the radiation field has yet to take place such that the electron momentum need not be limited to the discrete step size of the radiation and its effect cannot be captured by the momentum state description.

To take this effect into account, we assume an arbitrary distribution function $f_0(\delta)$ for the detuning $\delta = \gamma_0 - \gamma_r/(\rho\gamma_r)$. For ease of calculation, a slightly modified Fourier expansion of the wave function is adopted that includes the detuning

$$\Psi(\vartheta, \bar{z}) = \sum_{m=-\infty}^{\infty} c_m(\bar{z}, \delta) e^{in(\vartheta + \delta\bar{z})}. \tag{3.41}$$

Following identical derivation steps for the discrete Wigner model (Section 3.3) with this modified expansion, in combination with a generalized source term that include all detunings weighted by $f_0(\delta)$ for the radiation field yields

$$\frac{\partial \bar{A}}{\partial \bar{z}} = b'(\bar{z}) = \sum_{m=-\infty}^{\infty} \int_{-\infty}^{\infty} f_0(\delta) w^1_{m+\frac{1}{2}} \, \mathrm{d}\delta, \tag{3.42}$$

Here, $A = \bar{A}e^{i\delta\bar{z}}$ and the right-hand side is a quantum expression for the bunching factor $b'(\bar{z})$ weighted by the distribution. The electron equation for w_s^n remains unaltered from Eq. (3.40a). We study the effect on the radiation evolution for two different initial energy distribution $f_0(\delta)$ with an rms width of $\sigma_\delta = 0.5$ and $\sigma_\delta = 2.8$. Both are plotted together with the QFEL gain bandwidth in Fig. 3.11. Since the gain bandwidth decreases both in width and size for smaller $\bar{\rho}$ (see again Fig. 3.2), the initial energy distribution $f_0(\delta)$ could contain values which lie outside the QFEL bandwidth. For the complete wave function to take part in the interaction, it should hold that $4\sqrt{\bar{\rho}} < \sigma_\delta$, for instance $\bar{\rho} = 0.2$ yields a constraint that $\sigma_\delta \lesssim 1.8$.

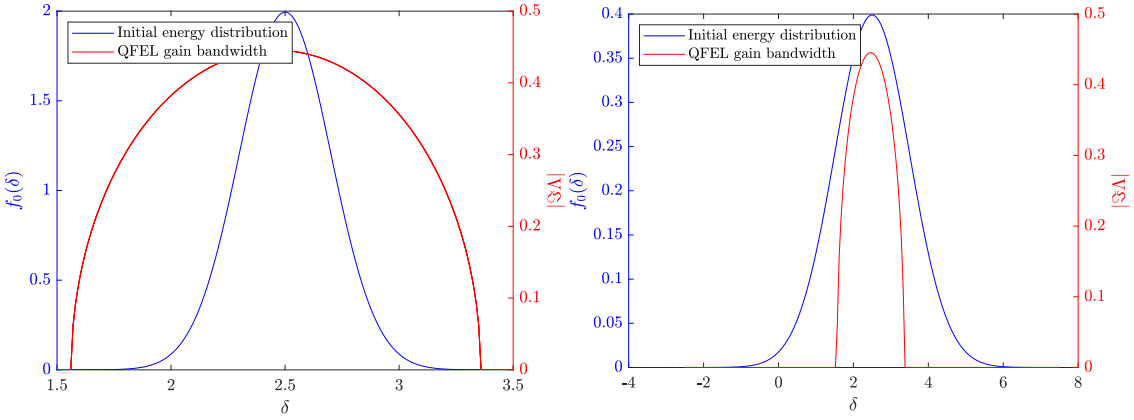

(a) (b)

Figure 3.11: Initial energy distribution $f(\delta)$ for $\sigma_\delta = 0.5$ (a) and $\sigma_\delta = 2.8$, and QFEL gain bandwidth for $\bar{\rho} = 0.2$ from the linear analysis (Eq. (3.18).

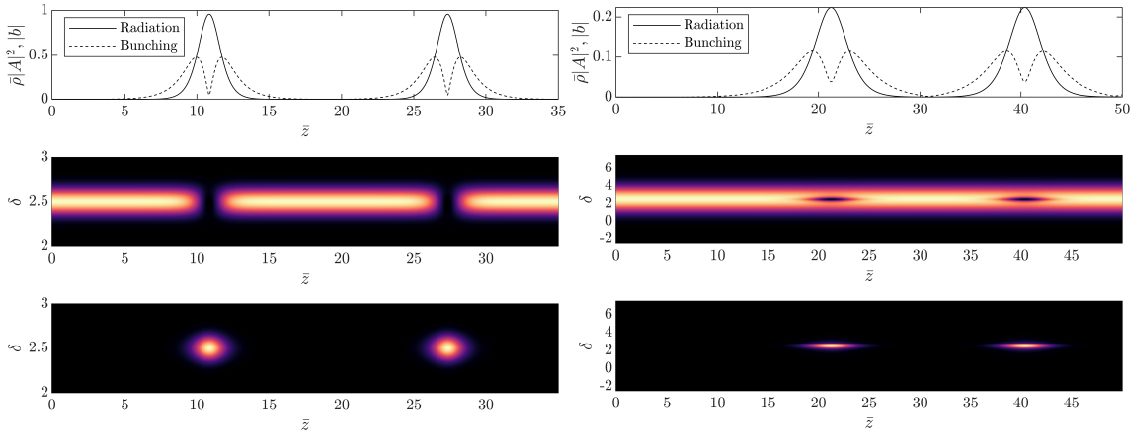

(a) (b)

Figure 3.12: Normalized radiation intensity and bunching (top), occupation probabilities $|c_0(\delta)|^2$ (center) and $|c_{-1}(\delta)|^2$ (bottom) against $\bar{z}$ for $\bar{\rho} = 0.2$.

In Fig. 3.11(a), we see that a Gaussian distribution around δ (in blue) is chosen well within the bounds of the QFEL gain bandwidth (red), such that $\sigma_\delta < 1.8$. The corresponding intensity and occupation probabilities in Fig. 3.12(a) show that the transition from c_0 to c_{-1} is fully made for all detunings. Conversely, as $f_0(\delta)$ is not contained within the gain region as depicted Fig.

3.11(b), only part of the electrons have the appropriate detuning to undergo QFEL interaction and make the transition to c_{-1}. In addition, this goes at the cost of the radiation intensity $|A_{sat}|^2$, the saturation length $\bar{z}_{sat}$ and the duration of a single pulse, as is seen in Fig. 3.13 where the radiation intensity is again plotted against $\bar{z}$ for different three rms widths of $f_0(\delta)$.

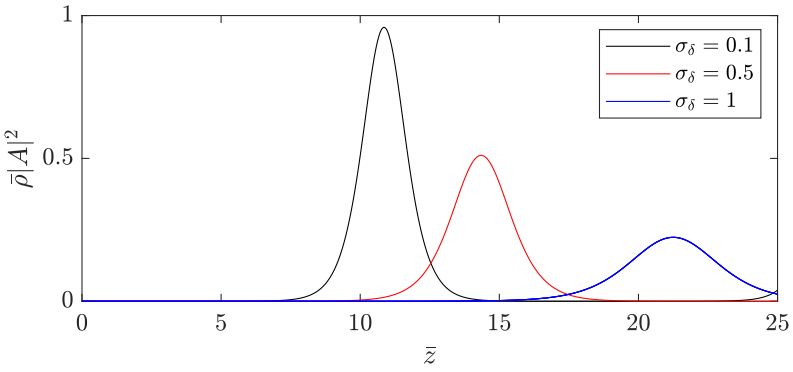

Figure 3.13: Normalized radiation intensity for three energy spreads.

3.4.2 Spontaneous emission

In QFEL operation, spontaneous emission refers to the incoherent undulator radiation emitted by electrons. However, the current model is based on electron dynamics being coupled only to the coherent radiation field, under the assumption that the coherent amplification quickly outgrows the initial incoherent contribution from spontaneous emission. Though, QFEL operation heavily relies on the coherence between adjacent momentum states $b = \sum c_m c^*_{m-1}$ as opposed to classical FELs. A significant spontaneous emission rate introduces additional transitions from c_0 and c_{-1} to lower momentum states, which causes decay of bunching and could impair the coherence. This effectively induces an energy spread to the electron distribution. This decoherence effect can be included by first considering a rate equation for the electron momentum [53, 30]. The probability of an electron having momentum p will increase by spontaneous emission events from electrons with momentum $p+\hbar k$ and decrease for electrons with momentum p. These photons are generally emitted under a certain random angle φ with respect to the propagation axis z, resulting in a distribution $G(\omega)$ for the frequency and associated photon momenta. Using this fact, we construct a simple rate equation for a momentum distribution function, in our case the Wigner function $\mathcal{W}$, of the form

$$\frac{\partial \mathcal{W}(z,p)}{\partial z} = R \int G(\omega) \mathcal{W}\Big(z, p + \hbar\frac{\omega}{c}\Big) \mathrm{d}\omega - R\mathcal{W}(z,p), \tag{3.43}$$

where $R = \pi\alpha a_0^2/(3\lambda_L)$ is the spontaneous emission rate per unit undulator length with fine-structure constant $\alpha \approx 1/137$. It has been shown, however, that broadband spontaneous emission does not significantly affect the competition between coherent and incoherent emission compared to monochromatic spontaneous emission [53], hence we will assume the latter *i.e.* $G(\omega) = \delta(\omega' - \omega)$. As the momentum distribution in our current model is captured by components w_s^n of the discrete Wigner distribution, where the probability for momentum $p = m\hbar k$ is given by Eq. (3.36a). The evolution equation for w_s^n can thus be modified to include this spontaneous emission rate as follows:

$$\frac{\mathrm{d}w_s^n}{\mathrm{d}\bar{z}} + in\frac{s}{\bar{\rho}} w_s^n = \bar{\rho}\Big\{ A\Big(w_{s+\frac{1}{2}}^{n-1} - w_{s-\frac{1}{2}}^{n-1}\Big) + A^*\Big(w_{s+\frac{1}{2}}^{n+1} - w_{s-\frac{1}{2}}^{n+1}\Big)\Big\} + \underbrace{\frac{\beta}{\bar{\rho}}\Big\{w_{s+1}^n - w_s^n\Big\}}_{\text{Spont. emission rate}}, \tag{3.44}$$

where $\beta = \alpha a_0^2 mc\gamma/(6\hbar k)$ is the spontaneous emission rate in universal scaling. In Fig. 3.14(a), the intensity, bunching and occupation probabilities for $m = 0, -1, -2$ are plotted against $\bar{z}$ for

$\bar{\rho} = 0.2$ and $\beta = 0.03$. This shows that in the quantum regime, spontaneous emission causes an additional damping of the intensity and increased saturation length as occupation of the c_{-2} state slowly starts to grow. The Wigner distribution along with its marginal projections on m and ϑ for $\bar{\rho} = 5$ and $\beta = 3$ in Fig. 3.14(b) clearly depicts two effects of spontaneous emission. First off, the negative regions of the phase-space distribution which indicate quantum behaviour, have almost fully disappeared. This is due to the energy spreading effect of spontaneous emission which increases the blue continuous (classical-like) line's thickness, obfuscating the interference regions. Also, we can observe that the induced energy spread smears out the spatial distribution function $|\Psi(\vartheta, \bar{z})|$ at the maximum bunching position. The phase-space distribution of the micro-bunches appears less sharp en less jagged compared to Fig. 3.9(a). Also notice the two orders of magnitude difference in β between the deep quantum regime ($\beta = 0.03$ in Fig. 3.14(a)) and the quasi-classical regime ($\beta = 3$ in Fig. 3.14(b)), which implies that spontaneous emission is significantly more restrictive for $\bar{\rho} < 1$.

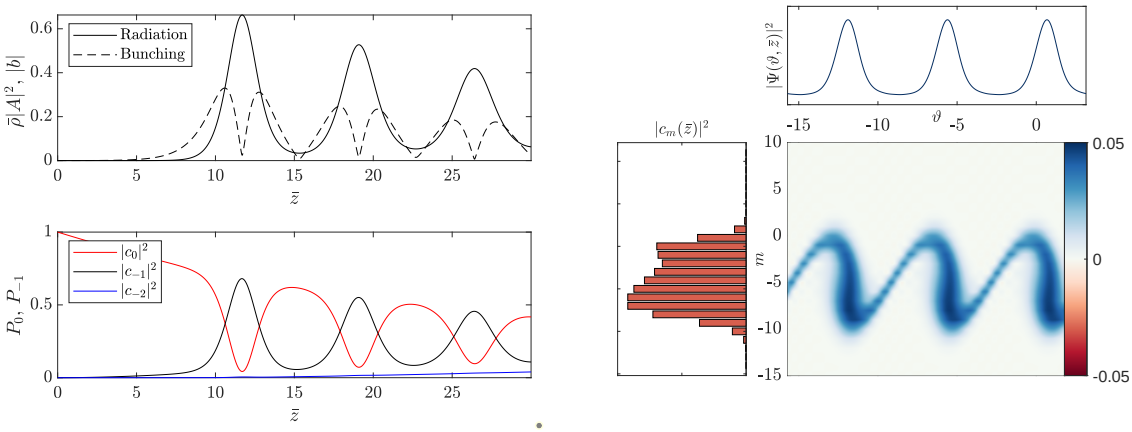

(a) (b)

Figure 3.14: (a) Normalized radiation intensity, bunching and occupation probabilities against $\bar{z}$ for $\bar{\rho} = 0.2, \beta = 0.03$. (b) Wigner distribution $\mathcal{W}_m$ for $\bar{\rho} = 5$ and $\beta = 3$.

3.4.3 Opposing constraints of spontaneous emission and space-charge

Contrary to spontaneous emission, space-charge has not been included in QFEL models leaving its effect largely unknown. To demonstrate why space-charge is important to include in a QFEL model, we review the opposing experimental constraints put on by spontaneous emission and space-charge [7]. Both effects can be associated with length scales which, in turn, can be related to the required interaction length expressed in the number of gain lengths $L_{\text{int}} = NL_g$, to derive explicit constraints for the laser undulator parameter a_0. For space-charge, the relevant length scale comes from the inverse plasma wavenumber $k_p^{-1} = c\gamma^3/\omega_p$. Using this, we pose a constraint based on the fact that micro-bunching should occur over shorter distance than space-charge effects become significant *i.e.* $NL_g < k_p^{-1}$. We can rewrite this inequality to

$$a_0 \geq a_{0,\text{min}} = N\sqrt{\frac{8\lambda_c}{\gamma\lambda_R}(1+\bar{\rho})}, \tag{3.45}$$

where we used the fact that $L_g \propto \rho^{-1}(a_0)$ and the definition of ρ from Eq. (2.24). We have also seen in the previous section that spontaneous emission leads to electron decay outside the allowed QFEL bandwidth inhibiting its performance. Alternatively, we can state that all QFEL dynamics

should take place within the lifetime of the initial electron momentum state such that a constraint can be formulated using the decay rate $R^{-1} = 2\pi\alpha a_0^2/(3\lambda_L)$. As the lifetime of an excited state should be greater than the typical interaction time such that a *coherent* interaction can actually take place, we pose the constraint that the interaction length L_{int} should be greater than (twice) the inverse decay length, or $RNL_g \leq \frac{1}{2}$. Again, we can derive a constraint for a_0 on the basis of this

$$a_0 \leq a_{0,\max} = \sqrt{\frac{3\lambda_c}{\alpha\gamma\lambda_R N}\sqrt{\frac{\bar{\rho}^3}{1+\bar{\rho}}}}. \tag{3.46}$$

Evaluating both constraint relations as a function of N in Fig. 3.15 shows that a regime in which both decoherence effects become negligible only occurs well before saturation around $N \approx 1.5 - 2$. As a consequence, QFELs cannot be operated in a space-charge-free regime while simultaneously neglecting spontaneous emission, or vice versa. Therefore, for the general completeness of the QFEL model, it becomes crucial to account for space-charge.

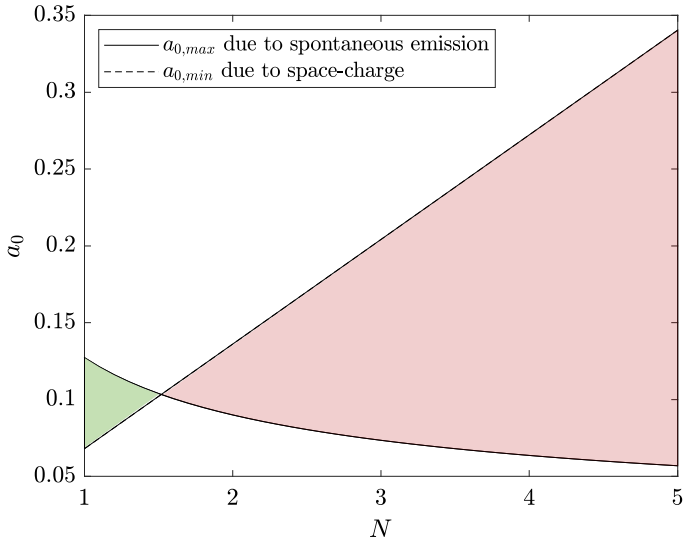

Figure 3.15: Laser undulator parameter a_0 against N. Green shaded area denotes region where $a_{0,\max} > a_{0,\min}$, in the red shaded area holds that $a_{0,\min} > a_{0,\max}$, such that both constraints cannot be met simultaneously.

4 Results of a first Raman QFEL model

This chapter focuses on the inclusion of longitudinal space-charge effects on the micro-bunch scale in a discrete Wigner model. The relevance of including space-charge in a QFEL model has been stressed on multiple occasions in literature [7, 54, 55]. In the previous chapter, it was hypothesized that space-charge could act as a decoherence mechanism with opposing experimental constraints to spontaneous emission. In this chapter, the classical space-charge potential is formally quantized after which we investigate the linear stability conditions in the momentum state model. We subsequently add the space-charge potential to a discrete Wigner model which we use to study QFEL dynamics.

4.1 Implementation of space-charge effects

At present, most X-ray FELs operate in the Compton regime where the modulation process is negligibly influenced by the internal Coulomb interaction, *i.e.* space-charge forces, between the electrons. However, at high electron densities or, such as in QFELs, at low electron beam energy, space-charge can significantly affect bunching dynamics. In this so-called Raman regime, the characteristic length scale of electron plasma behavior in terms of the (inverse) plasma wave number k_p^{-1} and the FEL gain length L_g become comparable in size. Raman FELs show even stronger collective electron behavior having direct consequences for their operating regime and overall performance. In a one-dimensional model, these effects can be largely understood in terms of *microscopic* space-charge which directly acts against the density modulations that constitute micro-bunching. Especially in micro-bunch configuration, the repulsive Coulomb forces grow stronger as electrons are more narrowly spaced. In what follows, this longitudinal microscopic space-charge field is derived and implemented in the QFEL model.

We start by evaluating the electrostatic field $E_{\mathrm{sc}} = -\nabla\Phi_{\mathrm{sc}}$ using Gauss' law for an arbitrary charge distribution $\varrho(\mathbf{x}, t)$ given by the electron bunch

$$\Big(\boldsymbol{\nabla}_{\perp}^{\mathbf{2}} + \frac{\partial^2}{\partial z^2}\Big)\Phi_{\mathrm{sc}} = -\frac{e}{\epsilon_0 mc}\varrho(\mathbf{x}, t) = \frac{e^2}{\epsilon_0 mc}\sum_{j=1}^{N}\delta^{(3)}\Big(\mathbf{x} - \mathbf{x}_j(t)\Big). \tag{4.1}$$

The one-dimensional approximation simplifies this equation to

$$\frac{\partial E_{\mathrm{sc}}}{\partial \bar{z}} = \frac{e^2}{m\epsilon_0 c^2}\frac{n_e(\vartheta)}{N_e}\sum_j \delta(\vartheta - \vartheta_j). \tag{4.2}$$

where we use the particle density as function of ϑ: $n(\vartheta) = (2\pi n_e/N)\sum_j \delta(\vartheta - \vartheta_j)$ with n_e the local density. As micro-bunches start to form on the scale of the wavelength $2\pi/(k_R + k_L)$ or the ponderomotive phase $\vartheta = (k_R + k_L)z - (k_R - k_L)ct$, the associated space-charge field generated

by the high-density regions is periodic in ϑ as well. The electron density $n(\vartheta)$ can be Fourier expanded in ϑ as follows

$$n(\vartheta) = n_e \sum_n \langle e^{-in\vartheta}\rangle e^{in\vartheta} + \langle e^{-in\vartheta}\rangle^* e^{-in\vartheta}. \tag{4.3}$$

Note that the summing over delta functions has allowed for a similar averaging procedure as before, see for instance Eq. (2.18). Using this, we can solve Eq. (4.2) to obtain an expression for the space-charge field.

$$E_{\mathrm{sc}}(\vartheta) = k_R\Big(\frac{\omega_p}{\omega_R}\Big)^2 \sum_{n=0}^{\infty} \frac{\langle e^{-in\vartheta}\rangle e^{in\vartheta} - \langle e^{-in\vartheta}\rangle^* e^{-in\vartheta}}{in}. \tag{4.4}$$

As we neglect macroscopic space-charge effects, the zeroth ($n = 0$) harmonic of the Fourier expansion is neglected. In fact, the only term of interest, for now, is the microscopic space-charge field periodic with the first harmonic ($n = 1$) of the radiation wavelength, as we neglect higher harmonics. Interestingly, this field is proportional to the bunching factor $b = \langle e^{-i\vartheta}\rangle$. This makes sense: as the bunching factor increases, electrons collect themselves in small regions to form the micro-bunches. More closely spaced, the repulsive Coulomb forces between electrons are more pronounced and the corresponding field should grow. This result should now be fitted into the classical FEL model of Eqs. (2.25a)-(2.25c). It is easily recognized that the presence of an additional electric field will modulate the electron momenta, since $F = \mathrm{d}p/\mathrm{d}t = qE$. This way, the evolution of p_j can be written as having an additional term:

$$\frac{\mathrm{d}p_j}{\mathrm{d}\bar{z}} = -\underbrace{\Big(Ae^{i\vartheta_j} + A^* e^{-i\vartheta_j}\Big)}_{\text{Mod. by radiation field}} - \underbrace{i\sigma\Big(be^{i\vartheta_j} - b^* e^{-i\vartheta_j}\Big)}_{\text{Mod. by space-charge field}} = -\Big[(A+i\sigma b)e^{i\vartheta_j} + (A - i\sigma b^*)e^{-i\vartheta_j}\Big]. \tag{4.5}$$

Equation (4.4) has undergone universal scaling, where we introduced the space-charge parameter σ as

$$\sigma = 4\rho\frac{1+a_0^2}{a_0^2} = \frac{L_g}{\rho\gamma}k_R\Big(\frac{\omega_p}{\omega_R}\Big)^2. \tag{4.6}$$

The space-charge parameter denotes the amplitude and thereby the strength of the space-charge field, and is dependent on both the electron energy and density. Here we also observe that σ increases for high densities and low γ. So far, this derivation is fully classical but, of course, we like to extend this to the quantum regime. Similarly, by recognizing the equivalence between Eq. (2.25a) and the modified equation for p_j, we can write the associated Hamiltonian as

$$\mathcal{H} = \sum_j \mathcal{H}_j = -\frac{1}{2\bar{\rho}}\frac{\partial^2}{\partial\vartheta^2} - i\bar{\rho}\Big[(A + i\sigma b)e^{i\vartheta_j} + (A^* - i\sigma b^*)e^{-i\vartheta_j}\Big]. \tag{4.7}$$

Again by substitution of the Hamiltonian $\mathcal{H}$ in the Schrödinger-like equation, we obtain an evolution equation for the electron wave function

$$\frac{\partial\Psi}{\partial\bar{z}} = -\frac{i}{2\bar{\rho}}\frac{\partial^2\Psi}{\partial\vartheta^2} - \bar{\rho}\Big[(A + i\sigma b)e^{i\vartheta_j} + (A^* - i\sigma b^*)e^{-i\vartheta_j}\Big]\Psi, \tag{4.8}$$

where the bunching factor is again given by the expectation value expression $b = \int \Psi^*\Psi e^{-i\vartheta}\mathrm{d}\vartheta$. The radiation field evolves in an identical way according to Eq. (3.14)

4.2 Detuning with quantum and space-charge corrections

Having introduced a new free parameter to the equations, it is essential to investigate the conditions under which the steady-state instability can occur. For sake of clarity, we perform the linear

stability analysis using the momentum state model. This yields an evolution equation for c_m coefficients

$$\frac{\mathrm{d}c_m}{\mathrm{d}\bar{z}} = -i\frac{m^2}{2\bar{\rho}}c_m - \bar{\rho}\Big[(A + i\sigma b)c_{m-1} + (A^* - i\sigma b^*)c_{m+1}\Big], \tag{4.9}$$

which is coupled to the radiation field that evolves according to Eq. (3.15). Assuming small variations around the stationary solution ($A \approx \Delta A$, $c_0 \approx 1 + \Delta c_0$ and $c_{m\neq 0} \approx \Delta c_m$) a single third-order is derived of the form:

$$\frac{\mathrm{d}^3 A}{\mathrm{d}\bar{z}^3} - i\delta\frac{\mathrm{d}^2 A}{\mathrm{d}\bar{z}^2} + \Big[\frac{1}{4\bar{\rho}^2} + \sigma\Big]\frac{\mathrm{d}A}{\mathrm{d}\bar{z}} - i\Big(\Big[\frac{1}{4\bar{\rho}^2} + \sigma\Big]\delta + 1\Big)A = 0. \tag{4.10}$$

Assuming a solution of the form $A \propto e^{i\Lambda\bar{z}}$ yields the following dispersion relation

$$(\Lambda - \delta)\Big(\Lambda^2 - \Big[\frac{1}{4\bar{\rho}^2} + \sigma\Big]\Big) + 1 = 0. \tag{4.11}$$

The dispersion relation admits the classical Compton limit ($\sigma = 0, \bar{\rho} \gg 1$) from Eq. (2.31), the quantum Compton limt ($\sigma = 0, \bar{\rho} < 1$) from Eq. (3.18) *and* the classical Raman limit ($\sigma \neq 0, \bar{\rho} \gg 1$) [56], all three of which are consistent with existing literature. The interesting regime for us, of course, is the quantum Raman regime ($\sigma \neq 0, \bar{\rho} < 1$). Although this result was found before using a heuristic approach [55], we here formally derived the dispersion relation including both quantum and space-charge corrections. We can show that the approximate detuning to obtain optimal gain is given by

$$\delta_{\max} \approx \sqrt{\frac{1}{4\bar{\rho}^2} + \sigma}. \tag{4.12}$$

In Fig. 4.1 we have plotted the growth rate against the detunings for 4 combinations of $\bar{\rho}$ and σ. It can be seen that both the quantum and space-charge corrections affect the gain region identically; for optimal gain with non-zero space-charge, the detuning should be increased accordingly and the optimal gain is decreased. From this, we may conclude that it has a detrimental effect on the dynamics.

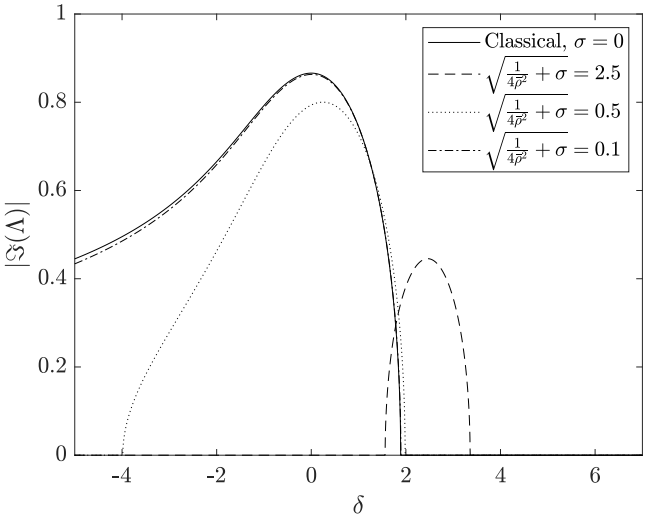

Figure 4.1: Growth rate against detuning, for different values of σ and ρ.

4.3 Wigner quasi-phase-space dynamics

Having done a formal derivation of the evolution equation for $\Psi(\vartheta, \bar{z})$ with space-charge, we can go a step further to study the effect of space-charge in steady-state simulations. Although the

momentum state model allows for easy linearization, we use the Wigner model to investigate the effects of space-charge on the phase-space dynamics. Importantly, the Wigner model allows for better bench-marking with classical simulation in the Raman limit. Subsequently, we can gradually decrease $\bar{\rho}$, which brings us into the quantum regime. Using the evolution of Ψ in Eq. (4.8), which now includes space-charge, we can follow the same steps to derive a discrete Wigner description including space-charge:

$$\frac{\mathrm{d}w_s^n}{\mathrm{d}\bar{z}} + in\frac{s}{\bar{\rho}}w_s^n = \bar{\rho}\Big\{(A+i\sigma b)\Big(w_{s+\frac{1}{2}}^{n-1} - w_{s-\frac{1}{2}}^{n-1}\Big) + (A^* - i\sigma b^*)\Big(w_{s+\frac{1}{2}}^{n+1} - w_{s-\frac{1}{2}}^{n+1}\Big)\Big\} \tag{4.13a}$$

$$\frac{\mathrm{d}A}{\mathrm{d}\bar{z}} = b + i\delta A = \sum_{m=-\infty}^{\infty} w_{m+\frac{1}{2}}^1 + i\delta A \tag{4.13b}$$

The quasi-phase-space can be reconstructed from the numerical solutions of w_s^n according to Eq. (3.34) for $\mathcal{W}_m$, as well as the marginal probability distributions for ϑ and c_m from respectively Eq. (3.36b) and Eq. (3.36a). The Wigner function $\mathcal{W}_m$ and associated marginal projections $|\Psi|^2$ and $|c_m|^2$ for increasing values of $\bar{\rho} = 0.2, 1, 5$ in the Compton ($\sigma = 0$) and Raman regime ($\sigma = 3$) are plotted in Fig. 4.2.

4.3.1 Classical limit

Figures 4.2(a)-(b) show the correspondence between the classical phase space one gets from numerically integrating Eqs. (2.25a)-(2.25c) and the Wigner function in both the Compton ($\sigma = 0$) and Raman limit ($\sigma \neq 0$) at the point of saturation. The (quasi-)phase-space in Fig. 4.2(a) is shown at the position where the bunching factor reaches its maximum value, which can be recognized as the periodic, vertical alignment in phase space. From the marginal distribution for ϑ, *i.e.* the probability $|\Psi(\vartheta, \bar{z})|^2$, bunching is observed as increased probability to find electrons at the micro-bunch positions. Although classical-like dynamics for $\mathcal{W}_m$ are clearly visible, the relatively low value of $\bar{\rho} = 5$ makes that some quantum interference effects in the negative regions of the phase-space are still visible and we recognize that the momentum state occupation, although a multiple of states is occupied, has not fully lost its discrete nature.

To attain optimal gain in Raman FELs, electrons are more strongly detuned (see Eq. (4.12)) which increases the effective energy spread of the electrons induced by the momentum exchange with the radiation field [57]. Larger bucket amplitudes, quantum mechanically, correspond to the occupation of more momentum states, which is clearly visible in Fig. 4.2(b). Here, quantum interference and momentum discreteness is again not fully lost. Micro-bunching still occurs although the probability distribution is somewhat smeared out and shows more oscillatory behaviour with respect to the Compton FEL.

4.3.2 Intermediate and quantum regime

To show the transition from the pendulum-like phase-space swirls in classical FELs to the simpler two-state transitions in the QFEL picture, we turn to the resulting phase spaces in Figs. 4.2(c)-(d). As is seen, the number of momentum states getting occupied during the interaction reduces in this intermediate regime for $\bar{\rho} = 1$ compared to $\bar{\rho} = 5$. Some of the characteristics of classical orbits are evident but the discreteness of momentum is more apparent in the resulting phase spaces. Especially Fig. 4.2(d) resembles the Raman phase-space shape from Fig. 4.2(b), though with discreteness being more visible. When entering the quantum regime in Fig. 4.2(e)-(f), the phase-space representation becomes trivial. As the momentum state occupation is reduced to only two states, we turn to the radiation field and separate momentum states in the next section, to further investigate the Raman QFEL regime.

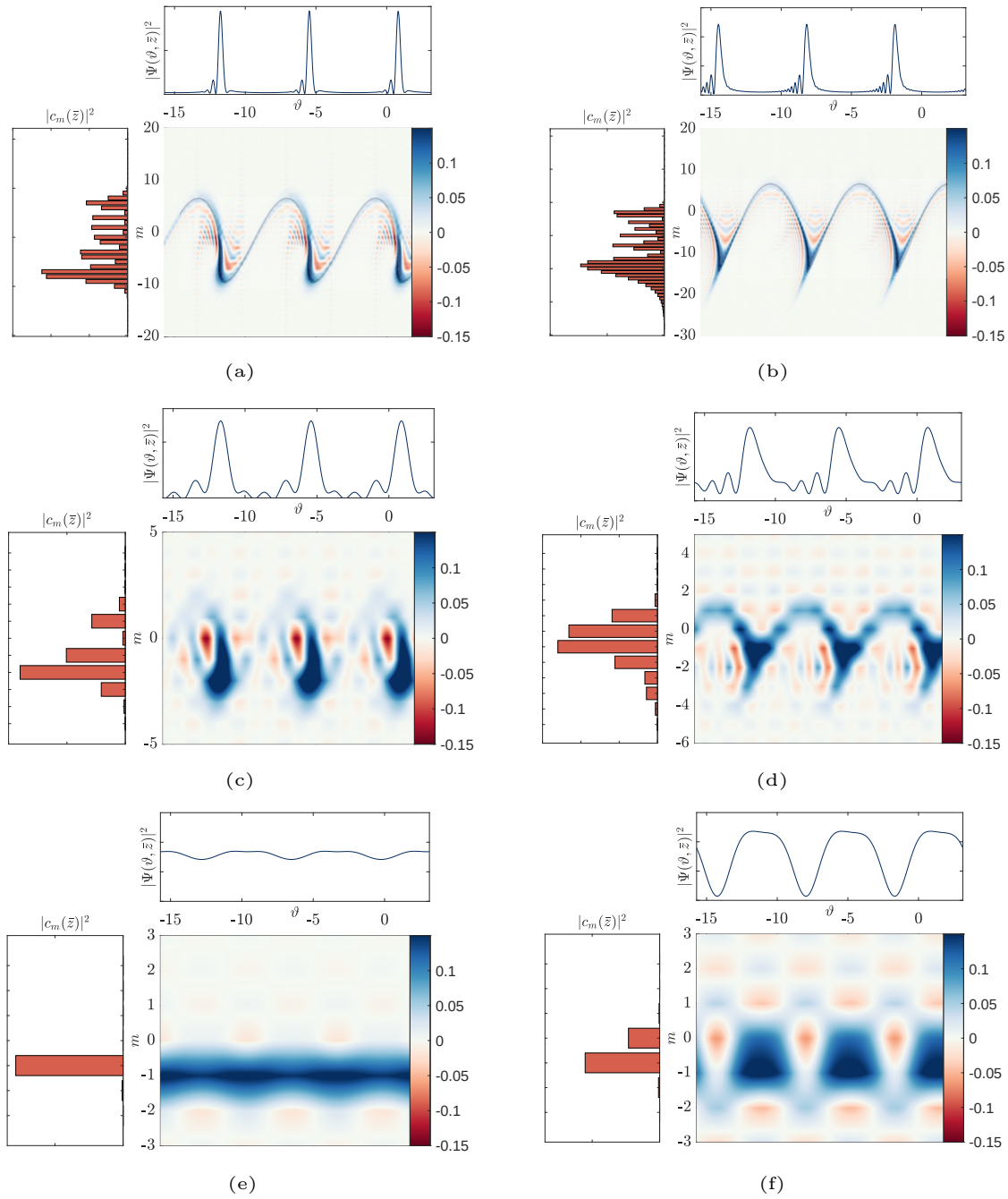

Figure 4.2: Wigner function $\mathcal{W}_m(\vartheta, \bar{z})$ with marginal projections for m (left) and ϑ (top). Results are shown for (a) $\bar{\rho} = 5, \sigma = 0$ at $\bar{z} = 11.9$, (b) $\bar{\rho} = 5, \sigma = 3$ at $\bar{z} = 18.9$ (both with classical phase-space overlap according to Eqs. (2.25a)-(2.25c)), (c) $ar\rho = 1, \sigma = 0$ at $\bar{z} = 13.5$, (d) $\bar{\rho} = 1, \sigma = 3$ at $\bar{z} = 18.5$, (e) $\rho = 0.2, \sigma = 0$ at $\bar{z} = 10.7$, (f) $\rho = 0.2, \sigma = 3$ at $\bar{z} = 11.6$. All positions are chosen at the point of saturation where the first radiation peak and maximum micro-bunching first occur.

4.4 Radiation field and momentum state dynamics

We now examine the deep quantum regime with space-charge. In Fig. 4.3(a), the evolution of the c_0 and c_{-1} states is plotted as function of $\bar{z}$ for $\sigma = 3$. Contrary to a Compton QFEL where the electron wave function completely transitions to the c_{-1} state, the electron wave function in the Raman regime does not completely de-excite. Instead, the radiation reaches saturation when the wave function is in a superposition of both states, which comes at the cost of radiation intensity. This can also be seen in Figs. 4.2(f) by the distinct occupation of the Wigner distribution at the point of saturation of the radiation. The phase-space plots also show that decoherence, *i.e.* the occupation of momentum states outside the two-state QFEL bandwidth such as with spontaneous emission, does not take place.

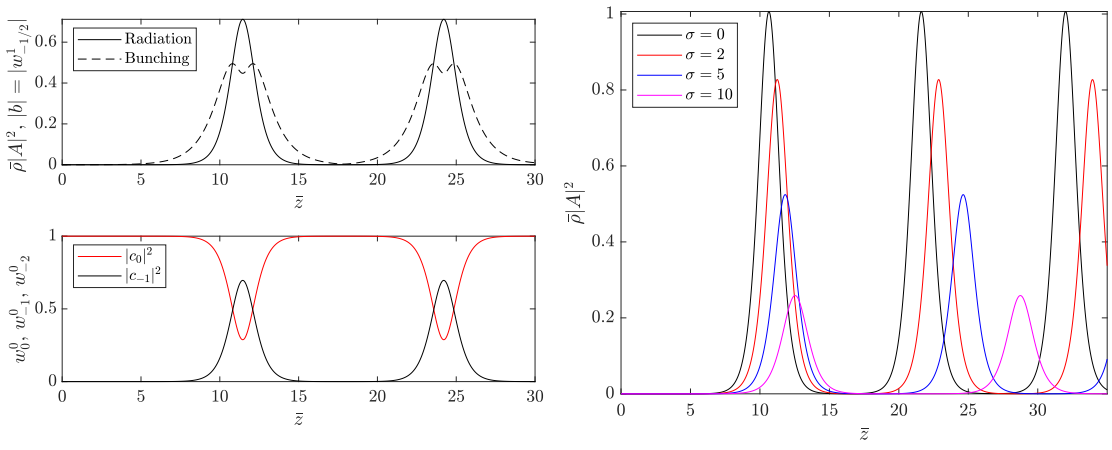

(a) (b)

Figure 4.3: (a) Normalized radiation intensity and bunching factor (top) and occupation probabilities (bottom) against $\bar{z}$ for $\sigma = 3$. (b) Normalized radiation intensity for different values of σ.

The transition is increasingly damped for higher σ, reducing the peak saturation intensity and increasing the saturation length, which is more clearly seen in Fig. 4.3(b) where the normalized intensity is set out against $\bar{z}$ for different values of σ. We can further illustrate this on the basis of a numerical example. For $\sigma = 5$ the radiation saturates about 2 gain lengths later ($\bar{z} \approx 12.5$) at only 50% intensity (so $\bar{\rho}|A|^2 \simeq 0.5$) with respect to the Compton limit. Based on this, one might be tempted to extrapolate the trend of increasing saturation lengths and decreasing radiation amplitude to conclude that eventually, for sufficiently strong space-charge effects, the occupation probability of c_0 stays fixed to 1, the transition to c_{-1} is fully withheld and therefore no radiation is produced.

To test this, we simulate QFEL dynamics for even stronger space-charge of which the results are shown in Fig. 4.4. Figure 4.4(a) shows that as the transition probability to c_{-1} tends to zero, the c_{-2} state starts contributing to the dynamics, perturbing the pure two-state dynamics and altering the periodicity of the radiation peaks. By increasing σ only slightly further as shown in Fig. 4.4(b), the c_{-2} state starts to overtake at the positions of the radiation peaks. As a result, QFEL-like dynamics in the form of a periodic sequence of radiation pulses are recovered but with prolonged saturation and a significantly longer transition period. The additional strength of space-charge has radically altered the behavior to where a specific transition from c_0 to c_{-2} is now being driven. The c_{-1} state still participates in the transition though not predominantly, and the

transition is still terminated by a complete return to the c_0 state.

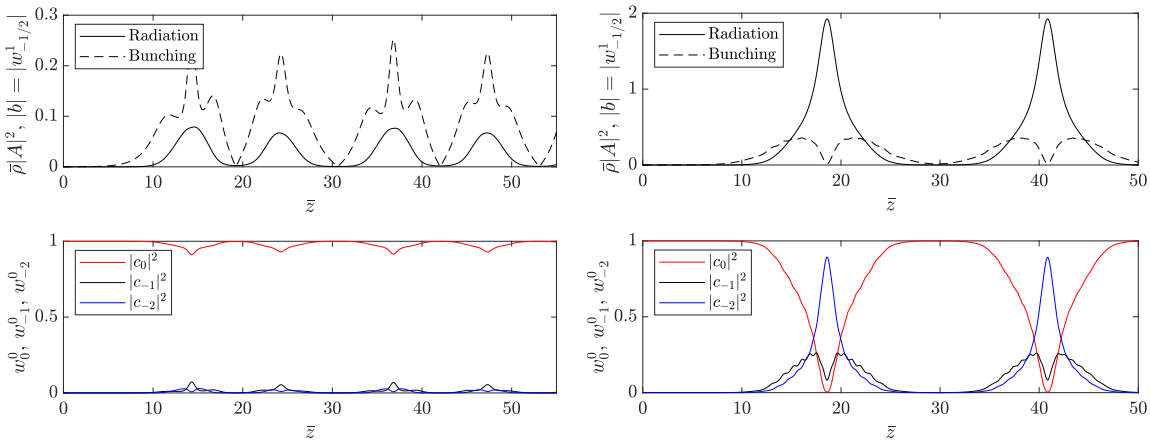

(a) (b)

Figure 4.4: Radiation intensity, bunching factor and momentum state occupations against $\bar{z}$ for $\sigma = 18.5$ (a) and $\sigma = 20$ (b)

To explain this variant behavior when operating at stronger space-charge, we first compare $\delta_{\max}$ to $\hbar k$ to evaluate a critical value regime for σ in which the added electron energy could trigger dynamics outside the two-level system between c_0 and c_{-1}. For this we evaluate the detuning normalized to a single-photon momentum in the following inequality:

$$\delta_{\max}\bar{\rho} = \frac{\gamma_0 - \gamma_r}{\rho\gamma_r}\frac{\gamma_r mc\rho}{\hbar k} = \frac{(\gamma_0 - \gamma_r)mc}{\hbar k} \geq 1. \tag{4.14}$$

Substitution of Eq. (4.12) and solving for σ yields a critical value from which the detuning necessary for optimal gain with space-charge starts to provide electrons with sufficient energy to start driving higher-harmonic transitions between momentum states that lie outside the usual QFEL two-level system. This critical value for the space-charge parameter σ is given by

$$\sigma_{\text{crit}} \geq \frac{3}{4\bar{\rho}^2}. \tag{4.15}$$

Next, we will benchmark this analytical result with numerical simulations. In Fig. 4.5, we plotted the (normalized) maximum intensity for the first radiation peak as found through numerical integration of Eqs. (4.13a)-(4.13b) against σ. The first region $0 \leq \sigma < \sigma_{\text{crit}}$ shows a steady decrease of the radiation intensity due to attenuated momentum state transitions within the two-level system, consistent with Fig. 4.3. For the region $\sigma \geq \sigma_{\text{crit}}$ however, the intensity makes an abrupt jump to a value of 2 as the c_{-2} transition and the sequential pulsing of radiation from Fig. 4.4(b) start to overtake. The critical value at which this sudden intensity jump occurs is in accordance with the analytical result from Eq. (4.15) suggesting that detuning is indeed responsible for this behaviour. The increase in intensity can be explained due to the momentum separation between c_0 and c_{-2} being equal to $2\hbar k$.

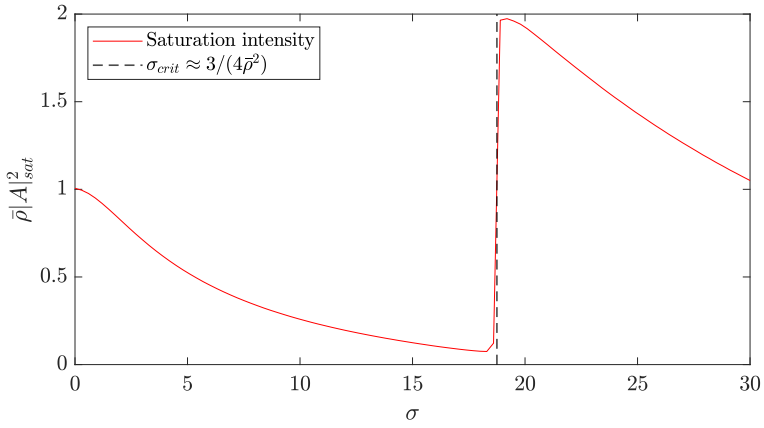

Figure 4.5: Normalized saturation intensity against space-charge parameter.

4.4.1 Limitations from higher harmonics

We immediately recognize that by introducing higher-order transitions to the dynamics in the region $\sigma \geq \sigma_{\text{crit}}$, the current implementation of space-charge effects in this model does not suffice anymore. The first-order Fourier components for bunching have so far been considered dominant with respect to higher-order Fourier components, such that the complete space-charge field from Eq. (4.4) is not taken fully into account. In the case of driving transitions dominantly with c_{-2}, it is evident that the second-order bunching factor $b_2 = \langle e^{-2i\vartheta} \rangle = \sum_m c_m c^*_{m-2}$ starts to become relevant in addition to the first-order b. Most FEL models have worked under the (valid) assumption that space-charge on the micro-bunch scale suffices to capture the dominating dynamics. Here, however, we show a case where specific values of σ result in targeting specific transitions (such as between $c_0 - c_{-2}$ for $\sigma \geq \sigma_{\text{crit}}$) for which this assumption might not be valid anymore. Further work should thus include the effects of higher-order Fourier components to the space-charge and bunching formalization, although we recognize that the experimental parameters for such high σ are currently not within realistic bounds.

4.5 In sum

For the first time, we have presented an extended Wigner QFEL model that includes longitudinal space-charge effects on the micro-bunch scale, and studied its dynamics. The explicit correspondence between the Wigner phase space in the classical limit and classical Raman FEL models as well as the dispersion relation inferred from the linear stability analysis, have shown that extending the classical space-charge potential to a QFEL model can be done consistently. Numerical simulations have shown overall decreasing quantum efficiency and saturation length increase for larger values of σ. For even stronger space-charge, we have found a critical regime of σ where the corresponding detuning necessary for optimal gain is sufficiently large to start driving transitions between momentum states outside the two-level bandwidth. Space-charge can here be viewed as a mechanism directly responsible for the loss of coherence whilst recognizing that, for this specific case, the first-order Fourier description of space-charge might fall short. The inclusion of space-charge directly makes for a more realistic, complete QFEL model, and can be used in combination with the effect of spontaneous emission from Ref. [30] for further, more extensive studies. Especially considering the opposing constraints for these two decoherence effects set out in Ref. [7], the results and theoretical model presented here are highly relevant for further discussion. Whilst recognizing that a 3D approach of space-charge, which includes transverse and macroscopic space-charge, will eventually be necessary, the 1D implementation presented here captures much of the relevant physics and provides a consistent theoretical continuation of existing QFEL models.

5 Towards a 3D QFEL model

In this chapter, we make progress towards a 3D QFEL model. We first perform simulations of a model that includes the aforementioned decoherence effects as well as 2D and 3D diffraction of radiation based on a finite electron beam waist. Based on these results, we propose a numerical approach using decomposition in transverse radiation modes. Finally, we discuss the more general structure of a 3D model which includes transverse electron dynamics and the 3D ponderomotive wave using the Wigner formalism. This type of model is, however, severely limited by its computational load required for simulation.

5.1 Simulation results with diffraction

So far, we have seen that the Wigner model can be extended to account for the competition between coherent and spontaneous emission through the β parameter (Chapter 3) as well as space-charge effects by σ (Chapter 4). The corresponding evolution equation for w_s^n is then given by

$$\frac{\mathrm{d}w_s^n}{\mathrm{d}\bar{z}} + in\frac{s}{\bar{\rho}}w_s^n = \bar{\rho}\Bigg\{(A + i\sigma b)\Big(w_{s+\frac{1}{2}}^{n-1} - w_{s-\frac{1}{2}}^{n-1}\Big) + (A^* - i\sigma b^*) \times \Big(w_{s+\frac{1}{2}}^{n+1} - w_{s-\frac{1}{2}}^{n+1}\Big)\Bigg\} + \frac{\beta}{\bar{\rho}}\Big\{w_{s+1}^n - w_s^n\Big\}. \quad (5.1)$$

The field equation was also modified to include the inhomogeneous energy spread of the incoming electrons. Now, we will additionally consider diffraction, that is the spreading of the radiation field as it passes the boundaries/edges of the electron beam. We do so by taking into account the transverse derivatives in the field equation

$$\frac{\partial A}{\partial \bar{z}} - \underbrace{ia\nabla_{\bar{\mathbf{x}}_\perp}^2 A}_{\text{Diffraction}} = \sum_{m=-\infty}^{\infty}\int_{-\infty}^{\infty} f_0(\delta)w_{m+\frac{1}{2}}^1 \mathrm{d}\delta, \quad (5.2)$$

where $a = L_g/Z_R$ is the diffraction parameter with $Z_R = 4\pi\sigma_x^2/\lambda_R$ the radiation Rayleigh length for a radius equal to the transverse rms electron beam size σ_x. The definition of a in Eq. (5.2) follows directly from the 3D Maxwell wave equation and universal scaling of $\nabla_{\mathbf{x}_\perp}^2/(2ik_R)$ from Eq. (2.19). To obtain numerical solutions to these equations, we define a 3D Cartesian grid in combination with a Runge-Kutta solver scheme (see Appendix A). In addition, to compute the transverse dependence of the radiation field efficiently, we use a Fourier-transformed radiation field $\tilde{A}(\bar{z}, \boldsymbol{\kappa}_\perp) = \int A(\bar{z}, \mathbf{x}_\perp)e^{i(\boldsymbol{\kappa}\cdot\mathbf{x})_\perp}$ such that the nabla-operator simplifies to $\nabla_{\mathbf{x}_\perp}^2\tilde{A} \to -\kappa^2\tilde{A}$. Rather than Fourier transforming Eq. (5.1) as well, we inverse Fourier transform $\tilde{A} \to A$ for each step $\Delta\bar{z}$ to consistently couple the field to the Wigner evolution.

5.1.1 2D steady-state diffraction

We first isolate the effect of radiation diffraction, for simplicity, in one transverse direction. The transverse occupation distribution of the momentum states is chosen to be Gaussian centered

around the electron propagation axis and normalized to $1-\epsilon^2$ for c_0 and ϵ^2 for c_{-1}. No seed field is included in the simulation, *i.e.* $A_0 = 0$. We consider the case with no diffraction ($a = 0$) in Fig. 5.1(a) where the normalized intensity is plotted in the $(\bar{x}, \bar{z})$-plane for $\bar{\rho} = 0.2$, the only difference with 1D being a finite electron beam waist. Each part of the beam still evolves independently from the others. The occupation probability, which is a measure of the electron density, simultaneously determines the bunching factor is lower at the edge of the electron beam, resulting in slower radiation growth. In Fig. 5.1(b), the normalized intensity is again plotted for $\bar{\rho} = 0.2$ but with diffraction $a = 0.01$. Around the saturation point, we see part of the radiation diffracts away in the regions $|\bar{x}| > 1$. As a consequence, some of the radiation escapes the interaction volume with the electron beam and thus cannot undergo further amplification leading to a lower on-axis intensity ($\bar{\rho}|A|^2 \approx 0.2$). For higher values of $\bar{z}$, the radiation better maintains its overlap with the electron beam but decreases in intensity.

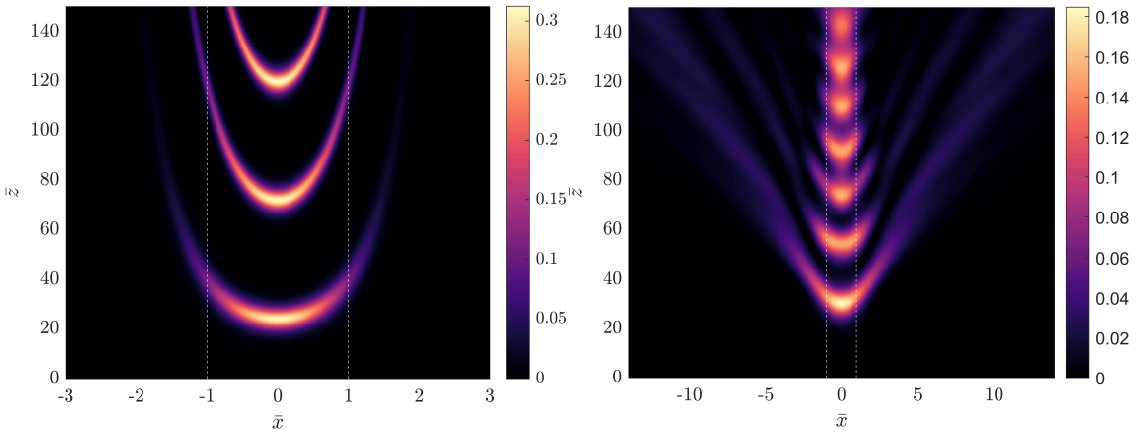

(a) No diffraction

(b) Diffraction

Figure 5.1: Normalized radiation intensity $\bar{\rho}|A|^2$ denoted by colorbar vs. $\bar{z}$ for $\bar{\rho} = 0.2$, $\delta = 5$ for (a) $a = 0$ and (b) $a = 10^{-2}$.

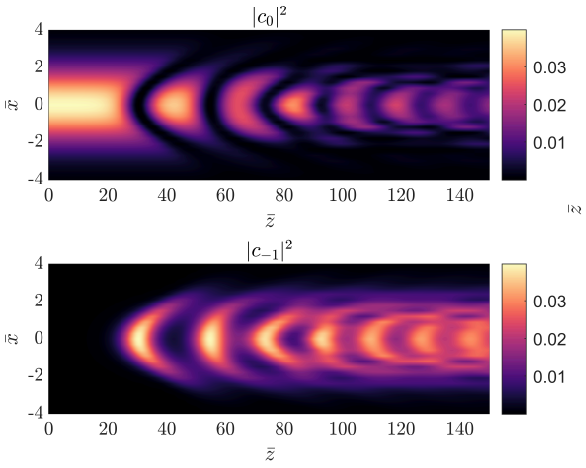

Figure 5.2: Occupation probabilities for c_0 and c_{-1}.

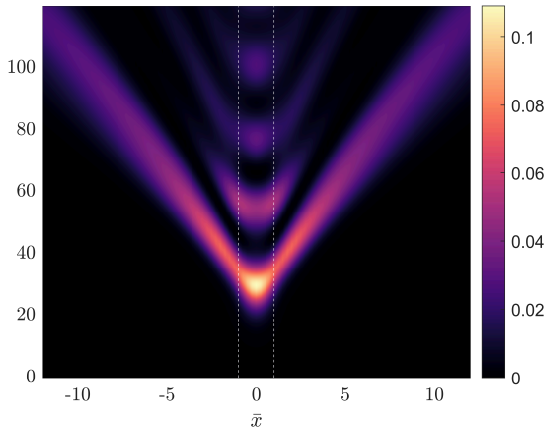

Figure 5.3: Normalized radiation intensity for $\sigma = 0.5$, $\beta = 8 \cdot 10^{-4}$.

The occupation probabilities $|c_0|^2$ and $|c_{-1}|^2$ are plotted against $\bar{x}$ and $\bar{z}$ for the the same parameters as the previous example as shown in Fig. 5.1(b) in Fig. 5.2, and show transitions between

the two states still occurring. The transverse width of the electron beam remains unchanged as the emittance is excluded from the model. We also observe that the transitions become less sharp, *i.e.* less separated along the undulator. As a result, the cyclic pulsing of the radiation intensity characteristic of the 1D QFEL model starts to become less pronounced. Lastly, we perform a 2D simulation of the intensity again for $\bar{\rho} = 0.2$ and $a = 10^{-2}$, but including non-zero space-charge $\sigma = 0.5$ and a spontaneous emission rate of $\beta = 8 \cdot 10^{-4}$ in Fig. 5.3. We observe notable damping of the radiation intensity due to increasingly attenuated transitions in accordance with the 1D result discussed in section 3.4.2. It is also interesting to observe the significantly higher intensity in the tails of the diffracted radiation pattern. This might be caused by the interplay between the bunching initialization and the proportionality of the space-charge term to b, but more extensive simulation is necessary to make any hard statements.

5.1.2 3D diffraction and transverse cross-sections

Here we will extend to 3D space and study the diffracted radiation pattern. First, we consider a plot at $\bar{y} = 0$ of the 3D normalized intensity against $\bar{x}$ and $\bar{z}$ for $\bar{\rho} = 0.2$, $a = 10^{-2}$ and $\beta = \sigma = 0$ in Fig. 5.4. By comparing Fig. 5.4 with Fig. 5.1(b), we observe a similar effect around the first saturation peak where radiation fans out away from the interaction volume. We also observe that Rabi-like oscillations damp out. This occurs on a shorter length scale compared to 2D, since radiation now diffracts away in two transverse directions instead of one. This way, radiation is more quickly lost outside the interaction volume. For the multi-dimensional simulations, we remark that the dynamics is intrinsically different due to the transverse spreading and normalization of the electron wave function. By renormalizing b, we can effectively consider the 1D model as the inner core of the 3D radiation profile such that consistency can be recovered between the models. As a consequence, the on-axis peak radiation in Fig. 5.4 is normalized as $\bar{\rho}|A|^2 = 1$ and saturation is attained around $L_{\text{sat}}/L_g \approx 10$, similar to the 1D model. Since diffraction is present in Fig 5.4, we lose radiation from the interaction region such that the maximum intensity cannot be attained. The normalization will be further discussed in Chapter 7.

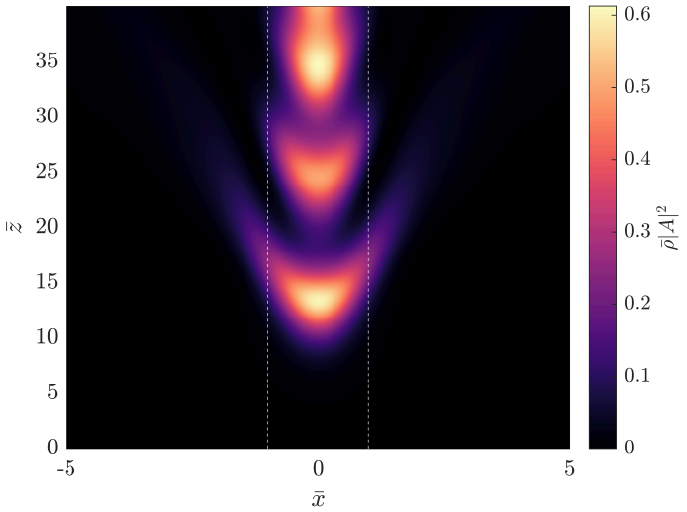

Figure 5.4: Normalized radiation intensity at $\bar{y} = 0$ against $\bar{z}$ and $\bar{x}$ for $\bar{\rho} = 0.2$, $a = 10^{-2}$, $\sigma = \beta = 0$. Dotted lines at $\bar{x} = \pm 1$ signify e-beam waist.

Next, we consider transverse cross-sections of the normalized intensity in the $(\bar{x}, \bar{y})$-plane at two longitudinal positions from Fig. 5.4 for $\bar{\rho} = 0.2$, $a = 10^{-2}$ and $\sigma = \beta = 0$. The first $\bar{z}$-position in Fig. 5.5(a) is taken right after saturation, where the center beam corresponds to the radiation that largely overlaps with the electron beam and the outer ring corresponds to radiation that has escaped the beam at saturation due to diffraction. Again, the white dotted lines indicate

the regions of the electron beam waist $\bar{x} = \bar{y} = \pm 1$. We see a significant difference in intensity between the circle that falls within the interaction volume and outside. Logically, radiation that falls within the beam waist boundaries can be subjected to the QFEL amplification process whilst the outer radiation ring is spatially separated from the electron beam such that amplification can no longer occur. The second $\bar{z}$-position in Fig. 5.6(a) is taken well after saturation and the outer ring has almost fully disappeared. Due to lack of amplification, the intensity drops significantly such that a Gaussian profile within the interaction volume becomes dominant.

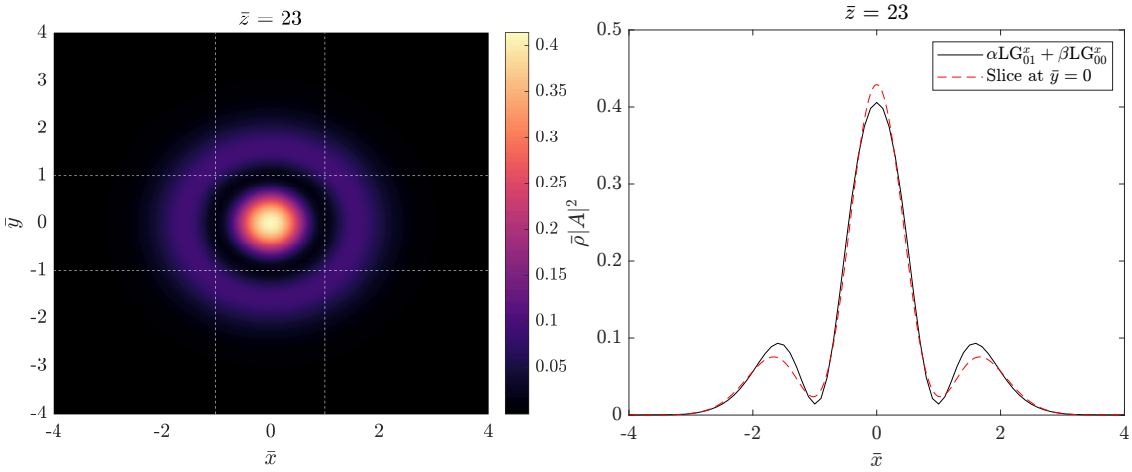

(a) (b)

Figure 5.5: Transverse intensity cross-section (a) and slice intensity with LG00 fit (b) for $\bar{\rho} = 0.2$, $\delta = 5$, $a = 10^{-2}$ at $\bar{z} = 23$

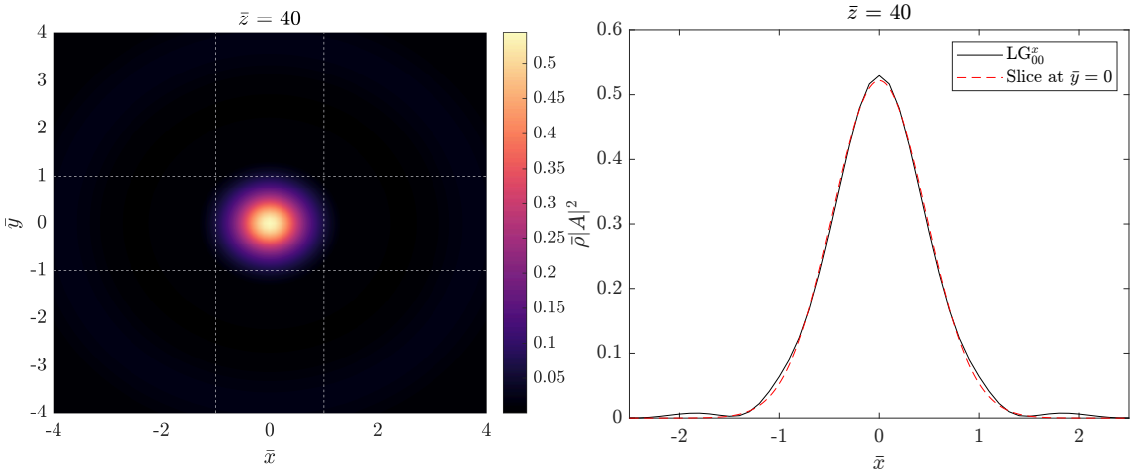

(a) (b)

Figure 5.6: Transverse intensity cross-section (a) and slice intensity with LG00+LG01 fit (b) for $\bar{\rho} = 0.2$, $\delta = 5$, $a = 10^{-2}$ at $\bar{z} = 40$

We fit (slices of) the two transverse profiles explicitly with a combination of Laguerre-Gauss (LG) mode fits in Figs. 5.5(b) and 5.6(b), where an LG mode for radial p and azimuthal index l

is given by

$$\mathrm{LG}pl(\bar{z},r,\varphi)=\sqrt{\frac{2p!}{\pi(p+|l|)!}}\frac{w_0}{w}\left(\frac{r\sqrt{2}}{w}\right)^{|l|}e^{-\frac{r^2}{w^2}}L_p^{|l|}\left\{\frac{2r^2}{w^2}\right\}e^{-ik\frac{r^2}{2R}-i\psi}e^{-il\varphi} \tag{5.3}$$

Using only two modes, LG00 and LG01, we find that the fit already agrees with the transverse radiation pattern, respectively with an R-square of 0.9947 in Fig. 5.5(b) and 0.9953 in Fig. 5.6(b). From this, we may conclude that the solution can be well approximated by already a small number of LG modes, taking into account that more modes would further improve the goodness of the fit. Especially well after saturation, we observe dominant amplification of a single Gaussian (LG00) mode.

5.2 Decomposition in transverse radiation modes

The 3D description of the radiation field has allowed for the radiation to diffract away from the interaction volume, which can be represented by a small number of transverse LG modes. We also observed amplification of the fundamental mode. For more efficient simulation, we propose to adopt an approach based on the decomposition in transverse radiation modes [58, 59, 60], and introduce it for the first time to a QFEL model. This is done to the following form of the field equation:

$$\frac{\partial A}{\partial\bar{z}}+\frac{\partial A}{\partial z_1}-ia\nabla^2_{\mathbf{x}_\perp}A=b(\mathbf{x}_\perp,\bar{z},z_1)+i\delta A, \tag{5.4}$$

where the bunching factor in the Wigner model is given by $b(\mathbf{x}_\perp,\bar{z},z_1)=\sum_{m=-\infty}^{\infty}w^1_{m+\frac{1}{2}}(\mathbf{x}_\perp,\bar{z},z_1)$. The first step is to resolve for the z_1-coordinate via a Fourier decomposition in s spatial frequencies in z_1 for A and b according to

$$A(\mathbf{x}_\perp,\bar{z},z_1)=\sum_s A_s(\mathbf{x}_\perp,\bar{z})e^{ik_sz_1};\qquad b(\mathbf{x}_\perp,\bar{z},z_1)=\sum_s b_s(\mathbf{x}_\perp\bar{z})e^{ik_sz_1}. \tag{5.5}$$

For the next step, we assume the decomposition of the radiation amplitude $A_s(\mathbf{x}_\perp,\bar{z})$ on an arbitrary, orthogonal mode basis Θ^{pl} normalized as

$$\iint\left|\Theta^{pl}_s\right|^2\mathrm{d}\mathbf{x}_\perp=\int_0^{2\pi}\int_0^{\infty}\Theta^{pl}_s\Theta^{pl*}_s r\mathrm{d}r\mathrm{d}\varphi=1. \tag{5.6}$$

Switching to a cylindrical coordinate system $A_s(\bar{z},\mathbf{x}_\perp)=A(\bar{z},r,\varphi)$, we can write the total field as a finite sum over these transverse modes:

$$A_s(\bar{z},r,\varphi)=\sum_{p=0}^{\infty}\sum_{l=-\infty}^{\infty}a^{pl}_s(\bar{z})\Theta^{pl}_s(\bar{z},r,\varphi). \tag{5.7}$$

We adopt Laguerre-Gaussian (LG) modes typical for transverse cylindrical symmetry. Again, each transverse mode is labelled by a radial index p and azimuthal index l:

$$\Theta^{pl}_s(\bar{z},r,\varphi)=\sqrt{\frac{2p!}{\pi(p+|l|)!}}\frac{w_{0,s}}{w_s}\left(\frac{r\sqrt{2}}{w_s}\right)^{|l|}e^{-\frac{r^2}{w_s^2}}L_p^{|l|}\left\{\frac{2r^2}{w_s^2}\right\}e^{-ik_s\frac{r^2}{2R_s}-i\psi_s}e^{-il\varphi} \tag{5.8}$$

In this expression $w_s=w_s(\bar{z})$, $R_s=R_s(\bar{z})$ and $\psi_s=\psi_s(\bar{z})$ respectively indicate the waist size, phase front curvature and Gouy phase for each spatial frequency mode k_s. Combining both the longitudinal and transverse spatial expansion yields

$$A(\bar{z},z_1,\mathbf{x}_\perp)=\sum_{s=-\infty}^{\infty}\sum_{p=0}^{\infty}\sum_{l=-\infty}^{\infty}a^{pl}_s(\bar{z})\Theta^{pl}_s(\bar{z},r,\varphi)e^{ik_sz_1}. \tag{5.9}$$

By substitution of Eq. (5.9) in Eq. (5.4), one could write the second-order PDE into a collection of first-order ODE's of the form

$$\frac{\partial a_s^{pl}}{\partial \bar{z}}\Theta_s^{pl} + a_s^{pl}\frac{\partial \Theta_s^{pl}}{\partial \bar{z}} + ik_s a_s^{pl}\Theta_s^{pl} - ia\left(\frac{1}{r}\frac{\partial}{\partial r}\Big(r\frac{\partial \Theta_s^{pl}}{\partial r}\Big) + \frac{1}{r^2}\frac{\partial^2 \Theta_s^{pl}}{\partial \varphi^2}\right)a_s^{pl} = \Big(b_s^{pl} + i\delta a_s^{pl}\Big)\Theta_s^{pl} \quad (5.10)$$

It is clear that the first term in this expression contains $\partial a_s^{pl}/\partial \bar{z}$ which is the evolution we set out to capture in an ODE. By multiplying both sides of Eq. (5.10) by Θ_s^{pl*} and consequently integrating over both transverse coordinates r and φ, the normalization condition ensures that

$$\frac{\partial a_s^{pl}}{\partial \bar{z}} + a_s^{pl}\iint \frac{\partial \Theta_s^{pl}}{\partial \bar{z}}\Theta_s^{pl*} r\mathrm{d}r\mathrm{d}\varphi + ik_s a_s^{pl} - ia\cdot a_s^{pl}\iint\left(\frac{\partial}{\partial r}\Big(r\frac{\partial \Theta_s^{pl}}{\partial r}\Big) + \frac{1}{r}\frac{\partial^2 \Theta_s^{pl}}{\partial \varphi^2}\right)\Theta_s^{pl*}\mathrm{d}r\mathrm{d}\varphi = b_s^{pl} + i\delta a_s^{pl} \quad (5.11)$$

This is rewritten to the following evolution equation for a_s^{pl}

$$\frac{\partial a_s^{pl}}{\partial \bar{z}} = b_s^{pl} - a_s^{pl}\left(\iint\left[r\frac{\partial \Theta_s^{pl}}{\partial \bar{z}} + ia\left(\frac{\partial}{\partial r}\Big(r\frac{\partial \Theta_s^{pl}}{\partial r}\Big) + \frac{1}{r}\frac{\partial^2 \Theta_s^{pl}}{\partial \varphi^2}\right)\right]\Theta_s^{pl*}\mathrm{d}r\mathrm{d}\varphi + ik_s - i\delta\right). \quad (5.12)$$

From here, we make use of the fact that the transverse nabla-operator works solely on the predefined expressions of LG modes. This is numerically more efficient, especially when the number of modes can be kept sufficiently small which the results in subsection 5.1.2 strongly suggest. The mode amplitudes can then be easily solved for and are subsequently recombined to construct the complete 4D field.

5.3 The structure of a 3D QFEL model

As of yet, the model still omits the transverse electron dynamics and the transverse (laser) undulator profile. To wrap up this chapter, we will review the theoretical steps on how to fit these into the Wigner model. For classical FEL models, this is done by a straightforward account of the transverse phase space $(\mathbf{x}_\perp, \frac{\mathrm{d}\mathbf{x}_\perp}{\mathrm{d}\bar{z}})$ and the complete 3D ponderomotive wave from Eq. (2.4) in the Hamiltonian from Eq. (2.5). However, the 3D extension in a QFEL model is more intricate because of the different nature of the electron-light interaction along the transverse and longitudinal axes [32]. The quantum mechanical nature of the interaction is important for the longitudinal dynamics whilst the transverse dynamics adhere to a classical description for thermal electron beams. As a consequence, this 3D model should not only admit the 1D limit when we drop transverse dependencies and the classical 3D Vlasov limit for $\bar{\rho} \gg 1$, but in addition a separate classical limit only for the transverse dynamics.

5.3.1 Extending the Wigner model

The Wigner formalism is again well-suited to capture such a system, and a similar procedure as before can followed: (i) formulate a Hamiltonian $\mathcal{H}$ with quantum operators, (ii) use $\mathcal{H}$ to derive evolution of either the quantum wave function Ψ using the Schrödinger equation or the density operator $\hat{\varrho}$ using Louiville-von Neumann equation, and (iii) determine the evolution of the discrete Wigner function w_s by substitution of the evolution equation for Ψ or $\hat{\varrho}$. The 3D Hamiltonian operator in universal scaling is given by [28]

$$\mathcal{H}^{3\mathrm{D}}(\bar{z}) = \frac{\hat{p}^2}{2\bar{\rho}^{3/2}} + \frac{\alpha b}{2}\hat{p}_\perp^2 + \Big[\frac{\xi}{2\rho\sqrt{\bar{\rho}}}(1-|g|^2) - \frac{bX}{4}\alpha^2\hat{p}_\perp^2\Big]\hat{p} - \Big[g^* A e^{i\hat{\vartheta}} - \mathrm{H.c.}\Big] + \frac{\xi}{\alpha\rho\sqrt{\rho}X}|g|^2, \quad (5.13)$$

where the transverse momentum operator $\hat{\mathbf{p}}_\perp = -i\nabla_{\bar{\mathbf{x}}_\perp}$ is associated with the variable $\mathbf{p}_\perp = (\gamma_r\sigma_x/\lambda_c)\mathbf{x}'_\perp$ where $\mathbf{x}'_\perp = \frac{\mathrm{d}\mathbf{x}_\perp}{\mathrm{d}\bar{z}}$ and $\lambda = \hbar/mc$ the Compton wavelength. This operator forms a canonically conjugate pair with the transverse position operator $\hat{\bar{\mathbf{x}}}_\perp = \hat{\mathbf{x}}_\perp/\sigma_x$. Furthermore, $\alpha =$

$\lambda\!\!\!^{-}_c/\epsilon_n$ where ϵ_n is the normalized transverse beam emittance, $X = 4\pi\epsilon_n/(\gamma_r\lambda_R)$, $\xi = a_0^2/(1+a_0^2)$ and $b = L_g/\beta^* = L_g(\epsilon_n/\sigma_x^2\gamma_r)$. The transverse (laser) undulator profile is given by $g = g(\bar{\mathbf{x}}_\perp, \bar{z})$, where for example a Gaussian TEM_{00} looks like

$$g(\bar{\mathbf{x}}_\perp, \bar{z}) = \frac{1}{1 - i(L_g/Z_L)(\bar{z} - \bar{z}_0)} e^{-\frac{|\bar{\mathbf{x}}_\perp|^2}{4\sigma_L^2(1 - i(L_g/Z_L)(\bar{z} - \bar{z}_0))}}, \tag{5.14}$$

where $\sigma_L = R/\sigma_x$ with R the rms laser radius at the waist position and $Z_L = 4\pi R^2/\lambda_L$ the laser Rayleigh length. In the 1D limit, we can simply write $g(\bar{\mathbf{x}}_\perp, \bar{z}) = g = 1$. For step (ii), we consider the evolution of $\hat{\varrho}$ using the Louiville-von Neumann equation

$$\frac{\mathrm{d}\hat{\varrho}}{\mathrm{d}\bar{z}} = i[\mathcal{H}, \hat{\varrho}], \tag{5.15}$$

where we can plug in Eq. (5.13) for the Hamiltonian. For step (iii) we first define a 3D discrete Wigner distribution function as

$$w_s(\vartheta, \bar{\mathbf{x}}_\perp, \bar{z}, z_1) = \frac{1}{2\pi^3} \int_{-\pi}^{\pi} \int_{-\infty}^{\infty} \langle \vartheta + \vartheta', \bar{\mathbf{x}}_\perp + \bar{\mathbf{x}}'_\perp | \, \hat{\varrho} \, | \bar{\mathbf{x}}_\perp - \bar{\mathbf{x}}'_\perp, \vartheta - \vartheta' \rangle \, e^{-2i(s\vartheta' + \bar{\mathbf{x}}'_\perp \cdot \mathbf{p}_\perp)} \mathrm{d}^2\bar{\mathbf{x}}'_\perp \mathrm{d}\vartheta', \tag{5.16}$$

which we subsequently differentiate with respect to $\bar{z}$, and where we substitute Eq. (5.15) in the resulting expression. This rather long algebraic manipulation yields the exact evolution of the Wigner function w_s [28], though we can still make one additional simplification. Up to now, we describe an electron beam with arbitrary normalized transverse emittance all the way down to the quantum limit ($\epsilon_n \sim \lambda\!\!\!^{-}_c$) whilst we already recognized that a classical limit would suffice here. To this end, we assume a thermal momentum distribution with a width $\Delta\mathbf{x}'_\perp$ much larger than the quantum limit, *i.e.* $\Delta\mathbf{x}'_\perp \sim (\epsilon_n/\sigma_x\gamma_r) \gg (\lambda\!\!\!^{-}_c/\sigma_x\gamma_r)$. To allow for an explicit transverse classical limit, we already introduced $\alpha = \lambda\!\!\!^{-}/\epsilon_n$ such that $\bar{\mathbf{p}}_\perp = (\sigma_x\gamma_r/\epsilon)\mathbf{x}'_\perp = \alpha\mathbf{p}_\perp$, and perform a Taylor series expansion by taking notice of the fact that $\alpha \ll 1$ such that only the 0-th order terms in α remain. This yields the following evolution equation for the Wigner function $w_s(\vartheta, \bar{\mathbf{x}}_\perp, \bar{\mathbf{p}}_\perp, \bar{z}, z_1)$:

$$\frac{\partial w_s}{\partial \bar{z}} + \underbrace{b(\bar{\mathbf{p}}_\perp \cdot \nabla_{\bar{\mathbf{x}}_\perp}) w_s}_{\text{term 1}} + \left[\frac{s}{\bar{\rho}^{3/2}} + \underbrace{\frac{\xi}{2\rho\sqrt{\rho}}(1 - |g|^2) - \frac{b^2}{4a}\bar{p}_\perp^2}_{\text{term 2}} \right] \frac{\partial w_s}{\partial \vartheta} - (g^* A e^{i\vartheta} + g A^* e^{-i\vartheta})$$
$$\times [w_{s+\frac{1}{2}} - w_{s-\frac{1}{2}}] \underbrace{- \frac{\xi}{\rho\sqrt{\bar{\rho}}} \nabla_{\bar{\mathbf{x}}_\perp} |g|^2 \cdot \nabla_{\bar{\mathbf{p}}_\perp} w_s}_{\text{term 3}} = 0. \tag{5.17}$$

Let us briefly discuss the three additional transverse terms that have appeared compared to Eq. (3.37). Term 1, in unscaled form $\mathbf{x}'_\perp \cdot \nabla_{\mathbf{x}_\perp}$ describes the diverging electron beam which leads to an increase of the beam waist $\sigma(\bar{z})$. Both contributions of term 2 signify a change in FEL resonance caused by respectively the transverse undulator profile and the beam emittance. Given that the resonant wavelength reads

$$\lambda_R = \frac{\lambda_L}{4\gamma^2}(1 + a_0^2 + \gamma^2\theta^2), \tag{5.18}$$

we see that a transverse undulator profile $a_0 = a_0(\mathbf{x}_\perp) \neq$ const. and beam divergence $0 \leq \theta \leq (\epsilon_n/\gamma\sigma)$ alter the resonant wavelength λ_R. Finally, term 3 stands for an additional ponderomotive force term because of the transverse distribution of the undulator field. Next, it can be shown that Eq. (5.17) is coupled to the 3D radiation field $A(\bar{x}_\perp, \bar{z}, z_1)$ as follows:

$$\frac{\partial A}{\partial \bar{z}} + \frac{\partial A}{\partial z_1} - ia\nabla_{\bar{\mathbf{x}}_\perp^2} A = g \sum_m \int_{-\pi}^{\pi} \int_{-\infty}^{\infty} w_{m+\frac{1}{2}} e^{-i\vartheta} \mathrm{d}^2\bar{\mathbf{p}}_\perp \mathrm{d}\vartheta + i\delta A. \tag{5.19}$$

Here we use the fact that the current density J_0 from the 3D Maxwell equation can be written in terms of the (integer) Wigner functions w_m [32]. This describes the radiation field driven by the three-dimensional bunching factor.

5.3.2 Limitations

The model in Eqs. (5.17) and (5.19) captures both the complete time-dependent electron motion and laser and radiation profiles using a 7D Wigner function. However, evaluating this 7D array requires a combination of integration schemes, interpolation methods, decomposition techniques and division of computational load which, in the end, becomes highly restrictive for the model's numerical efficiency [29]. In addition, it is still not exhaustive for all QFEL dynamics since spontaneous emission and space-charge effects are excluded from the model. Hence, there is a need for a simpler model that includes these effects as well as captures aspects of the 3D dynamics in a numerically efficient way. This is the model as presented in Eqs. (5.1) and (5.2) where we include 3D radiation dynamics. To justify its use, we do rely on three important simulation results of the 3D Wigner model (Eqs. (5.17)-(5.19)). First off, it was shown that a transverse beam emittance does not prevent for the collective QFEL instability to occur as long as it adheres to a certain upper limit dependent on specific experimental parameters such as λ_R and σ_x [32]. Secondly, by analyzing the energy stability of several SASE runs it was found that steady-state solutions serve as a reliable indicator for the average SASE output given a sufficiently long bunch $L_b > 20L_c$ [29]. Thirdly, the presence of a Gaussian undulator profile has only slightly diminishing effects ($\sim 10\%$) on the efficiency when $Z_L > 5L_g$ and $2\sigma_x < R < 5\sigma_x$ [29]. Lastly, an important feature of our model is the fact that the 3D field is still driven by 1D electron dynamics such that the 1D description of space-charge and spontaneous emission still holds. All in all, for the first time we presented a comprehensive QFEL model that takes into account both decoherence effects and 3D diffraction.

6 Experimental realization

In this final chapter, the theoretical and numerical work which led to our novel model presented in Chapter 5 is used to investigate a realizable QFEL set-up. We start by reviewing the most important theoretical constraints a future experiment should adhere to. Subsequently, we specify the requirements for the electron injector and consider the ultracold electron source (UCES) in particular, which could meet the stringent requirements for potential QFEL operation. We additionally consider the required laser undulator properties which include geometrical matching between the laser and electron bunch. To finish, we present a set of design parameters for a QFEL based on simulation results of the model presented in Chapter 5.

6.1 Basic criteria and theoretical constraints

In this section, we will review the most important theoretical constraints for QFEL operation. The experimental challenge is twofold: the electron bunch and laser beam parameters should allow for both efficient operation of the quantum regime as well as proper geometric overlap to attain the required interaction volume. Starting with the first, the initial electron energy spread $\Delta\gamma$ should be sufficiently small compared to the single-photon recoil to avoid discreteness washing out:

$$\frac{\Delta\gamma}{\gamma} < \frac{\hbar k_R}{\gamma mc} = \frac{\rho}{\bar{\rho}}. \tag{6.1}$$

On top of that, for QFEL interaction to yield exponential growth, the initial energy spread should be contained within the gain bandwidth that follows from the linear analysis (Fig. 3.2)

$$\frac{\Delta\gamma}{\gamma} < \rho\sqrt{\bar{\rho}}. \tag{6.2}$$

These expressions form the explicit constraints respectively for the *emergence* and the *efficient exploitation* of the quantum regime. In a deep quantum regime $\bar{\rho} < 1$, the condition in Eq. (6.2) becomes more restrictive than Eq. (6.1) such that imposing the latter automatically satisfies the first. Assuming this regime, we can rewrite the energy spread condition to an upper bound on the radiated bandwidth as follows

$$\frac{\Delta\lambda_R}{\lambda_R} = 2\frac{\Delta\gamma}{\gamma} < 2\rho\sqrt{\rho}. \tag{6.3}$$

We can subsequently pose that, in order to contribute to the two-level QFEL dynamics, the radiation produced by each electron must adhere to Eq. (6.3). The radiated wavelength for each electron is determined by the following resonance relation

$$\lambda_R = \frac{\lambda_L}{4\gamma^2}(1 + a_0^2 + \gamma^2\theta^2), \tag{6.4}$$

for a given angle θ with respect to the propagation axis. This equation immediately allows seeing what could push λ_R outside the allowed bandwidth, given that realistic electron bunches and lasers inevitably come with variations in their characteristic quantities. First off, both the electron

energy spread $\Delta\gamma$ and the angular spread $\delta\theta$ cause an increase in the radiation bandwidth according to Eq. (6.4). Also, a non-uniform laser undulator parameter $a_0 = a_0(\mathbf{x}, \bar{z})$ induces variations around the resonant wavelength. In the next sections, we will formulate conditions for allowed variations of these specific quantities.

6.2 Electron injector

For QFEL operation, relativistic electron bunches collide with a laser pulse to produce coherent X-ray pulses. Here, we consider the experimental demands put on the bunch quality for QFELs. In general, the bunch quality is expressed as a combination of bunch charge Q and the transverse and longitudinal normalized rms emittance. The transverse normalized emittance $\epsilon_\perp$ is used together with the rms electron beam radius σ_x as a measure for the beam divergence, given by $\delta\theta = (\epsilon_g/\sigma_x)$ with $\epsilon_g = \epsilon_\perp/(\gamma\beta)$ the geometrical transverse emittance. We can use Eq. (6.4) to derive that the maximum allowed divergence angle, and thus the upper-bound on the transverse emittance for efficient operation of the QFEL regime is

$$\gamma^2(\delta\theta)^2 \leq 2\rho\sqrt{\bar{\rho}} \qquad \rightarrow \qquad \epsilon_\perp \leq \sigma_x\sqrt{\rho\sqrt{\bar{\rho}}(1+a_0^2)}. \tag{6.5}$$

Next, we consider the geometrical matching conditions. Namely, beam divergence reduces the electron density effectively deteriorating the strength of the electron-light interaction. In addition, the overlap region is reduced, which leads to an additional condition for the bunch emittance. We therefore require that the interaction length $L_{\text{int}} = NL_g$ should fit twice within $\beta^* = \gamma\sigma_x^2/\epsilon_\perp$, which is the betatron-function at the center of the interaction [61]. This leads to

$$\epsilon_\perp \leq \frac{\sigma_x^2\gamma}{L_{\text{int}}} \tag{6.6}$$

where we additionally impose that the interaction length should be at least twice the laser Rayleigh length, *i.e.* $L_{\text{int}} = c\tau_L \approx 2Z_L = 4\pi R^2/\lambda_L$ where R is the rms laser radius at focus. This ensures that the electron bunch is fully contained within the laser pulse throughout the interaction. To continue, the longitudinal normalized emittance $\epsilon_\parallel$ relates the rms bunch duration σ_t and the rms longitudinal energy spread σ_γ. This Lorentz-invariant quantity is defined for a bunch without chirp as

$$\epsilon_\parallel = \sigma_t\sigma_\gamma \tag{6.7}$$

We have already seen that the energy spread σ_γ has a strict upper limit given by Eq. (6.2). For typical QFEL operation, short bunch lengths (on the order of 100 fs) are desirable to obtain appreciable electron densities and ultra-short X-ray pulses. Together with the bunch waist σ_x and the bunch charge Q, the bunch length σ_t determines the mean electron density on which ρ explicitly depends. Thereby, this directly determines how strongly coupled the electron-light interaction will be. For the prospected MeV electron beam energy, we require an exceptional electron injector that is especially capable of preserving low transverse emittances $\epsilon_\perp < 0.1$ mm mrad for decent bunch charges of $Q \sim 1$ pC. To this end, we investigate the ultracold electron source (UCES) [35] as a potential QFEL electron injector.

6.2.1 Ultracold electron source

The ultracold electron source, or UCES, produces highly charged bunches by near-treshold photoionization of laser-cooled gas trapped in a grating magneto-optical trap (GMOT) [62]. Using this approach, electron temperatures as low as a few-10 K can be reached, as was demonstrated by nanosecond [63] and femtosecond ionization [64]. The minimal source size σ_x is limited by the overlap between the excitation and ionization laser for high bunch charges. The transverse

beam quality is subsequently expressed as the normalized rms emittance and can be written, in the waist, as the product of the beam size σ_x and momentum spread $\sigma_{p_x} = \sqrt{\langle p_x^2 \rangle}$:

$$\epsilon_\perp = \sigma_x \sigma_{p_x} = \sigma_x \sqrt{\frac{k_B T}{mc^2}}, \tag{6.8}$$

where k_B is Boltzmann's constant and an effective electron temperature T is attributed to the transverse momentum distribution as $\sigma_{p_x} = \sqrt{m k_B T}$. Strongly reducing the electron source temperature thus allows for values of $\epsilon_\perp$ which can be significantly lower than conventional photoemission sources [65]. For example, for an rms transverse source size $\sigma_x = 25$ μm of temperature $T = 10$ K the normalized emittance is $\epsilon_\perp = 1$ nm rad, which is regularly achieved in the UCES [64, 66]. In addition, the trapped gas cloud size and therefore the longitudinal size of the ionization volume is typically ~ 1 mm, such that electron densities can be as high as $n_e \sim 10^{18}$ m^{-3}. This allows for a combination of high bunch charges and emittances as low as $\epsilon_\perp \sim 1$ nm rad, which meet the strict emittance upper bounds given by Eqs. (6.5)-(6.6). The electron bunches could be focused to a transverse size of several μm and bunch lengths up to ~ 100 fs [35], which is typically required for the characteristic QFEL interaction. All in all, the UCES could be an excellent candidate for driving QFEL interaction as it could meet the stringent requirements for the bunch charges and emittance.

6.2.2 Bimodal TM010 TM020 cavity

Presently, the electrons in the UCES are extracted by an electrostatic field [62], which has two main drawbacks. First, the electrons from the trailing part of the bunch accelerate more in the electrostatic field than the leading part causing the electron bunch to compress downstream of the UCES. In the compression point, the space-charge forces within highly charged bunches result in the growth of emittance and uncorrelated energy spread, which is detrimental for lasing. Second, the longitudinal emittance increases at the source since electrons are accelerated during the finite ionization time.

A way to circumvent both drawbacks, simultaneously, is to use an oscillating extraction field at two harmonic frequencies. In Fig. 6.1(a)-(b), the field amplitude for two harmonics of 3 GHz and 6 Ghz is shown in the accelerator of length $z = 3$ cm and radius $r = 4.4$ cm. The time dependence (together with the finite length of the accelerator and amplitude of the field) allows for tuning of the field gradient over the electron bunch at the beginning and end of the accelerator such that (de)compression can be controlled. In addition, the bimodality ensures that the field is set to zero at ionization, thereby overcoming the longitudinal emittance growth. After ionization, the field ramps up quickly, accelerating the electron bunch away from the source. This is clearly depicted in Fig. 6.1(d) by the total field (black line). Since AC-accelerators are less sensitive to breakdowns than DC-accelerators, much stronger fields can be used, which in turn lead to much higher electron beam energy.

We can subsequently simulate the extraction of a bunch from the UCES using this bimodal cavity where the maximum field strength is 45 MV/m. We find that for a 1 pC bunch of $\sigma_x = 60$ μm, $L_b = 360$ μm, $T = 10$ K with an ionization time $t_{\text{ion}} = 0.5$ ps, the resulting energy spread is $\Delta\gamma/\gamma \sim 10^{-4}$ for $E = 800$ keV and the transverse normalized emittance $\epsilon_\perp = 10$ nm rad. The corresponding (averaged) electron phase space is plotted in Fig. 6.2. These values demonstrate that bunch quality in terms of low emittance and energy spread (for sufficient bunch charge) can be preserved using this type of setup. The bunch parameters could thus fall within the intended parameter space of potential QFEL operation, especially given that optimization of the cavity design could further increase the bunch quality.

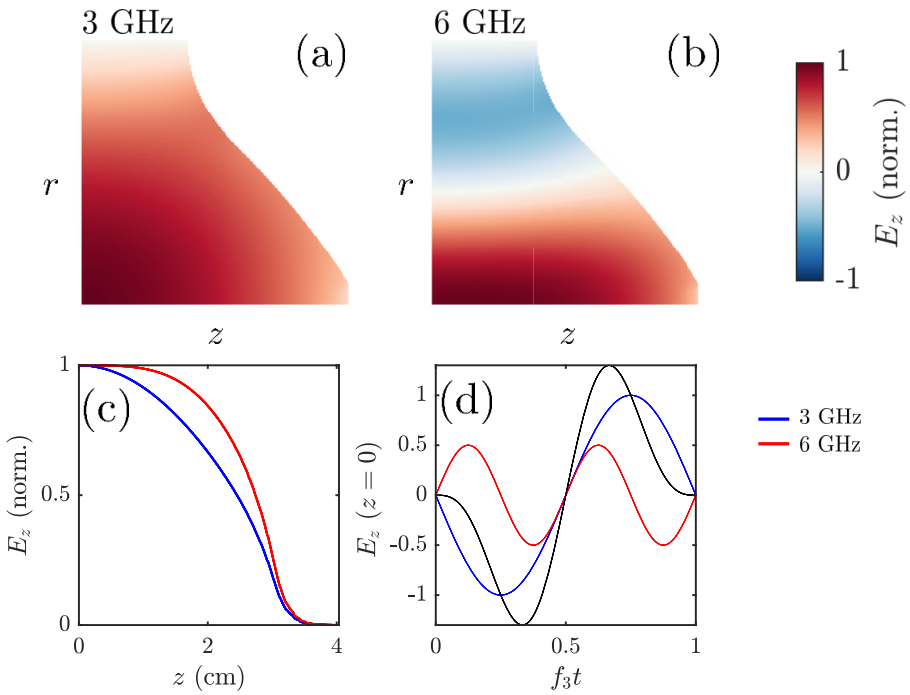

Figure 6.1: Normalized electric field in cross-section of acceleration cavity for (a) 3 GHz and (b) 6 GHz. (c) Field plotted against $\bar{z}$ and (d) against normalized time $f_3 t$ where the black line denotes the sum of the two frequencies.

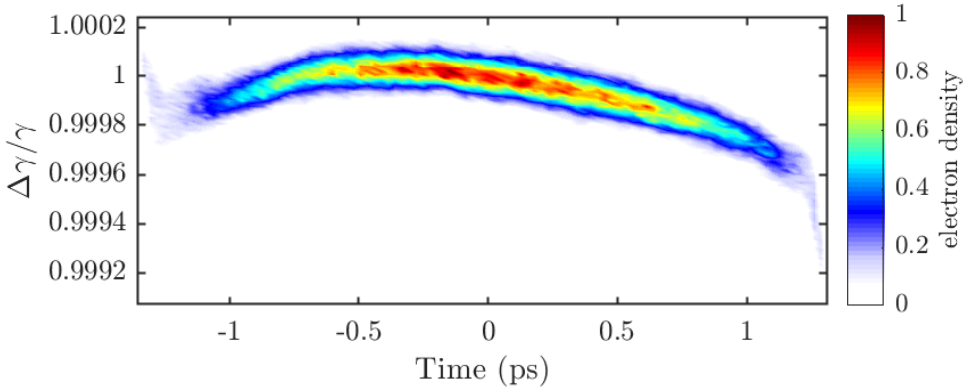

Figure 6.2: Electron phase space for $Q = 1$ pC, 60×360 μm extracted from UCES using bimodal TM010 TM020 cavity, resulting in relative energy spread $\Delta\gamma/\gamma \sim 10^{-4}$ for $E = 800$ keV and emittance $\epsilon_\perp = 10$ nm rad.

6.3 Laser undulator

The principal aim of the laser undulator is to provide a highly uniform field, both in a spatial and temporal sense, in which individual electrons should experience similar field strengths. Realistic laser pulses, however, always come with spatial envelopes thus variations in intensity. First, we revisit the fact that intensity variations of the laser profile, *i.e.* non-constant laser parameter a_0, induce variations in the radiated wavelength by electrons according to Eq. (6.4). Compared to the allowed QFEL bandwidth, we can subsequently pose an upper limit to the allowed relative

variations in a_0

$$\frac{\delta a_0}{a_0} \leq \rho\sqrt{\bar{\rho}}\frac{1+a_0^2}{a_0^2}, \tag{6.9}$$

where we still assume the linear Thomson regime such that $a_0 < 1$. Additionally, the intensity gradients result in an inhomogeneous field which gives rise to a ponderomotive force of the form $\mathbf{F}_{\text{pond}} = -(mc^2/4\gamma)\nabla a_0^2$. This force acts on electrons and causes them to drift out from the center of the bunch inducing an angle of deflection θ. We can approximate an upper bound on the allowed intensity variation by first assuming a constant force over the interaction, such that $\mathbf{F}_{\text{pond}} \sim \nabla a_0^2 \approx \sqrt{2/\pi\sigma_x^2}\delta a_0^2$. In combination with $\theta_{\text{pond}} = (L_{\text{int}}/\sqrt{8\pi}\gamma^2\sigma_x)\delta a_0^2$, a second constraint on the intensity variation can be written as [7]

$$\frac{\delta a_0}{a_0} \leq \frac{2}{a_0}\Big(\frac{\pi\rho\sigma_x^2\gamma^2}{L_{\text{int}}^2}\Big)^{\frac{1}{4}}. \tag{6.10}$$

We have already seen in Eq. (6.6) that $\beta^* \geq 2Z_L$ which ensures that the electron bunch is fully contained within the laser pulse given that $\sigma_x \leq 2R$, and does not diverge considerably within Z_L. Furthermore, for proper geometric matching, the laser pulse length τ_L should be sufficiently long to cover (twice) the duration up till saturation in a head-on scattering geometry, or $\tau_L > 2L_{\text{sat}}/c$. Typically, the radiation intensity saturates around $L_{\text{sat}} \approx 10L_g$ on the mm-to-cm length scale which corresponds to laser pulse lengths τ_L on the ps-to-ns scale. Additionally, the total pulse energy is given by $U = P\tau_L$ for a given laser power P, which for a Gaussian laser profile with a radius R can be written as [31]

$$P\ [\text{TW}] = \frac{a_0 R}{(2\sqrt{2\ln 2})\lambda_L}. \tag{6.11}$$

The combination of long pulse lengths and a low intensity variation is experimentally challenging, but can be obtained in modern high-power laser systems. In addition, we detect a favorable scaling for low values of a_0 in Eq. (6.9) which also lowers the required pulse energy U.

6.4 Proposal design for a QFEL

In this final section, we will present the design parameters of a potential QFEL experiment. Previous feasibility studies [7, 31] have been limited to the Compton regime, which has put significant limitations on the usable laser and electron bunch parameters. Yet, the results from Chapter 4 have now enabled us, for the first time, to make quantitative statements of the effects of space-charge on QFEL dynamics. Most importantly, we have found that the coherent two-state dynamics of QFEL interaction can be preserved in a moderate space-charge regime, only at reduced efficiency. Moreover, we have found that the reduction in $|A|_{\text{sat}}^2$ is way more significant under the influence of a spontaneous emission rate [30] compared to a Raman regime with moderate values of σ (Fig. 4.5). Using this insight, we propose a novel operating regime with non-zero space-charge where we can operate at lower a_0 values. This also automatically mitigates the detrimental effect of spontaneous emission, although our model still takes into account a small non-zero value of β. In addition, low values of a_0 are easier to maintain over the required interaction length, thereby bringing the corresponding parameters within the capabilities of state-of-the-art laser systems. This is particularly interesting given that, up till now, feasibility studies have required laser pulse energies on the order of $10 - 100$ J [29, 31] due to higher operating values of a_0.

6.4.1 Selecting the operating regime

We start by picking typical parameters for the laser undulator operating at $\lambda_L = 1$ μm with a 10 μm beam waist. Based on the UCES, we assume 1 pC 100 fs electron bunches with an rms width $\sigma_x = 1$ μm, such that $\sigma_x < R$. Although this is not yet within the reach of contemporary electron sources, the UCES allows for such bunches to be generated. Thereafter, by selecting values for a_0 and γ we fix almost all remaining parameters. In doing so, we make sure that $\bar{\rho} < 1$,

the effect of space-charge may be moderate ($\sigma \sim 1-5$) and the spontaneous emission rate very small ($\beta/\bar{\rho}^{3/2} \ll 1$). In addition, we aim for a manageable gain length $L_g \sim 1$ mm (and thus interaction length) that can be obtained using pulse lengths within available laser technology. This simultaneously relaxes the upper bound on the required emittance given that the interaction length L_{int} decreases, whilst be comparable in size to the betatron function $\beta^* \sim \epsilon_\perp^{-1}$ (see Eq. (6.6)). Taking all these considerations into account lands us on a laser strength parameter of $a_0 = 0.01$ and an electron energy of $\gamma = 7$ (or $E = 3.35$ MeV), which yield a radiated wavelength $\lambda_R = 5.10$ nm in the Raman QFEL regime for $\bar{\rho} = 0.217$ and $\sigma = 4.12$. For this value of $\bar{\rho}$, the quantum purification is in full effect such that the spectrum consists of a single transform-limited spike. The spontaneous emission parameter is sufficiently small and given by $\beta = 1.8 \cdot 10^{-3} \ll 1$. The maximum allowed gain bandwidth $\rho\sqrt{\rho} \approx 5 \cdot 10^{-5}$ and thus the required (relative) electron energy spread also falls within the prospected capabilities of the UCES. The full set of experimental parameters is listed below in Table 6.1.

6.4.2 Numerical simulations

Given these parameters, we can perform numerical simulations of the QFEL dynamics to quantify the X-ray yield and interaction length. For illustrative purposes, we first run the steady-state 1D Wigner model for the given values of σ and β. Given that the bunch length is picked such that $L_b/L_c \sim 20$, the steady-state model is expected to yield a reasonable approximation of the energy output [29]. In Fig. 6.3(a), we plot the normalized intensity $\bar{\rho}|A|^2$, bunching factor $|b|$ and occupation probabilities $|c_m|^2$ against $\bar{z}$ for $\bar{\rho} = 0.217$, $\sigma = 4.12$ and $\beta = 1.8{\cdot}10^{-3}$, as found through numerical integration of Eqs. (3.40b) and (5.1). We observe that the combination of space-charge and spontaneous emission causes both attenuation and damping of the $c_0 - c_{-1}$ transitions. In Fig. 6.3(b), we explicitly compare the intensity against $\bar{z}$ with and without decoherence, from which we deduce that the radiation saturates about 2 gain lengths later at 40% of the intensity given the proposed Raman regime.

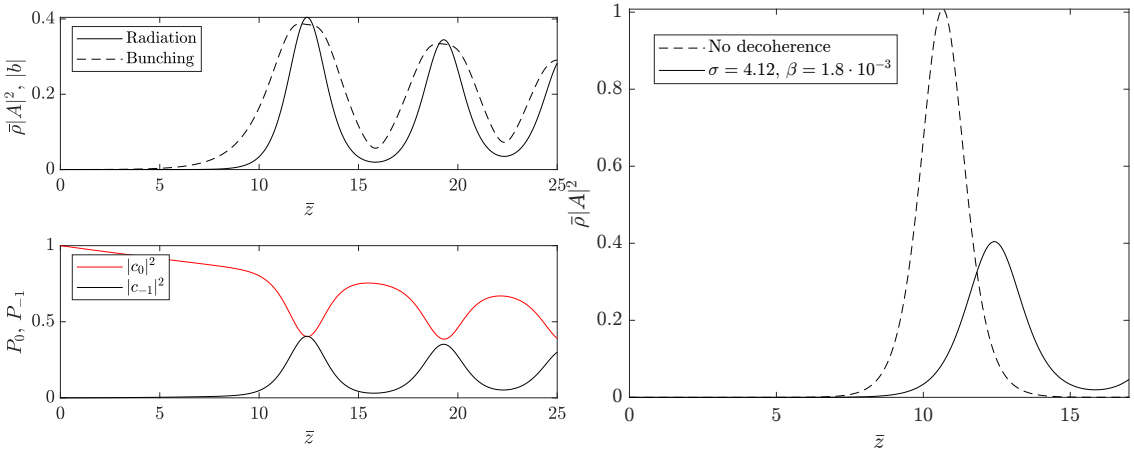

(a) (b)

Figure 6.3: Normalized radiation intensity and bunching against $\bar{z}$ for $\bar{\rho} = 0.2$, $\sigma = 4.12$, $\beta = 1.8 \cdot 10^{-3}$. (a) normalized radiation against $\bar{z}$ with and without decoherence (b).

To obtain a more realistic estimate of the energy output of the QFEL radiation and the saturation length, which simultaneously determines the pulse length τ_L and energy U of the laser, we simulate the 3D model including diffraction from Eqs. (5.1)-(5.2). In Fig. 6.4, the radiation intensity is plotted in the $(\bar{x}, \bar{z})$-plane for $\bar{\rho} = 0.217$, $\sigma = 4.12$, $\beta = 1.8 \cdot 10^{-3}$ and $a = 0.315$,

given a transverse normalized Gaussian occupation distribution. We observe a further increase in saturation length to $L_{\text{sat}} \approx 15L_g$, and a radiation profile where a significant fraction escapes the interaction volume after saturation due to a relatively high value of the diffraction parameter a. Moreover, Rabi-like oscillations quickly damp out after the first saturation peak. To characterize the energy output of the experimental set-up, we briefly discuss the notion of radiated power P_R and the number of emitted photons per pulse N_ϕ. From simulations, we have observed that in the classical regime the saturation intensity is given by $|A|^2_{\text{sat}} \approx 1$ (see Fig. 2.2) and in the quantum regime by $\bar{\rho}|A|^2_{\text{sat}} \approx \eta$ (see Fig. 3.3). Here we define an efficiency term that signifies the decrease in $|A|^2_{\text{sat}}$ under the influence of space-charge and spontaneous emission, thus $\eta = \eta(\sigma, \beta)$. We can approximate the saturation intensity valid in both regimes by

$$|A|^2_{\text{sat}} \approx 1 + \frac{\eta}{\bar{\rho}}. \tag{6.12}$$

The peak radiation power for a given electron beam power $P_{\text{beam}} = \gamma mc^2(I/e)$ can thus be written as [38]

$$P_R = P_{\text{beam}}(\rho|A|^2_{\text{sat}}) \approx \frac{I}{e}\hbar\omega(\eta + \bar{\rho}), \tag{6.13}$$

where we substituted the definition of $\bar{\rho} = \gamma mc\rho/(\hbar k)$. As a result, we can express the number of emitted photons per pulse as

$$N_\phi = \frac{Q}{e}(\eta + \bar{\rho}). \tag{6.14}$$

The detrimental effect of space-charge, spontaneous emission and diffraction on the on-axis ($\mathbf{x}_\perp$=0) saturation intensity is specified by $\eta \approx 0.2$. This is consequently used to determine the number of X-ray photon generated per pulse using Eq. (6.14), which shows an X-ray yield of around $2.6 \cdot 10^6$ photons per pulse. For pulsed lasers with a modest repetition rate around 40 Hz, the prospected soft X-ray flux of 10^8 photons per second could be sufficient for many applications. The full set of experimental parameters is summarized in Table 6.1.

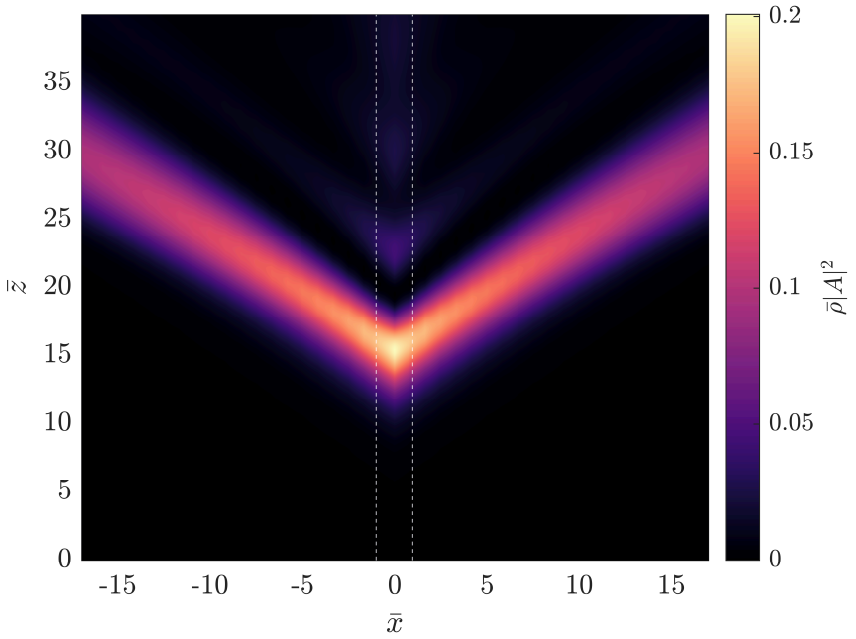

Figure 6.4: Normalized radiation intensity at $\bar{y} = 0$ against $\bar{z}$ and $\bar{x}$ for $\bar{\rho} = 0.2$, $a = 0.315$, $\sigma = 4.12$ and $\beta = 1.8 \cdot 10^{-3}$.

QFEL		
QFEL parameter	$\bar{\rho}$	0.217
FEL parameter	ρ	$1.03 \cdot 10^{-4}$
Max. gain bandwidth	$\rho\sqrt{\bar{\rho}}$	$4.80 \cdot 10^{-5}$
Gain length	L_g (mm)	0.776
Saturation length	L_{sat}/L_g	15
Laser undulator		
Laser wavelength	λ_L (μm)	1
Laser undulator parameter	a_0	0.01
Pulse length	τ_L (ps)	77.6
Pulse energy	U (mJ)	619
Power	P (GW)	7.97
Electron bunch		
Electron energy	E (MeV)	3.58
Transverse normalized emittance	$\epsilon_\perp$ (nm rad)	5.57
Rms bunch radius	σ_x (μm)	1
Peak current	I (A)	10
Electron density	n_e (m^{-3})	$6.63 \cdot 10^{22}$
Bunch charge	Q (pC)	1
Bunch length	L_b (μm)	30.0
Decoherence and 3D effects		
Space-charge parameter	σ	4.12
Spontaneous emission rate	β	0.0018
Diffraction parameter	a	0.315
X-rays		
Radiation wavelength	λ_R (nm)	5.10
Efficiency of sat. intensity	η	0.2
No. of photons per pulse	N_ϕ	$2.60 \cdot 10^6$

Table 6.1: Design parameters for a potential Raman QFEL.

7 | Discussion and outlook

The work in this thesis directly motivates topics of further study, both theoretical and experimental. In this section, we discuss the current space-charge implementation and the 3D QFEL Wigner model with diffraction, and provide an outlook for further research.

Firstly, the theoretical model is limited to the space-charge field induced by the electron density modulation at the ponderomotive beat wave frequency. However, we have shown that for sufficiently strong space-charge ($\sigma \geq 3/4\bar{\rho}^2$) higher harmonics should be taken into account as well. Although we remark that, in a deep quantum regime, σ does typically not exceed this critical value, the dynamics with a higher-harmonic space-charge field can be further investigated and compared to the current description. In addition, macroscopic and transverse components of the space-charge field based on the full 3D charge-distribution should eventually be included in the Wigner model for the most accurate description.

For the multi-dimensional simulations, we have remarked that wave function normalization is different in two or three dimensions thus altering the growth rate and peak intensity. The approach followed in literature [67] and also this work was taking the 3D model as reference for explicit comparison to 1D and 2D. This way, the gain from lower-dimensional simulations is matched through a renormalization factor for b given that the evolution of A in Eq. (2.19) is quadratic in Ψ ($b = \int |\Psi|^2 e^{-i\vartheta} \mathrm{d}\vartheta$). Nevertheless, a thorough account of normalization remains ambiguous, especially given that the derivation of the 1D model also contains a transverse averaging step (see Eq. 2.18). We therefore suggest that the manual bunching normalization and subsequent consistency between 1-, 2- and 3D models with diffraction should be studied in more detail.

A logical extension of our work is to also include the beam emittance. In combination with the effects of space-charge, spontaneous emission and diffraction, such a complete model can be used to quantify the regime where the QFEL instability could potentially be inhibited. Numerical simulation of this model, however, requires a large amount of computational resources. To this end, we have proposed a modal decomposition technique similar to Ref. [60] to efficiently compute the 3D field in terms of transverse LG modes. From current 3D simulations, we have shown predominant amplification of specific LG modes such that a solution may be approximated by a small number of modes, which would significantly speed up computation. Furthermore, these simulations can also be used to investigate the transverse coherence properties in comparison to classical FELs, it being a trivial extension of the theory presented in subsection 3.2.4 and Ref. [46].

As a general remark, with the model presented here, a lot can still be learned from more extensive simulation including different combinations of effects, *e.g.* to study the interplay between spontaneous emission and space-charge. Moreover, since previous feasibility studies were limited to the Compton regime, our model can be used to potentially unveil more realizable QFEL regimes than the one from section 6.4. Finally, preliminary simulation results of the UCES and bimodal extraction cavity have demonstrated that the electron bunch quality (1 pC, $\epsilon_\perp \sim 10$ nm rad, $\Delta\gamma/\gamma \sim 10^{-4}$) can be preserved, even with minimal optimization of the cavity design. This offers promising prospects for achieving the relevant parameter space for QFEL operation.

8 Conclusion

This thesis focused on the theoretical continuation and numerical simulation of the QFEL theory. In the first chapters, we presented a review of the classical and quantum FEL theory and identified the importance of accounting for the Raman QFEL regime. Consequently, we have presented results of a QFEL model that, for the first time, can describe this Raman regime. To this end, we have included microscopic space-charge by quantizing the periodic potential derived from Fourier components of the electron beam density. The most important outcomes of this work can be summarized as follows:

- **The space charge potential has been incorporated in a QFEL Wigner model, which is consistent with the classical limit.**
- **In a moderate space charge regime ($\boldsymbol{\sigma \leq 3/4\bar{\rho}^2}$) the gain and efficiency of a QFEL is reduced, while the coherent two-state dynamics is preserved.**
- **A comprehensive model including spontaneous emission, space-charge and 3D diffraction is presented. We also propose a method to improve the efficiency of the 3D model based on transverse mode decomposition.**
- **The ultracold electron source together with commercially available laser systems can potentially drive a realizable QFEL in a moderate space-charge regime.**

All in all, with the work presented in this thesis we have made a contribution to a more complete understanding and the future experimental realization of QFELs.

Bibliography

[1] Andrew H Rawicz. Theodore harold maiman and the invention of laser. In *Photonics, Devices, and Systems IV*, volume 7138, page 713802. International Society for Optics and Photonics, 2008. 1

[2] EA Seddon, JA Clarke, DJ Dunning, C Masciovecchio, CJ Milne, F Parmigiani, D Rugg, JCH Spence, NR Thompson, K Ueda, et al. Short-wavelength free-electron laser sources and science: a review. *Reports on Progress in Physics*, 80(11):115901, 2017. 1

[3] Jeff Hecht. The history of the x-ray laser. *Optics and photonics news*, 19(5):26–33, 2008. 1, 2

[4] Brian Herman Schaap, Thomas de Vos, Peter Smorenburg, and O Jom Luiten. Photon yield of superradiant inverse compton scattering from microbunched electrons. *New Journal of Physics*, 2022. 1

[5] EL Saldin, EA Schneidmiller, and MV Yurkov. Study of a noise degradation of amplification process in a multistage hghg fel. *Optics Communications*, 202(1-3):169–187, 2002. 1

[6] R. Bonifacio, N. Piovella, and G.R.M. Robb. Quantum theory of sase fel. *Nuclear Instruments and Methods in Physics Research Section A: Accelerators, Spectrometers, Detectors and Associated Equipment*, 543(2):645–652, 2005. 1, 5, 14

[7] Alexander Debus, Klaus Steiniger, Peter Kling, C Moritz Carmesin, and Roland Sauerbrey. Realizing quantum free-electron lasers: a critical analysis of experimental challenges and theoretical limits. *Physica Scripta*, 94(7):074001, 2019. 1, 5, 6, 21, 30, 32, 39, 52

[8] A.E. Siegman. *Lasers*. University Science Books, 1986. 1

[9] D. Nilsson, A. Holmberg, H. Sinn, and U. Vogt. Zone plates for hard x-ray fel radiation. *AIP Conference Proceedings*, 1365(1):120–123, 2011. 3

[10] P Sprangle, CM Tang, and CW Roberson. Collective effects in the free electron laser. *Nuclear Instruments and Methods in Physics Research Section A: Accelerators, Spectrometers, Detectors and Associated Equipment*, 239(1):1–18, 1985. 3

[11] Marie-Emmanuelle Couprie. New generation of light sources: Present and future. *Journal of Electron Spectroscopy and Related Phenomena*, 196, 12 2013. 4

[12] Juan C Gallardo, Richard C Fernow, Robert Palmer, and C Pellegrini. Theory of a free-electron laser with a gaussian optical undulator. *IEEE journal of quantum electronics*, 24(8):1557–1566, 1988. 4

[13] J Gea-Banacloche, G Moore, R Schlicher, M Scully, and H Walther. Soft x-ray free-electron laser with a laser undulator. *IEEE journal of quantum electronics*, 23(9):1558–1570, 1987. 4

[14] K Ta Phuoc, Sébastien Corde, Cédric Thaury, Victor Malka, Amar Tafzi, Jean-Philippe Goddet, RC Shah, Stéphane Sebban, and Antoine Rousse. All-optical compton gamma-ray source. *Nature Photonics*, 6(5):308–311, 2012. 4

[15] Yoshitaka Mori, Hajime Kuwabara, Katsuhiro Ishii, Ryohei Hanayama, Toshiyuki Kawashima, and Yoneyoshi Kitagawa. Head-on inverse compton scattering x-rays with energy beyond 10 kev from laser-accelerated quasi-monoenergetic electron bunches. *Applied Physics Express*, 5(5):056401, 2012. 4

[16] Nathan D Powers, I Ghebregziabher, G Golovin, Cheng Liu, Shouyuan Chen, Sudeep Banerjee, Jun Zhang, and Donald P Umstadter. Quasi-monoenergetic and tunable x-rays from a laser-driven compton light source. *Nature Photonics*, 8(1):28–31, 2014. 4

[17] Klaus Steiniger, Daniel Albach, Michael Bussmann, Markus Loeser, Richard Pausch, Fabian Röser, Ulrich Schramm, Mathias Siebold, and Alexander Debus. Building an optical free-electron laser in the traveling-wave thomson-scattering geometry. *Frontiers in Physics*, page 155, 2019. 4

[18] John MJ Madey. Stimulated emission of bremsstrahlung in a periodic magnetic field. *Journal of Applied Physics*, 42(5):1906–1913, 1971. 4

[19] Peter Kling, Enno Giese, Rainer Endrich, Paul Preiss, Roland Sauerbrey, and Wolfgang P Schleich. What defines the quantum regime of the free-electron laser? *New Journal of Physics*, 17(12):123019, 2015. 5, 15

[20] R Bonifacio, L De Salvo, P Pierini, N Piovella, and C Pellegrini. Spectrum, temporal structure, and fluctuations in a high-gain free-electron laser starting from noise. *Physical review letters*, 73(1):70, 1994. 5

[21] R Bonifacio, N Piovella, and GRM Robb. Quantum theory of sase fel. *Nuclear Instruments and Methods in Physics Research Section A: Accelerators, Spectrometers, Detectors and Associated Equipment*, 543(2-3):645–652, 2005. 5

[22] R Bonifacio, N Piovella, GRM Robb, and Angelo Schiavi. Quantum regime of free electron lasers starting from noise. *Physical Review Special Topics-Accelerators and Beams*, 9(9):090701, 2006. 5

[23] S Inouye, AP Chikkatur, DM Stamper-Kurn, J Stenger, DE Pritchard, and W Ketterle. Superradiant rayleigh scattering from a bose-einstein condensate. *Science*, 285(5427):571–574, 1999. 5

[24] Nicola Piovella, Angel Tarramera Gisbert, and Gordon RM Robb. Classical and quantum collective recoil lasing: a tutorial. *Atoms*, 9(3):40, 2021. 5

[25] D Kruse, Ch von Cube, C Zimmermann, and Ph W Courteille. Observation of lasing mediated by collective atomic recoil. *Physical review letters*, 91(18):183601, 2003. 5

[26] S. Slama, S. Bux, G. Krenz, C. Zimmermann, and Ph. W. Courteille. Superradiant rayleigh scattering and collective atomic recoil lasing in a ring cavity. *Phys. Rev. Lett.*, 98:053603, Feb 2007. 5

[27] N Piovella, MM Cola, L Volpe, R Gaiba, A Schiavi, and R Bonifacio. A wigner function model for free electron lasers. *Optics communications*, 274(2):347–353, 2007. 5, 23, 25

[28] N Piovella, MM Cola, L Volpe, Angelo Schiavi, and R Bonifacio. Three-dimensional wigner-function description of the quantum free-electron laser. *Physical review letters*, 100(4):044801, 2008. 5, 45, 46

[29] A Schiavi, R Bonifacio, N Piovella, MM Cola, and L Volpe. Three-dimensional free electron laser numerical simulations for a laser wiggler in the quantum regime. *Nuclear Instruments and Methods in Physics Research Section A: Accelerators, Spectrometers, Detectors and Associated Equipment*, 593(1-2):80–86, 2008. 5, 25, 47, 52, 53

[30] H Fares, N Piovella, and GRM Robb. The detrimental effect of spontaneous emission in quantum free electron lasers: A discrete wigner model. *Physics of Plasmas*, 25(1):013111, 2018. 5, 29, 39, 52

[31] Rodolfo Bonifacio, Hesham Fares, Massimo Ferrario, Brian WJ McNeil, and Gordon RM Robb. Design of sub-angstrom compact free-electron laser source. *Optics Communications*, 382:58–63, 2017. 6, 52

[32] MM Cola, L Volpe, N Piovella, A Schiavi, and R Bonifacio. 3d wigner model for a quantum free electron laser with a laser wiggler. *Nuclear Instruments and Methods in Physics Research Section A: Accelerators, Spectrometers, Detectors and Associated Equipment*, 593(1-2):75–79, 2008. 6, 45, 46, 47

[33] Makina Yabashi and Hitoshi Tanaka. The next ten years of x-ray science. *Nature Photonics*, 11(1):12–14, 2017. 6

[34] James Lloyd-Hughes, Peter M Oppeneer, T Pereira Dos Santos, Andre Schleife, Sheng Meng, Michael A Sentef, Michael Ruggenthaler, Angel Rubio, Ilie Radu, Margaret Murnane, et al. The 2021 ultrafast spectroscopic probes of condensed matter roadmap. *Journal of Physics: Condensed Matter*, 33(35):353001, 2021. 6

[35] B.H. Schaap, T.C.H. De Raadt, D.F.J. Nijhof, J.G.H. Franssen, P.H.A. Mutsears, and O.J. Luiten. Coldlight: From laser-cooled atoms to coherent soft x-rays. 2020. cited By 0. 6, 49, 50

[36] Rodolfo Bonifacio, Cesare Maroli, and Nicola Piovella. Slippage and superradiance in the high-gain fel: Linear theory. *Optics communications*, 68(5):369–374, 1988. 10

[37] R. Bonifacio, F. Casagrande, and G. Casati. Cooperative and chaotic transition of a free electron laser hamiltonian model. *Optics Communications*, 40(3):219–223, 1982. 11

[38] R. Bonifacio, C. Pellegrini, and L.M. Narducci. Collective instabilities and high-gain regime in a free electron laser. *Optics Communications*, 50(6):373–378, 1984. 11, 54

[39] Nicola Piovella and Luca Volpe. A review of high-gain free-electron laser theory. *Atoms*, 9(2):28, 2021. 13

[40] T. J. Orzechowski, B. Anderson, W. M. Fawley, D. Prosnitz, E. T. Scharlemann, S. Yarema, D. Hopkins, A. C. Paul, A. M. Sessler, and J. Wurtele. Microwave radiation from a high-gain free-electron laser amplifier. *Phys. Rev. Lett.*, 54:889–892, Mar 1985. 14

[41] Paul Emma, R Akre, J Arthur, R Bionta, C Bostedt, J Bozek, A Brachmann, P Bucksbaum, Ryan Coffee, F-J Decker, et al. First lasing and operation of an ångstrom-wavelength free-electron laser. *nature photonics*, 4(9):641–647, 2010. 14

[42] EL Saldin, EA Schneidmiller, and MV Yurkov. Statistical and coherence properties of radiation from x-ray free-electron lasers. *New Journal of Physics*, 12(3):035010, 2010. 14

[43] Giuliano Preparata. Quantum field theory of the free-electron laser. *Phys. Rev. A*, 38:233–237, Jul 1988. 16

[44] N Piovella, M Gatelli, and R Bonifacio. Quantum effects in the collective light scattering by coherent atomic recoil in a bose–einstein condensate. *Optics communications*, 194(1-3):167–173, 2001. 20

[45] R Bonifacio, N Piovella, and GRM Robb. The quantum free electron laser: A new source of coherent, short-wavelength radiation. *Fortschritte der Physik*, 57(11-12):1041–1051, 2009. 21

[46] EL Saldin, EA Schneidmiller, and MV Yurkov. Transverse and longitudinal coherence properties of the radiation from x-ray sase fels. *Proceedings FEL 2006, on JACOW*, pages 206–209, 2006. 21, 56

[47] C. Moritz Carmesin, Peter Kling, Enno Giese, Roland Sauerbrey, and Wolfgang P. Schleich. Quantum and classical phase-space dynamics of a free-electron laser. *Phys. Rev. Research*, 2:023027, Apr 2020. 22

[48] Robert O'connell. *Wigner Distribution*, pages 851–854. 07 2009. 23

[49] Eugene P Wigner. On the quantum correction for thermodynamic equilibrium. In *Part I: Physical Chemistry. Part II: Solid State Physics*, pages 110–120. Springer, 1997. 23, 25

[50] João P. Bizarro. Weyl-wigner formalism for rotation-angle and angular-momentum variables in quantum mechanics. *Phys. Rev. A*, 49:3255–3276, May 1994. 24, 25

[51] Daniela Dragoman. The origin of negative values of the wigner distribution function. *Optik*, 111(4):179–183, 2000. 25

[52] Nicola Piovella and R. Bonifacio. Inhomogeneous effects in the quantum free electron laser. *Nuclear Instruments Methods in Physics Research Section A-accelerators Spectrometers Detectors and Associated Equipment - NUCL INSTRUM METH PHYS RES A*, 560:240–244, 05 2006. 27

[53] GRM Robb and Rodolfo Bonifacio. Competition between coherent emission and broadband spontaneous emission in the quantum free electron laser. *Physics of Plasmas*, 20(3):033106, 2013. 29

[54] Peter Kling, Enno Giese, C. Moritz Carmesin, Roland Sauerbrey, and Wolfgang P. Schleich. High-gain quantum free-electron laser: Long-time dynamics and requirements. *Phys. Rev. Research*, 3:033232, Sep 2021. 32

[55] Giuseppe Dattoli, Hesham Fares, and Silvia Licciardi. Space charge and quantum corrections in free electron laser evolution. *Nuclear Instruments and Methods in Physics Research Section A: Accelerators, Spectrometers, Detectors and Associated Equipment*, 976:164176, 2020. 32, 34

[56] G. Marcus, E. Hemsing, and J. Rosenzweig. Gain length fitting formula for free-electron lasers with strong space-charge effects. *Phys. Rev. ST Accel. Beams*, 14:080702, Aug 2011. 34

[57] Ivan Gadjev, Rob Candler, Claudio Emma, Jere Harrison, Ariel Nause, Jiacong Wu, Avraham Gover, and J.B. Rosenzweig. High-gain, short wavelength fel in the raman regime. *Nuclear Instruments and Methods in Physics Research Section A: Accelerators, Spectrometers, Detectors and Associated Equipment*, 09 2016. 35

[58] P. Sprangle, A. Ting, and C. M. Tang. Analysis of radiation focusing and steering in the free-electron laser by use of a source-dependent expansion technique. *Phys. Rev. A*, 36:2773–2781, Sep 1987. 44

[59] Panagiotis Baxevanis, Ronald D. Ruth, and Zhirong Huang. General method for analyzing three-dimensional effects in free-electron laser amplifiers. *Phys. Rev. ST Accel. Beams*, 16:010705, Jan 2013. 44

[60] A Fisher, P Musumeci, and SB Van der Geer. Self-consistent numerical approach to track particles in free electron laser interaction with electromagnetic field modes. *Physical Review Accelerators and Beams*, 23(11):110702, 2020. 44, 56

[61] Klaus Steiniger, Michael Bussmann, Richard Pausch, Tom Cowan, Arie Irman, Axel Jochmann, Roland Sauerbrey, Ulrich Schramm, and Alexander Debus. Optical free-electron lasers with traveling-wave thomson-scattering. *Journal of Physics B: Atomic, Molecular and Optical Physics*, 47(23):234011, 2014. 49

[62] JGH Franssen, TCH de Raadt, MAW van Ninhuijs, and OJ Luiten. Compact ultracold electron source based on a grating magneto-optical trap. *Physical Review Accelerators and Beams*, 22(2):023401, 2019. 49, 50

[63] G Taban, MP Reijnders, B Fleskens, SB Van der Geer, OJ Luiten, and EJD Vredenbregt. Ultracold electron source for single-shot diffraction studies. *EPL (Europhysics Letters)*, 91(4):46004, 2010. 49

[64] WJ Engelen, MA Van Der Heijden, DJ Bakker, EJD Vredenbregt, and OJ Luiten. High-coherence electron bunches produced by femtosecond photoionization. *Nature communications*, 4(1):1–5, 2013. 49, 50

[65] SB van der Geer, EJD Vredenbregt, OJ Luiten, and MJ de Loos. An ultracold electron source as an injector for a compact sase-fel. *Journal of Physics B: Atomic, Molecular and Optical Physics*, 47(23):234009, 2014. 50

[66] JGH Franssen, TLI Frankort, EJD Vredenbregt, and OJ Luiten. Pulse length of ultracold electron bunches extracted from a laser cooled gas. *Structural Dynamics*, 4(4):044010, 2017. 50

[67] A Schiavi, N Piovella, GRM Robb, and R Bonifacio. Qfel: A numerical code for multi-dimensional simulation of free electron lasers in the quantum regime. In *The Physics And Applications Of High Brightness Electron Beams*, pages 564–572. World Scientific, 2007. 56

A | Runge-Kutta scheme

Here we set out the Runge-Kutta scheme for obtaining numerical solutions to the steady-state 1D FEL model from Eqs. (2.25a)-(2.25c). We first collect all $(2N+1)$ variables in a single vector of the form

$$\mathbf{X} = \begin{bmatrix} \vartheta_1 \cdots & \vartheta_N & p_1 \cdots & p_N & A \end{bmatrix} \tag{A.1}$$

The set of equations can now be written in the form of

$$\frac{\mathrm{d}\mathbf{X}}{\mathrm{d}\bar{z}} = f(\bar{z}, \mathbf{X}). \tag{A.2}$$

More specifically, Eqs. (2.25a)-(2.25c) can be re-expressed in terms of (parts of) the vector $\mathbf{X}$ as follows:

$$\frac{\mathrm{d}\mathbf{X}(1:N)}{\mathrm{d}\bar{z}} = \mathbf{X}(N+1:2N) \tag{A.3a}$$

$$\frac{\mathrm{d}\mathbf{X}(N+1:2N)}{\mathrm{d}\bar{z}} = -\Big(\mathbf{X}(2N+1)e^{i\mathbf{X}(1:N)} - \mathbf{X}^*(2N+1)e^{-i\mathbf{X}(1:N)}\Big) \tag{A.3b}$$

$$\frac{\mathrm{d}\mathbf{X}(2N+1)}{\mathrm{d}\bar{z}} = \sum_N e^{-i\mathbf{X}(1:N)} + i\delta\mathbf{X}(2N+1) \tag{A.3c}$$

Equations of the form as in Eq. (A.2) can be solved using the fourth-order Runge-Kutta method (RK4) for an initial condition $\mathbf{X}(\bar{z}) = \mathbf{X}_0$. This is done in a step-wise manner, where

$$\bar{z}_{i+1} = \bar{z}_i + \Delta\bar{z} \tag{A.4}$$

and the

$$\mathbf{X}_{i+1} = \mathbf{X}_i + \frac{\Delta\bar{z}}{6}(k_1 + 2k_2 + 2k_3 + k_4). \tag{A.5}$$

In this expression, the values for k are given by

$$k_1 = f(\mathbf{X}_i) \tag{A.6a}$$

$$k_2 = f\Big(\mathbf{X}_i + k_1\frac{\Delta z}{2}\Big) \tag{A.6b}$$

$$k_3 = f\Big(\mathbf{X}_i + k_2\frac{\Delta z}{2}\Big) \tag{A.6c}$$

$$k_4 = f\Big(\mathbf{X}_i + k_3\Delta z\Big) \tag{A.6d}$$

The iterative process in these equations can be carried out for a given $\Delta\bar{z}$ and yields solutions of $\mathbf{X}$ over any given $\bar{z}$-domain. For the momentum state model (section 3.2) and the Wigner function model (section 3.3), we follow an identical approach where the vector $\mathbf{X}$ contains respectively the momentum states c_m, or the discrete Wigner components w_s^n.